University of Exeter

College of Engineering, Mathematics and Physical Sciences

Thesis for the Degree of Doctor of Philosophy in Physics

Rapid high-resolution mid-IR imaging for molecular spectral histopathological diagnosis of oesophageal cancers

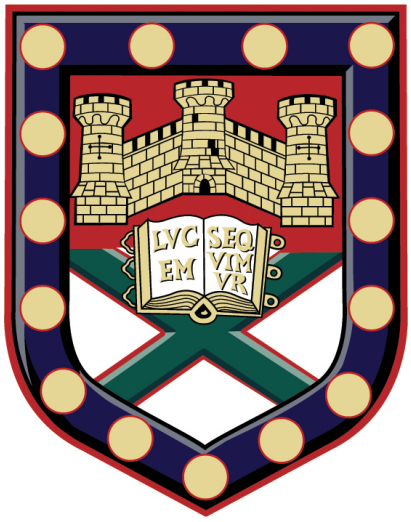

Author:

Michael Hermann

Wolfgang Hermes

Supervisors:

Prof. Dr. Nick Stone

Prof. Dr. Francesca Palombo

I certify that all material in this thesis which is not my own work has been identified and that no material has previously been submitted and approved for the award of a degree by this or any other University.

December 19, 2018 .....

Abstract

This thesis is written as part of Marie-Curie international training network called Mid-TECH. Mid-TECH is devoted to improve mid-infrared (MIR) technologies and consists of 15 PhD projects across European universities. This thesis aims to evaluate new technologies and concepts developed by the project partners for their applicability in a biomedical setting. The clinical problem to diagnose oesophageal cancers serves as an example case for this. The thesis consists of three projects all aimed to further the understanding of MIR hyperspectral imaging.

The first project discussed in chapter 5 demonstrates the use of an new design of the United States Airforce resolution test chart. The new test chart is developed to evaluate spatial resolution of MIR hyperspectral imaging systems. The use of different materials is discussed and the new iteration of the thes chart is evaluated using a state of the art MIR imaging system.

The second project discussed in chapter 6 evaluates the technical differences and their practical implications of discrete frequency MIR imaging systems compared to continuum source systems. A comparison of the two system types is drawn for imaging paraffin embedded sections of oesophageal tissue. Furthermore the effect of chemically removing the paraffin from the sample is compared to a mathematical correction algorithm. The system performance is compared based on their ability to differentiate healthy from cancerous tissue.

The third project discussed in chapter 7 evaluates the potential of a new MIR detection scheme called upconversion in combination with a novel MIR laser source. It is a prove of concept study demonstrating that those two technologies can be deployed to do hyperspectral imaging in the MIR.

Contents

List of Figures

List of Tables

1 Introduction

1.1 Foreword

This thesis is written in 7 independent chapters which the author envisions to be readable independently apart from the summary and discussion chapter.

This work involved a range of external collaborations with other university groups working with imaging systems or setups of varying degrees of maturity, from proof of concept to industrial research grade. Therefore, each chapter is structured like a scientific paper. The chapters 2, 3 and 4 are written in review style providing theoretical backbone of the thesis. Chapter 5, 6 and 7 are original research chapters with independent methods and discussion of the results. The final chapter 8 puts the individual experiments into a wider context.

1.2 Aims of the Thesis

The principal aim of this thesis is to evaluate novel mid-infrared (MIR) systems for their use for histopathological work flows. Research investigating mechanisms for generation and detection of MIR radiation is going through a renaissance to the date this thesis is written. Therefore, it is likely that technological improvements in these areas will progress to applications. MIR hyperspectral imaging as discussed in great detail here is believed to have great potential to improve clinical decision making.

In this thesis, the author gives an overview how new MIR imaging technology could be harnessed to improve workflows in a clinical environment. For this purpose the thesis looks at the diagnosis of oesophageal adenocarcinoma as an example case.

2 Mid-Infrared Technology

Disclaimer: This chapter is an adaptation from a review paper entitled: 'Mid-IR hyperspectral imaging for label-free histopathology and cytology' published by the author of the thesis and collaborators in the IOP journal of optics [1]. The review is published licensed under Creative Commons Attribution 3.0 licence which allows reuse and remix of content. The following chapter is remixed from sections: 2. Mid-infrared light sources; 3. Mid-infrared detection systems and 4. Mid-infrared micro spectroscopy. In addition to the review a section discussing OPOs has been added as they are important for this work.

2.1 Introduction

The last decade has seen the early exploration of myriad applications of vibrational spectroscopy for clinical applications. Both mid-infrared (MIR) absorption spectroscopy and Raman spectroscopy, utilising the inelastic scattering of laser light, probe the specific vibrational energy levels of molecules in the target volume. The two techniques are complementary, probing different vibrational modes based on specific vibrational selection rules. The various methodologies are undergoing translational development for a range of applications from in vivo surface [2] and deep tissue probes [3] providing real-time analysis of disease specific tissue molecular compositional changes; to point of care testing of ex vivo tissues or body fluids [4, 5]; to microspectroscopic analysis and imaging of tissue and cells [6–8]. Until recently the limited speed of vibrational spectroscopic imaging has prevented its translation as a tool in digital spectral histopathology. However, new developments in MIR technologies and a greater understanding of the key discriminating features is leading to a resurgence of interest in MIR spectral histopathology as a tool for rapid molecular identification of disease, particularly to support pathologists in making difficult decisions when assessing early malignant disease [9, 10].

MIR technology is experiencing a renaissance with development of new light sources and detection systems. This is driven by the need for faster imaging systems, as MIR

hyperspectral imaging has proven to be a valuable tool for medical diagnostics but is hampered by relatively slow throughput. Imaging speed has significantly increased within the last five years and is on the brink of becoming competitive to gold standard histopathology procedures. Potentially it could furthermore, offer more detailed chemical information without the need for staining or labelling.

Imaging biological samples using resonant absorption in the MIR region is a particularly challenging task compared to imaging in the visible range of the electromagnetic spectrum. Here we define the MIR region in terms of wavelengths ranging between 2 and 12 µm (5000 to 800 cm^{-1}). A major challenge when measuring the IR absorption spectrum of biological matter is the interference of water absorption, i.e. OH stretching modes giving rise to a broad band centred at 3300 $cm^{-1}$and bending mode at 1620 cm^{-1}. Furthermore, many materials have absorption bands in the MIR range and so there are only a few transparent materials that can be used as substrates, for instance. A problem of equal importance is, that the optical imaging elements made from these materials are less widely available than standard silica or quartz optics.

The scope of this chapter is to give an overview of the state of the art of MIR technologies. The reader is also referred to recent reviews in this area: *Bhargava et al.* [11] and *Gardner et al.* [12] both covering complementary aspects of the field.

Traditional visible light microscopy often requires specific histological staining to reveal morphological patterns in biomedical samples. This requires separate sections for each marker of interest, whereas vibrational spectroscopic imaging can potentially provide information on various markers at once, from a single section of unstained tissue.

Raman microspectroscopy, although able to provide high resolution chemical mapping of cells and tissues, is either significantly slower than MIR imaging, or when used in fast non-linear modalities [13] has less chemical information. The non-linear modalities such as coherent anti-stokes Raman scattering (CARS) or stimulated Raman scattering (SRS) are mostly limited to probing only the higher wavenumber region of a vibrational spectrum while being more complex in optical setup compared to a discrete frequency MIR imaging system. Notable however is their ability to perform better in aqueous media than MIR systems which makes them superior for studying living organisms but less favourable for studying clinical samples.

Mass spectrometry based imaging techniques [14, 15] offer a comparably good chemical contrast to MIR and Raman imaging but are significantly slower, more expensive in

operation, and notably destructive. In comparison to other techniques, MIR imaging offers high sensitivity, reasonable spatial resolution (of the order of 1-10 µm), non-destructive testing and specific chemical contrast without the requirement of extensive sample preparation.

In simplistic terms, the four key components of a MIR imaging system are the light source, the imaging optics e.g. microscope, the wavelength separating unit or spectrometer, and the detector.

All novel developments in each of these areas are be discussed and the implications for MIR hyperspectral imaging of histological tissue sections considered. The focus lies on farfield techniques, likely to be applied to large scale tissues and cells at scales of 10‘s µm to mm. There are many rapid developments in nearfield IR techniques, beyond the scope of this introduction, such as scanning near-field optical microscopy (SNOM) or nano-IR, the reader is pointed to a review by *Bazylewski et al.* [16] for a general overview or others for more specific nano-IR applications [17–23].

Integration of the new IR technologies into an imaging system, often using coherent light sources, can require careful consideration of the impact of the optical systems on the imaging quality achieved, particularly when trying to achieve diffraction limited spatial resolution. Designing an imaging system is a complex task and needs to consider all requirements and components to maximise performance. The most important parameters in a spectral measurement are the spectral range (defined by the light source, optical components, and detector), spectral resolution (either defined by a spectrometer, wavelength tuning element or inherently from the linewidth of the monochromatic excitation light), spatial resolution (defined by the objective‘s numeric apeture) and speed (given by brightness of the light source, speed of wavelength selection and sensitivity of the camera). Here it is discussed, how each new instrumental approach is likely to affect those parameters.

2.2 MIR Light Sources

The light source is a key component of MIR imaging systems and its choice has a major influence on the rest of the system design. To date, only two types of radiation source can be seen as well-established sources for MIR spectroscopy and imaging: globar and synchrotron illumination. In recent years, additional technologies have become available in the MIR region. These include: quantum cascade lasers (QCL), MIR supercontinuum light sources, optical parametric oscillators (OPO) and free electron lasers (FELs).

A globar is the simplest and cheapest broadband light source. It consists of a filament made of silicon carbide which is heated up to 1000 to 1650 °C by an electric current and radiates according to Planck's law (i.e. as a black-body). The output radiation is spatially and temporally incoherent, and has very low intensity noise, being limited by the drive current and the stability of the cooling system. It has a large spectral emission range (2-25 µm) but low spectral intensity (radiant intensity per wavelength) stemming from the principle of black-body radiation.

Synchrotron radiation and free electron lasers (FEL) are easily able to cover the whole MIR spectral range with significantly higher brightness than globars. Their working principle is based on the Bremsstrahlung effect, whereby electrons are accelerated to relativistic speeds while the transverse part of their momentum is modulated by a magnetic field (e.g. by an undulator or bending magnet) leading to emission of electromagnetic radiation in a cone, spanning a wide range of wavelengths. While the undulator induced radiation is inherently incoherent with arbitrary phase relation, some designs [24] can achieve coherence over certain spectral ranges in the far-IR. Free electron lasers emit coherent radiation in both spatial and temporal domain [25, 26]. The FEL from Tokyo University of Science, for example, emits a selectable wavelength in the range 5-16 µm [27]. It can operate at 5 Hz repetition frequency and macro-pulse duration of approx 2 μs, which actually consists of a set of 2 ps micro-pulses with 350 ps periodicity, delivering 6-8 mJ per macro-pulse. FELs as well as synchrotrons are extremely large and expensive to maintain; therefore, they are available only for a few experiments in the basic sciences. High costs and lack of portability of these systems make them impractical for general use. Other notable MIR light sources [28] are solid state lasers and fibre lasers but will not be discussed further here. They can offer extremely high peak power and ultrashort (fs) pulses, but, at the expense of cost and bulk.

The most promising commercially available new technologies are MIR semiconductor lasers and supercontinuum light sources, as they combine high brightness and small size requirements.

2.2.1 Quantum Cascade Lasers (QCL)

Since the first demonstration of a working QCL in 1994 by *Capasso et al.* [29] with peak power of 8 mW at 4.2 µm , the QCL concept has since been very successfully. By now, the peak power has risen to over 200 W [30]. In continuous-wave (cw) operation the average output power exceeds several watts [31, 32] as well. The emission spectral range has improved, and lasing has been demonstrated on spectral bands spanning from 2.63 µm [33–35] to 24.4 µm .

Similar to diode lasers (DL) and interband cascade lasers (ICL) [36], pumping of the laser is realised by applying a voltage across the QCL chip. Carefully designed periodic heterostructures as visualised in figure 2.1 enable electrons to move into an upper laser level in the conduction band, where these electrons undergo a radiative transition to a lower energy state, also within the conduction band [37]. Finally, the electrons exit the lower laser state by non-radiative transition and are re-injected into the upper laser state of the next cascade (period). After moving through all cascades, typically 30-40 within one laser structure, the electrons are collected at the positive contact. The electrons‘ wavefunctions are composed of spatially-modulated Bloch states of the conduction band during the entire process, so no holes are involved, which is not the case for DL and ICL.

Increasing the number of cascades can technically achieved total quantum efficiencies greater than 100 % because each cascade can result in up to one photon per electron [38] and the electron can be reused by the next cascade. The power efficiency is largely independent on the number of cascades, but increases with the cascade number due to better overlap of the optical mode with the gain. For high power, it appears that having 10-15 cascades [39] is optimum because of a need to balance thermal conductance with power efficiency. One can also enhance the emission range of a single chip by heterogeneous stacking of cascades with gain centred at different wavelengths [40–43].

To achieve individual energy levels, in an otherwise continuous band of energies, quantum confinement has to be established. This is realised by surrounding a thin (nm scale) layer of low bandgap material with a different lattice matched material of

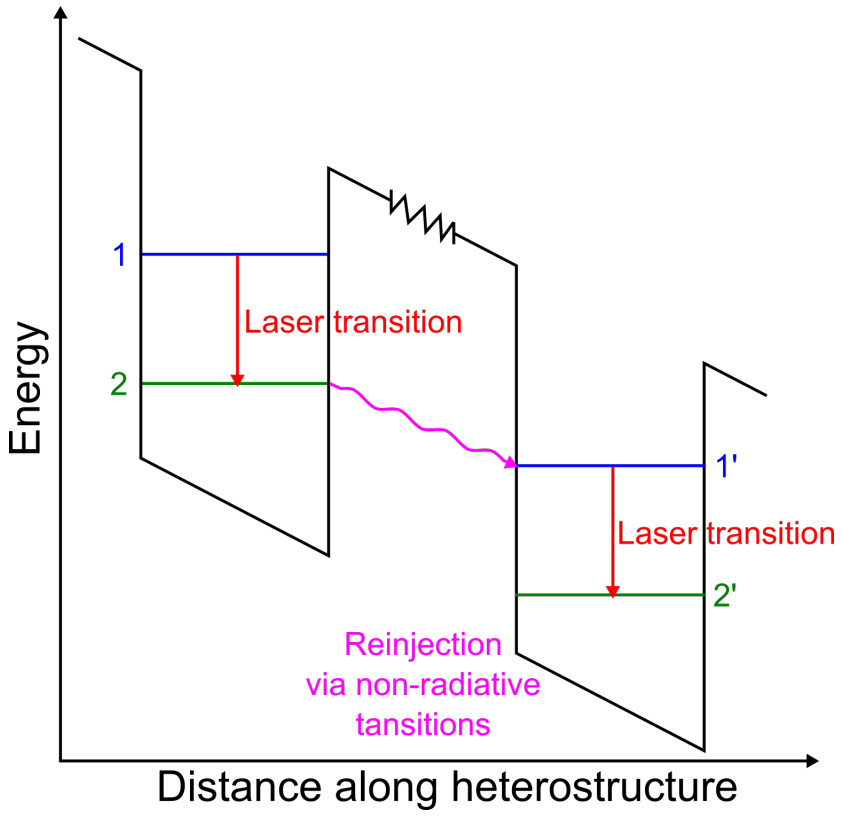

Figure 2.1: *Simplified QCL energy schematic.*

higher conduction band offset. This creates a quantum hole with individual energy levels along one spatial dimension. Additional energy levels need to be introduced into the sequence for proper functioning of the laser (e.g. for efficient depopulation of the lower laser state), resulting in a set of quantum holes and barriers. Such a set is called a period or a cascade, and as is apparent from its name they can be stacked together quite easily as the major carrier are electrons. By heterogeneous stacking of periods, a gain spectrum at different wavelengths can be designed. Therefore, those strucktures can be stacked periodically to form several pairs of quantum wells and barriers on top of each other. This cascading structure enhances the quantum efficiency of the process [38] and gives the lasers their name (QCL).

QCL chips emit a Fabry-Perot (FP) spectrum centred at a particular wavelength (design dependent) that can be broader than 10 % of the central wavelength. One way to achieve single longitudinal mode lasing is to etch a diffraction grating on top of the laser stripe, which acts as a distributed Bragg reflector (DBR) and provides feedback for a narrow band of wavelengths; such a laser is called distributed feedback laser (DFB). Tuning is achieved by either directly changing the temperature of the chip or by modifying its pumping current. This technique however only allows tuning of less than 1 % of the central wavelength [44]. To overcome this limitation, several DFB lasers with different grating periods can be manufactured on one chip. Lasing from 5.9 to 10.9 µm with over 50 mW peak power throughout a wide range of wavelengths has been demonstrated [40].

A different approach is to use just one stripe, but use an asymmetric sampled grating DFB with an additional amplifier section [45]. With this configuration, over 5 W power in pulsed operation at 4.8 µm and tunability of 270 nm (300 nm) has been achieved, as well as 1.25 W in cw operation. By combining these two approaches [43], thereby creating a set of 8 stripes with different sampled grating DFB with additional on-chip sections responsible for combining the beams, tuning from 6.2 to 9.1 µm has been demonstrated [43]. All the above mentioned designs emphasise probably the biggest benefits of semiconductor versus other laser types, i.e. small size, completely electronic tuning and enormous mass production potential.

Single mode lasing and tuning can also be achieved by mounting an FP laser into an external cavity (EC) [46]. Applying an antireflection coating on at least one facet of the QCL chip suppresses the FP modes and allows wavelength selection by tuning an optical element in the cavity. In Littrow and Littman-Metcalf configuration, a diffraction grating is utilised for this purpose, achieving laser line widths of below

$1\,cm^{-1}$[47, 48]. An alternative to this is the use of interference filters and retroreflectors. This has been successfully demonstrated [49] over a wavelength range of 4 - 4.3 µm and shows comparable results to grating based designs. If broader emission wavelength can be tolerated, acousto-optic modulators (AOM) and simple mirrors can also be used for tuning, thus achieving switching time between wavelengths under 1 μs [50] instead of several milliseconds, typical for micro-electro-mechanical systems (MEMS). Dual wavelength operation and tuning is also possible with AOM tuning [51].

EC-QCLs with tuneability in pulsed mode from 7.6 to 11.4 µm , with peak power of up to 1 W and average power of 15 mW have been realised [42]; higher powers have been achieved in the narrowed band of 7 to 8.9 µm with a maximum power of 200 mW [41]. Even by placing the QCL chip in these complex external cavities, the size is still reasonably small, of the order of a few tens of cm. However, the spectral range coverage of most commercially available laser chips is not sufficient to cover the full wavelength range of interest. To overcome this limitation, several individual EC-QCL chips are combined into a system with a common output port.

2.2.2 Supercontinuum Sources

Supercontinuum sources are well known to be powerful tools for microscopy and spectroscopy applications due to their high brightness and very broad spectrum. Supercontinuum generation was first demonstrated in bulk borosilicate glass by *Alfano and Shapiro* in 1970 [52]. In this process, narrow band optical pulses undergo significant spectral broadening through the interplay of a variety of non-linear optical effects in the propagation medium, yielding a spectrally continuous output. Optical fibres have proven to be particularly suitable for this purpose, as the light is strongly confined over long interaction lengths, which enhances the efficiency of non-linear effects. With the advent of fibre technologies such as high power pump diodes and gain fibres as well as the development of new optical fibre materials, geometries and dispersion profiles, it is now possible to design and build broadband supercontinuum sources at wavelengths from ultraviolet to the infrared [53, 54].

In recent years, a great deal of effort has been put into extending emission capability into the MIR. This pursuit requires the use of novel fluoride based fibres with transmission windows in the 2-5μm region and chalcogenide materials that allow supercontinuum generation extending to 13.3 µm [55, 56]. In the 2-4.5 µm region, power spectral density values of several hundred μW/nm have been reported [55].

Beyond 5 µm , experimental demonstrations have shown power spectral density levels of 1-2 μW/nm [57]. Simulations of alternative conversion schemes indicate that there is potential to achieve power densities of over 10 μW/nm at wavelengths as long as 10 µm [58]. However, it is worth noting that current commercially available MIR supercontinuum sources do not extend beyond a wavelength of 4.5 µm (around 2200 cm^{-1}).

Fibre based supercontinuum sources have a high inherent beam quality, enabling diffraction limited performance and high spatial coherence. Due to their large spectral bandwidth, supercontinuum sources exhibit extremely low temporal coherence effectively eliminating speckle in broadband illumination situations. However, applications that require narrow filtering of the supercontinuum may exhibit speckle [59].

Furthermore, fibre based MIR supercontinuum sources can be made compact, robust, and affordable ($50K-$100K) thus making them very attractive for practical applications. While only just appearing on the market, commercially available MIR supercontinuum sources are relatively inexpensive and can be purchased for comparable prices to those of current commercial turn-key QCL systems in the same wavelength range.

As supercontinuum sources are inherently broadband, their direct use for hyperspectral imaging requires a spectrometer or wavelength selection element. Utilising acousto-optic tuneable filters (AOTF), they can also be operated in a narrowband imaging scheme which has been demonstrated for wavelengths up to 4.5 µm [59, 60]. Yet, at any longer wavelengths, there are currently no commercially available AOTFs. Thus, the use of longer wavelength supercontinuum source requires an interferometer, monochromator or a novel upconversion scheme [61].

2.2.3 Optical Parametric Oscillators (OPO)

Optical parametric oscillators are a well-established technology for generating light in the visible spectrum but are more difficult to build for MIR applications. They are however particularly good at generating high intensity monochromatic radiation for spectroscopic purposes [62]. OPOs utilise difference frequency generation (DFG) between two laser beams referred to as pump and signal beams generating a third

beam referred to as idler beam. The frequency δ_i of the idler beam is determined by the law of energy conservation as difference of pump δ_p and signal δ_s frequencies:

$$h\delta_i = h\delta_p - h\delta_s \tag{2.1}$$

In order for the DFG to work efficiently all three beams need to conserve momentum ($\Delta k = 0$) which is referred to as phase matched. The phase mismatch is expressed as:

$$\Delta k = k_p - k_s - k_i = 2\pi \left(\frac{n_p}{\lambda_p} - \frac{n_s}{\lambda_s} - \frac{n_i}{\lambda_i} \right) \tag{2.2}$$

This principle allows to to build a DFG laser system with two input lasers. The system generates the desired idler beam by depleting the input signal and pump beams. An OPO system in contrast to that utilises the properties of quantum noise to generate signal and idler photon both from only one pump beam. The nonline crystal is placed in a cavity which is resonant to the signal wavelength. This principle however only works with sufficiently high pump laser power as the parametric generation of the signal needs to exceed the round trip loss of the cavity. Therfore, each OPO has a threshold pump power which needs to be surpassed in order to generate the desired idler photons.

Most OPOs utilize quasi phase matching created by special periodically poled non-linear crystals [63]. The crystals can be grown with a fanned poling structure effectively providing different refractive indices for different crystal positions. The generated wavelength is dependent on the refractive index. This effect can be used to coarse tune the output wavelength of the OPO by changing the refractive index, via temperature tuning, or by translating the crystal along the fanning direction. Fine tuning can be achieved by tuning the pump laser wavelength. The non-linear crystal is placed in a cavity which enhances the generated output [64–66].

Most OPOs built this way operate in the 2-5 µm wavelength range utilising periodically poled lithium niobate (PPLN) non-linear crystals. This configuration allows to build OPO systems with output power ranging from 100 mW up to 10 W limited by the damage threshold of the non-linear crystal [67].

2.2.4 Comparison

In summary, globars are still the most universal low cost option available to cover the entirety of the MIR spectral range of interest, but lacking brightness, especially for high resolution imaging. Synchrotrons and FELs are bright tuneable light sources, but very expensive and relatively inaccessible. Supercontinuum sources are close to performing as well as synchrotrons, but do not cover the full MIR spectrum with sufficient power. QCLs are becoming commercially mature (800 to 1800 cm^{-1}) and offer spatially and temporally coherent radiation in the longer wavelength MIR range, but may require a multi-chip design to cover arbitrarily wide spectral ranges. As QCLs are only available in the 6 to 12 µm wavelength range, OPOs are an alternative to cover the shorter MIR wavelength until QCLs in that wavelength range become available. For a further discussion of novel light sources in hyperspectral MIR imaging the reader is pointed to chapter 8.

2.3 MIR Detection Systems

A primary limitation for widespread exploitation of the IR spectrum for imaging applications is associated with a lack of sensitive, robust and easy to operate detection systems. In comparison to visible detectors, IR detectors generally suffer from noise originating from their own components emitting room temperature black-body radiation; hence, low noise performance can only be achieved through cryogenic cooling. Cold shields can be used to minimise the contribution from black-body radiation from surrounding objects entering the detector. Generally, light detection is based either on the absorption of photons by a sensor material resulting in a temperature increase which can then be detected (**thermal detectors**) or in the creation of electron-hole pairs giving rise to a current (**photodetectors**). Both these principles are routinely used for IR detection and can be considered mature technologies optimised for decades. Nevertheless, these detectors are still hampered by the need for cooling resulting in high operational cost, complexity and size for low noise operation. Recently, new types of detectors have emerged due to new technological achievements. These detectors have different working principles and can overcome traditional shortcomings for special applications.

2.3.1 Thermal Detectors

A thermal detector is based on the temperature increase produced by absorbed incident photons, which can be detected as a change in a temperature sensitive physical property of the material. These detectors generally have slow temporal response, often in the millisecond range, set by the thermal relaxation time of the sensor material. The spectral response of thermal detectors depends on the absorption characteristics of the material used. Thermal detectors are efficient for detection of high brightness signals, and can be operated without cryogenic cooling. One of the major sources of noise in thermal detectors relates to ambient thermal fluctuations transformed into a variation in the conductance of the sensor material. In general, thermal detectors need to have a low heat capacity for fast response time and good thermal isolation from the surroundings [68, 69]. Applications of thermal detectors are generally limited by their slow response time and lack of sensitivity, due to unwanted black-body radiation from surroundings and temperature fluctuation in the detector material particularly in the non-cooled versions. Thermal detectors are divided into different categories based on the physical property responsible for generating the output signal in response to the temperature variation. Two commonly used thermal detectors are presented below.

Bolometers The bolometer is a widely used thermal detector whereby the incident radiation is absorbed in the sensor material, increasing the temperature of the material relative to the surroundings. The sensor material has a temperature-dependent electrical resistance, which can be read out as a voltage when passing a current through the bolometer. The voltage can be expressed as:

$$\Delta V = IR\alpha\Delta T;\ \alpha = \frac{1}{R}\frac{dR}{dT} \tag{2.3}$$

α is the temperature coefficient of resistance of the sensor material that determines the sensitivity of the bolometer. Preferred materials for bolometers should have low heat capacity, low room temperature resistance and a large thermal coefficient of resistance.

IR imaging in the long wavelength regime, e.g. 8 to 14 µm , can be achieved using microbolometer arrays. These arrays consist typically of 320×240 pixels, however larger arrays with 640×512 pixels are emerging. The individual pixel dimension is of

the order of 20 µm × 20 µm ; however, as the pixel size decreases and thus the number of pixels per unit area increases, a larger noise equivalent temperature difference results due to smaller pixels being less sensitive to IR radiation [70].

Thermopiles The thermopile is another type of thermal detector, measuring temperature via a series of thermocoupled devices. An infrared absorption film is deposited on one side of the junction of a thermopile consisting of a series of thermocouple pairs. Each pair has a junction of two conductors on either side of a thermal resistance layer, resulting in a voltage in the range 10 to 100 mV proportional to the temperature difference:

$$\Delta V = N(\alpha_a - \alpha_b)\Delta T \tag{2.4}$$

α_a and α_b are the Seebeck coefficients, representing the magnitude of an induced thermoelectric voltage in response to a temperature difference across that material, of the two conductors forming the junction of the thermocouple pair. N is the number of thermocouple pairs and ΔT is the temperature difference caused by the absorbed IR radiation.

The sensitivity and the frequency response of thermopiles are inferior to bolometers, nevertheless thermopiles are cost efficient and have found several applications in the medical, farming and automotive industry [68, 69].

2.3.2 Photodetectors

The working principle of photodetectors is based on the photon absorption in a semiconductor material resulting in an electronic transition generating a free charge carrier. The bandgap of the semiconductor dictates the working wavelength range. Silicon (Si) is the preferred material for detectors in the visible and near-infrared (NIR) range, between 350 and 1100 nm. Moving towards longer wavelengths, indium gallium arsenide (InGaAs) is the detector material of choice covering the range between 0.85 and 1.7 µm [71]. Indium antimonide (InSb) can be used in the range 3 to 5 µm whereas mercury cadmium telluride (MCT) is commonly used in the wavelength ranges 3 to 5 and 8 to 12 µm [69, 72].

Generally, Si and InGaAs detectors can have very high quantum efficiency reaching more than 90 %, thus approaching single photon counting sensitivity, and have a rise time in the order of 10-100 picoseconds. In contrast, InSb and MCT based detectors typically have rise times in the order of 10-100 ns or more. The low bandgap energy of the IR detector has a great impact on the noise performance, both in terms of internal noise as well as sensitivity to black-body radiation originating from the detector surroundings. In practical applications were high sensitivity is needed, the InSb and MCT detectors are actively cooled in order to obtain low noise levels.

InGaAs and InSb Detectors Si and InGaAs detectors are divided into PIN diodes and avalanche photodiodes (APD). In both cases the detector operates in the reverse-biased region, which is known as photoconductive mode. The APDs work in the high voltage reverse-biased region, where the signal-to-noise ratio can be improved by the internal current gain due to the avalanche effect. APDs can be applied for single photon detection when operating in the Geiger mode.

A great variety of InGaAs detectors has been developed for different applications; Table 1 lists the properties of two typical APDs, working in the linear regime and Geiger mode, respectively. Generally for all detectors, there is a trade-off between high quantum efficiency, low noise and high bandwidth. InGaAs can also be applied for NIR imaging.

Compared to silicon-based cameras used for visible light imaging, InGaAs cameras suffer from higher dark current and larger readout noise as a result of the lower bandgap. InSb photovoltaic detectors reach further into the MIR than InGaAs systems and cover the wavelength range from 1 to 5.5 µm . They require to be cooled with liquid nitrogen like mercury cadmium telluride (MCT) detectors. Their noise performance is better than an MCT but as their spectral coverage is smaller they are rarely used for biomedical imaging applications.

Mercury Cadmium Telluride (MCT) Detectors MCT is an alloy composed of CdTe and HgTe. The absorption wavelength is determined by the amount of Cd in the alloy. MCT detectors can cover a relatively large wavelength range (2-12 µm), which makes them good candidates for Fourier transform infrared (FTIR) spectrometers.

MCT detectors have better performance than thermal detectors in terms of speed and noise, although they are still inferior to InGaAs detectors. However, MCT detectors

have been the detector of choice for MIR wavelengths, to which the InGaAs detectors are insensitive. The bandgap of MCT is smaller than that of InGaAs allowing it to detect longer wavelengths; however, this is also the main reason for the higher noise level. In practical applications, MCT detectors are usually actively cooled in order to reduce the noise.

2.3.3 Upconversion MIR detectors

Upconversion based detection is a fundamentally different approach for MIR sensing. Using upconversion the low energy MIR radiation is not detected directly. It is mixed with a high brightness laser in a transparent non-linear medium, shifting both the spectral and spatial information from the low energy MIR range to the NIR or visible range. This high frquency signal can be detected with sensitive and fast silicon technology detectors.

Using a transparent medium for the non-linear process also has the effect, that no black-body radiation from the medium is added to the MIR signal. Which is in strong contrast to direct detection where the medium has to be highly absorbing. Secondly, the non-linear process imposes a strong spectral and spatial filter to the upconversion process, limiting the spectral bandwidth and field of view of the detector, hence reducing the black-body noise picked up from the surroundings.

Upconversion is a parametric process and follows the principle of energy and momentum conservation (Equation 2.3 and Figure 2.2):

$$\frac{hc}{\lambda_{IR}} + \frac{hc}{\lambda_{pump}} = \frac{hc}{\lambda_{up}}, \quad \vec{k}_{IR} + \vec{k}_{pump} = \vec{k}_{up} \tag{2.5}$$

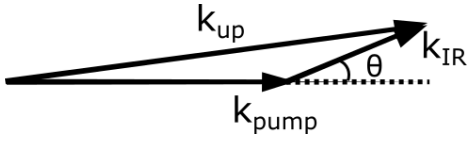

Figure 2.2: *Non-collinear phase matching diagram*

h is the Planck constant, c is the speed of light, λ_i and k_i are the wavelength and the wave vector for each specific photon. It should be emphasised that the phase matching

condition acts in all spatial dimensions; therefore, the upconversion photon preserves the spatial information of the IR photon, which enables upconversion imaging.

Upconversion technology has been deployed for both point detection [73] and for wide-field imaging configurations [74–76]. Recently, a conversion efficiency of 20 % has been demonstrated which presents the upconversion scheme as an emerging technique for MIR detection [77]. Figure 2.3 shows an example of upconversion-based measurement of MIR hyperspectral imaging.

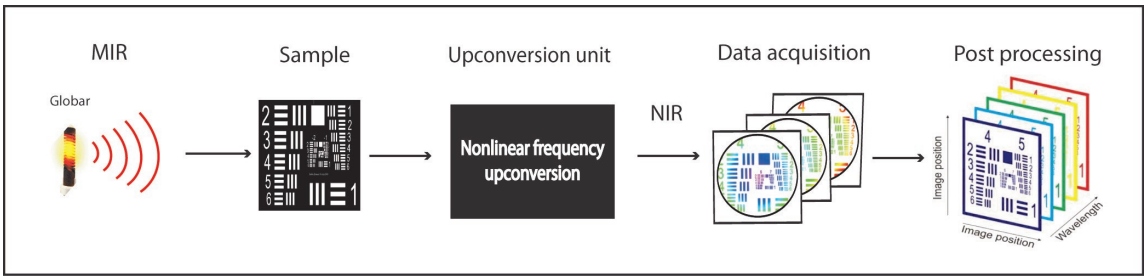

Figure 2.3: *A schematic of IR spectral imaging based on upconversion technology.*

Here, a globar is used as broadband illumination source, whilst an upconversion unit converts the transmitted radiation from the sample from MIR to NIR and a silicon-based camera captures the images. The acquired broadband images are then post processed to obtain a hyperspectral datacube made of a series of monochromatic images.

Upconversion can be used over a substantial part of the IR spectral range depending on the non-linear crystal used. Table 2.1 lists the properties of some commonly used non-linear materials for the upconversion.

Table 2.1: *Properties of nonlinear crystals for upconversion detectors.*

Nonlinear Crystals	**Transparency range (μm)**	**Nonlinear Coefficient (pm/V)**	**Thermal Conductivity (W/m-K)**
Lithium Niobate (LN)	1–4.5	14	4.6
Lithium Thioindate (LIS)	1–8	7	6
Silver Gallium Selenide (AGSe)	1–20	33	1
Silver Gallium Sulphide (AGS)	2–11	11	1.4

The choice of the non-linear material is very important for a given application, not only should the material be as transparent as possible to the IR wavelengths in order not to introduce thermal noise, but it should also be able to phase match the non-linear process while preferably having a high non-linear coefficient for efficient frequency conversion.

So far lithium niobate (LN) has been the preferred material for upconversion detection. It has been used in an intracavity configuration both for spectroscopic and imaging applications. It is, however limited by the transparency range (to below 4.5 µm). At wavelengths below 12 µm, silver gallium sulphide (AGS) has been used both for imaging [75] and spectroscopy [78]. AGS has very poor thermal conductivity, however, limiting its potential for intracavity configurations. In imaging applications thermal lensing within the crystal can cause distorions in images. Silver gallium selenide (AGSe) might be an alternative for longer wavelengths as well. AGSe can only be phase matched with longer mixing wavelengths, from 1.9 µm upwards. Consequently it needs to be combined with InGaAs detectors rather than Si detectors, thereby increasing the overall cost and complexity of the system.

Upconversion detection has also been demonstrated using periodically poled LN waveguides (PPLN-W). Comparing PPLN-W with upconversion in the bulk non-linear crystals, high internal conversion efficiency in PPLN-W can readily be achieved even with modest mixing powers due to the spatial confinement of the interacting fields inside the waveguide [73, 79]. If a broadband illumination source is used, the spectral resolution of the system can be set by the phase matching properties of the non-linear process.

For an upconversion imaging set-up, the spatial resolution is primarily determined by the beam diameter of the mixing field. It serves as a soft aperture in the imaging system. Both the spatial and spectral resolution of the imaging system depend on the IR input wavelength [74, 80].

Upconversion detection has a very small acceptance angle, which can strongly inhibit the ambient noise. In contrast, conventional detectors need a cold shield to block the ambient radiation from almost 2π solid angle.

A potential source of noise for upconversion systems is false MIR photon generation through a spontaneous parametric down conversion process (SPDC). These MIR photons are indistinguishable from the signal MIR photons. The upconverted SPDC

noise is roughly quadratically proportional to the pump power. This results in pump power having a trade-off term between high conversion efficiency and low-noise.

Further techniques utilising quantum phenomena with potential to improve MIR imaging technology are induced quantum-coherence imaging [81] and field-resolved spectroscopy [82, 83], although they have not been applied to real world samples yet.

2.4 Mid-Infrared Micro Spectroscopy

The spatial resolution of an IR microspectroscopy setup is defined by the wavelength and the collection optics in combination with the pixel size of the camera.

The choice of the optical setup is heavily dependent on the light source and detection system. For incoherent light sources such as a globar, the use of reflective optics is generally considered favourable. Most commercial FTIR microscopes employ Schwarzschild optics [84] which consist of a matched pair of Cassegrain objectives (figure 2.4A).

The Cassegrain objective has a central convex mirror that is held in place by a spider mount reflecting the incoming beam onto a secondary concave mirror above it. The secondary mirror focuses the beam onto the sample. This configuration can correct for spherical aberration, coma and astigmatism over a wide range of wavelengths [85]. Moreover, the Cassegrain objective can be used as a solid immersion objective, with higher magnification and higher numerical aperture than common lenses by the use of a high-refractive index crystal e.g. germanium ($n \approx 4$), hence increasing the spatial resolution [86].

Reflective optics only suffer from minimal broadband absorptions and thus usually give higher flux than refractive optics. Furthermore, they are not subject to chromatic aberrations. Therefore, Schwarzschild optics have proven to be most economical for non-coherent imaging. The central mirror and the spider legs holding it in place, however, can cause obscuration of the image, which is negligible for incoherent light sources but can be a problem with coherent ones [87]. Coherent light sources usually have higher brilliance, leading to more intense focused beams. Therefore, some losses due to lower optical throughput of refractive optics can be tolerated when considering the gain in imaging quality using these sources. Furthermore, the benefit of not having obscuration outweighs the loss of flux.

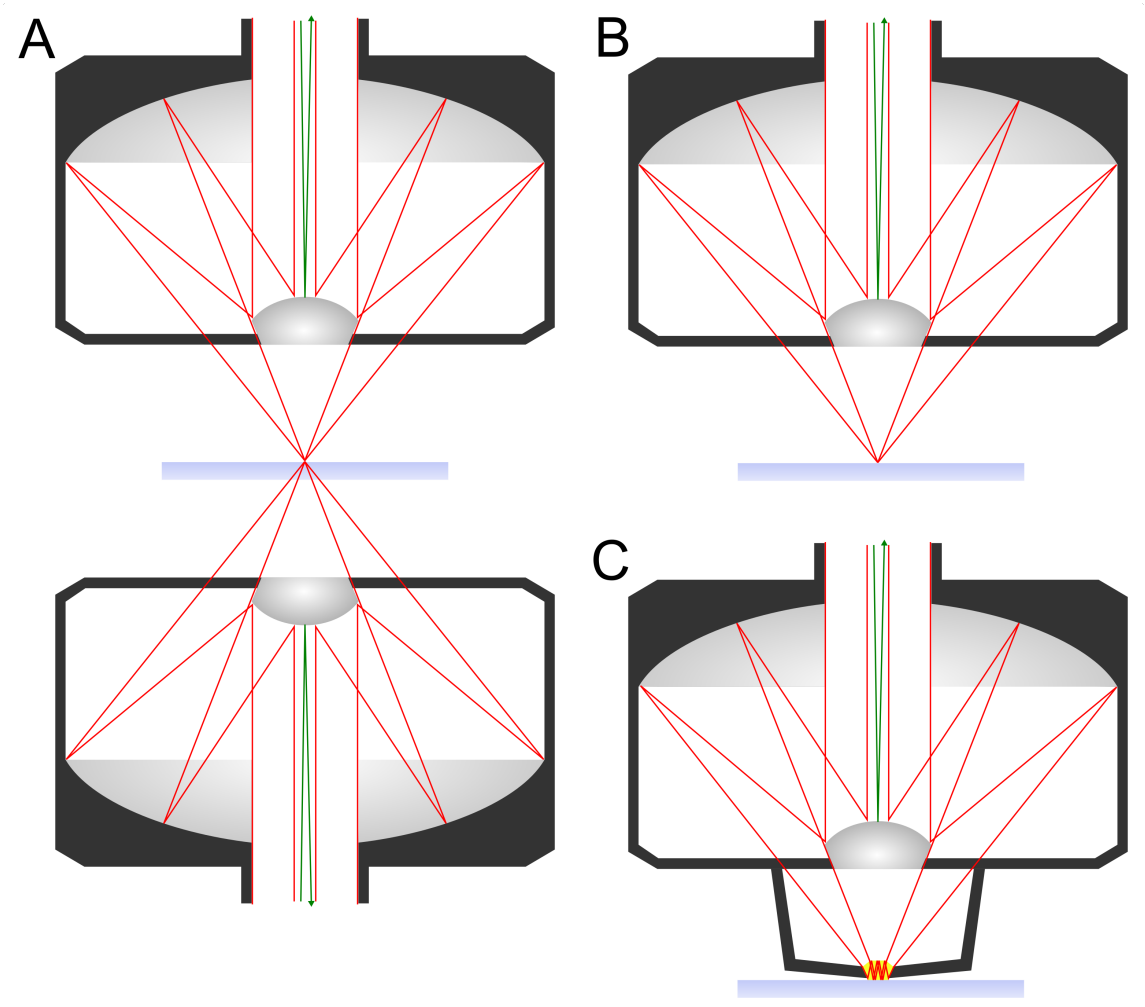

Figure 2.4: *Schematic diagram of three distinct optical configurations for MIR hyperspectral imaging. The beam path is outlined in red lines and the central obscuration in green lines. A: Set of Schwarzschild objectives used in transmission mode. B: Schwarzschild objective used in transflection mode. C: Combination of Schwarzschild objective with ATR crystal for total internal reflection mode*

MIR microspectroscopy can be realised in three different configurations, as shown in figure 2.4. In transmission mode, the sample is illuminated via a condenser and the transmitted light is collected in forward direction by a second objective (figure 2.4A). Here, the relevant optical path length is given by the thickness of the sample. To collect light in backward configuration, samples can be mounted onto reflective substrates, so that the one objective serves as focusing and collection optic at the same time. The beam is focused onto the sample, is reflected by the substrate, passes the sample a second time and is collected by the objective (figure 2.4B).In this case, the optical path length is twice the thickness of the sample.

The third way to realise imaging is by attenuated total reflection (ATR) using a high refractive index crystal as an internal reflection element, (IRE). For this purpose, an ATR crystal is placed in contact with the sample, and the IR beam is directed into the crystal and is internally reflected at the interface between the crystal and the sample (figure 2.4C). This results in an evanescent wave propagating orthogonally to the surface into the sample. Some of the energy of the radiated field is absorbed by the sample, resulting in an attenuation of the light reaching the detector. When the critical angle ($\Theta_c = sin_{-1}(n_2/n_1)$), where n_2 and n_1 are the refractive indices of the sample and the crystal, respectively) is exceeded, a purely ATR spectrum is observed. In this configuration, the optical path length depends on the refractive index of the ATR crystal. Valuable reviews have been published by Kazarian and co-workers on advances and applications of ATR-FTIR spectroscopic imaging to biomedical samples [88, 89], and pioneering work in biomedicine [90] includes the application of this technology to the studies of atherosclerosis [91–93].

The choice of sampling mode has major influence on the sample preparation required. Imaging in ATR mode requires the least sample preparation as the crystal is simply pressed onto the sample. The effective sampling volume depends on the internal reflection elements refractive index (n_1), the samples refractive index (n_2), the wavelength (λ) and incident angle (Θ) The penetration depth of the IR beam is given by equation 2.6 reaches around 1-3 µm into the sample [88].

$$d_p = \frac{\lambda}{2\pi n_1 \sqrt{\sin^2 \Theta - \left(\frac{n_2}{n_1}\right)^2}} \tag{2.6}$$

Transmission and transflection modes however require the sample to be mounted on a transmissive or reflective substrate. For transmission mode, monocrystalline calcium fluoride (CaF2) or barium fluoride (BaF2) slides are the optimal substrate. These substrates are expensive (>100$/slide) and brittle. Transflection measurements require reflective substrates. The most common way to achieve this is by coating glass slides with either gold or a low-emissivity (low-e) coating consisting of a very thin aluminium layer covered by a thin oxide layer. Those substrates are cheaper (< 5$/slide) than the monocrystalline ones commonly used for transmission IR.

Apart from the difference in the sample preparation, the sampling geometries can cause different effects in the spectra. Whereas influential factors on the image itself are well understood, there are furthermore important effects with regard to the spectral domain, which are less recognised. The aim in MIR imaging is to obtain transmission/absorption spectra from the samples. In the microscopy case, this aim can be perturbed by the fact that features of interest are of the same order of magnitude in size as the wavelength used for probing. Therefore, Mie scattering [94] can be observed in some cases. *Bassan et al.* developed an algorithm to correct for spectral distortions caused by Mie scattering, also incorporating resonance effects [95], i.e. related to the change in imaginary refractive index at spectral absorbance peaks. The algorithm has recently been further optimised by *Konevskikh et al.* [96, 97].

In transflection sampling, a different type of spectral distortion first referred to as electric field standing wave effect (EFSW) was reported by *Bassan et al.* [98], *Filik et al.* [99] and *Wrobel et al.* [100, 101]. A rigorous investigation of the theory by *Joe Lee* [102] however proposes that these effects are not due to a standing wave in the classical sense but can rather be explained by interference between reflections from a variety of different sample planes.

The formation of an image can be achieved in several ways; the two most common commercially available approaches are wide field imaging and point scanning. In wide-field imaging, the image is obtained by combining optics with a camera to obtain spatial resolution [103]. Hyperspectral information can then be obtained by introducing an interferometer, or wavelength filter into the beam path or by using a tuneable monochromatic light source and collecting individual images at several wavelengths. In point scanning, the light is focused into a diffraction limited spot, which is scanned across the sample [104]. The transmitted or transflected radiation can then be recorded on a single element detector. Spectral resolution can be obtained in the same fashion as in wide field imaging as well as by using a diffraction element and

dispersing the spectrum onto an array or line detector. Note that this latter approach should be described as mapping rather than imaging. For diffraction limited imaging, a wide-field approach is easier to realise and usually allows for faster data acquisition than point scanning. Point scanning systems have a much higher requirement on mechanical stability and therefore are more difficult to construct. If a coherent light source is used, a point scanning system is not affected by speckle. The spatial and phase variation in the beam wavefronts and associated interference are not resolved in point scanning, as they would be in a wide-field imaging system.

There are major differences in the nature of data obtained by discrete frequency (or monochromatic) sources and continuous sources. Continuous or broadband sources are most often used with interferometers, to take benefit from the Felgett and Jaquinot advantages [105]. In this work, these systems are referred to as Fourier transform (FTIR) spectrometers and the resulting data as FTIR spectra or data; whereas datasets of discrete sources will be referred to as discrete frequency IR (DF-IR) data.

FTIR data are essentially hyperspectral images with over 100 frequencies [106]. They also have the property that the bands are highly contiguous, while DF-IR images generally consist of images at much less than 100 discrete wavelengths. For hyperspectral images this means that each pixel can be represented as a spectrum, while for DF-IR or multispectral images this is not always the case. A comparison between hyperspectral and multispectral images is shown in figure 2.5.

The contiguous nature of the bands in IR spectra forming hyperspectral images allows application of a range of multivariate analysis techniques to extract the relevant chemical information. A hyperspectral dataset can be thought of as a data cube, with two spatial dimensions (x, y) and one spectral dimension (z). By unfolding the cube into a two-dimensional array, where each row represents the spectrum recorded for a single pixel, standard multivariate approaches can be applied. Refolding the processed array into a cube allows visualisation and interpretation of the data in the image domain that may not be possible otherwise, while the multivariate analysis allows for interpretation in the spectral domain, as well.

Absorption of radiation occurs at IR frequencies that match the vibration frequency of chemical bonds in the molecules of the sample. The transmittance or proportion of light transmitted through the sample, T, is calculated as the ratio of the intensity of light passing through the sample I to the intensity of a background or blank I_0. In

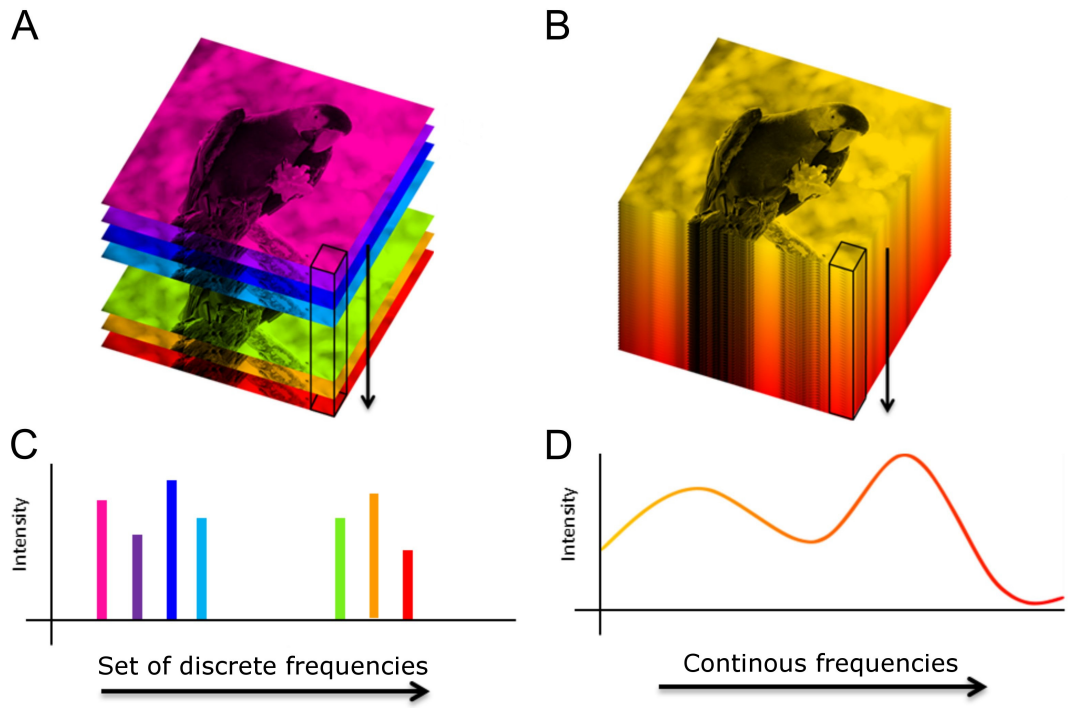

Figure 2.5: *Illustration of (A) a multimodal multispectral image and (B) a single mode hyperspectral image. (C) and (D) are the intensity profiles for the pixels indicated in (A) and (B), respectively.*

microspectroscopy, the background is typically a clean area of the transparent slide or substrate used to hold the sample:

$$T = \frac{I}{I_0} \tag{2.7}$$

The transmittance is related to absorbance by a simple logarithmic transform:

$$A = -\log_{10}\left(\frac{I}{I_0}\right) = -\log_{10}(T) \tag{2.8}$$

Multivariate analysis commonly assumes the Beer-Lambert law to be valid for this application. It states that the absorbance A at a given wavelength is proportional to the analyte concentration c:

$$A(\lambda) = a(\lambda) \cdot b \cdot c \tag{2.9}$$

where $a(\lambda)$ is the wavelength dependent molar absorption coefficient of the sample material and b is the optical path length. Many multivariate approaches assume linear relationships between variables, and using the Beer-Lambert law the results can be interpreted in terms of concentration. This provides quantitative analysis for the absorption spectroscopy data.

3 Hyperspectral Data Analysis

Disclaimer: This chapter is an adaptation from a review paper entitled: 'Mid-IR hyperspectral imaging for label-free histopathology and cytology' publish by the author of the thesis and collaborators in the IOP journal of optics [1]. The review is published licensed under Creative Commons Attribution 3.0 licence which allows reuse and remix of content. The following chapter is remixed from sections: 5. Hyperspectral data analysis and 6. Biomedical applications. The descriptions of EMSC; PLS and LDA have been further elaborated from the review paper as these techniques are most relevant to this work.

3.1 General Spectral Preprocessing Methods

A number of preprocessing steps are often required prior to undertaking detailed multivariate analysis of hyperspectral images in order to obtain meaningful results and interpretation. This section focuses on methods to analyse the spectral domain i.e. the unfolded data cube. These techniques have been developed in the context of FTIR data and some of them harness the continuous nature of the data, therefore application to DF-IR has to be considered with caution.

3.1.1 Normalisation

A key assumption when using the Beer-Lambert law is that the optical path length b (and molar absorption coefficient) is the same for each pixel. For histopathology applications, where the sample is a tissue section cut by microtome, variations in the sample thickness across the section result in a different path length. A normalisation step is therefore essential for comparing variations in absorption between pixels in an image. One simple approach is vector normalisation, which maps the spectra onto a unit sphere in multivariate space [107]. Other approaches include normalisation to constant total [107] and min-max normalisation, which scales each spectrum to between 0 and 1. Normalisation, however can have the disadavantage, especially

in imaging, that pixels with lower signal will be given less weight. This propagates to subsequent multivariate analysis, potentially masking important variations of compositional changes related to pathology.

Another common approach to normalisation in MIR spectroscopy is Multiplicative Scatter Correction (MSC) [108]. It attempts to account for scaling and offset effects by calculating a least-squares-fit of the measured spectrum to a reference spectrum. The measured spectrum is then corrected, the using the slope and offset of the fit. Extended Multiplicative Scatter Correction (EMSC) has been described that allows for normalisation, baseline subtraction and filtering of unwanted signals in a single step [109, 110]. Examples of application of EMSC in histopathology include Resonant Mie Scatter EMSC (RMieS-EMSC) [111] and paraffin removal [112, 113].

Standard Normal Variate (SNV) has also been suggested as an alternative method for normalisation [114]. SNV centres a spectrum and scales it by its own variance. SNV gives more weight to values in the spectrum that deviate most from the mean value, which for FTIR corresponds to peaks in the absorbance spectrum. It is usually most successful when the spectra are quite similar e.g. between pathology groups. It has been shown that SNV and MSC are mathematically very similar [115, 116].

3.1.2 Baseline Subtraction

In some cases there is unwanted background signal in the spectra forming an image. Specific approaches for background removal of signals due to atmospheric water vapour and resonant Mie scattering are discussed separately. For more general problems involving an undulating baseline, a polynomial subtraction approach can be used to subtract a best fit of the baseline. An iterative refinement of this approach is described in [117]. Sometimes the baseline will be too complex and a polynomial will not be capable of fitting the baseline without resorting to high orders that will over or under correct in some areas while fitting well in others. Approaches such as the rolling ball algorithm [118] and asymmetric least squares [119–121] may then be more appropriate. A comparison of various baseline methods for spectroscopic calibration has been published by *Liland et al.* [122].

3.1.3 Derivative Spectra

In microspectroscopy for histopathology the complexity of the sample, consisting of potentially thousands of biochemical signatures, results in highly complex IR spectra with multiple overlapping peaks. A common and highly successful approach is to use derivative spectra; the use of 2nd order derivative spectra is particularly prevalent [123]. This has two advantages: firstly, some baseline is removed without resorting to the methods described earlier (though this is limited to the derivative order minus one) and secondly it emphasises the shoulders of broad peaks when applying multivariate analysis. Disadvantages include making interpretation of subsequent analysis more difficult and emphasising noise. A Savitzky-Golay filter [124] is often used to calculate the second derivative and has the added advantage of smoothing at the same time, thereby reducing the impact of noise.

3.2 Specific Preprocessing Methods in Biospectroscopy

3.2.1 Atmospheric Water Vapour Removal

It is common practice to equip FTIR instruments with desiccant and a purge box to reduce the effect of absorption peaks from the atmosphere, in particular water vapour and carbon dioxide (CO_2). Fortunately, the position of the CO_2 peak at 2300-2400 $cm^{-1}$is well outside the typical 'fingerprint region' and 'high wavenumber region' (1000-1800 $cm^{-1}$and 2600-3800 cm^{-1}, respectively) and this region can simply be excluded. The effect of water vapour is however more serious as it overlaps with the fingerprint region, has numerous sharp peaks (associated with the rotational structure of the vibrational bending and steching modes) and is highly variable. Research is ongoing to explore methods to compensate for the presence of water vapour in the spectrum [125–127], and there have been some successful applications [128]. Perkin Elmer includes a patented method for Atmospheric Vapour Compensation (AVC) in the software for their FTIR systems that is based on a simulated water vapour spectrum with very high spectral resolution [129, 130].

3.2.2 Resonant Mie Scatter Extended Multiplicative Scatter Correction (RMieS-EMSC)

A known problem when using MIR spectroscopy to examine biological samples, particularly cells, is that the light has a similar wavelength to the diameter of particles (or cells) in the sample. This causes scattering, known as Mie scattering, which appears as a strong sloping baseline in the spectra of the sample. The scattering also contributis to distortions in the spectral peaks (with artefacts such as derivative shaped absorbance bands) resulting in small shifts in the peak wavenumber positions of important biomolecules such as proteins, making peak assignment and interpretation unreliable. In histopathology and cytology samples, the total Mie scatter is generated by contributions from a range of particle sizes and other properties making it difficult to compensate for.

Several attempts have been made to correct for Mie scattering contributions to FTIR spectra [131, 132], but the most popular approach uses a model for Mie theory that includes resonance [95]. First published in 2010 [111], the RMieS-EMSC algorithm incorporates a principal component model of resonant Mie scatter spectra generated from a theoretical basis into the standard EMSC algorithm as an interferent matrix (see below). Because the calculated scatter depends on the input spectrum, repeated applications of the algorithm have been shown to improve the correction but at the expenses of a considerable increase in computation time, particularly for hyperspectral datasets that contain tens of thousands to millions of spectra. An approach using graphical processing units (GPUs) to parallelise the correction algorithm has been suggested as a way of mitigating this problem [111], but currently adds a level of complexity and expense that might prevent clinical uptake.

3.2.3 Paraffin Removal

Motivated by the need to work with the current histological pathway, which involves formalin fixed, paraffin embedded tissues, some research groups have examined the possibility of using paraffin embedded sections. Some studies have used fresh frozen tissue because paraffin wax has a strong FTIR spectrum with peaks in the fingerprint region. Approaches investigated so far include chemical removal of paraffin using solvents such as xylene and hexane [133, 134] or chemometric methods that involve an EMSC step with a principal component model of paraffin wax spectrum as an interferent matrix [112]. *Nallala et al.* demonstrated that the EMSC approach is as

good as or better than the chemical removal of the paraffin contribution to FTIR microspectroscopy data of human colon tissue sections [113].

The EMSC utilises prior chemical knowledge of the samples by feeding in reference spectra for paraffin. It decomposes a measured spectrum ($\mathbf{Z}^{n\times p}$) assuming it consists of a linear combination of 'theoretical' spectra representing the chemical composition of the sample.

A single spectrum therefore, is decomposed into 'theoretical' spectra ($\mathbf{Z}_{chem}^{(n\times i)}$) referred to as loadings and scores an of those components ($\mathbf{B}^{(n\times i)}$), as well a residual error term $\mathbf{E}^{(n\times p)}$:

$$\mathbf{Z}^{n\times p} = \mathbf{B}^{(n\times i)}\mathbf{Z}_{chem}^{(n\times i)} + \mathbf{E}^{(n\times p)} \tag{3.1}$$

The index i denotes as the total number of components used for modelling, n denotes as the number of data points per spectrum and p is the number of spectra which are corrected. If any pure component spectra are known, they can be directly used for modelling; otherwise, they can be estimated using a principal component analysis or similar technique. $\mathbf{Z}_{chem}$ can be decomposed into a part worth retaining ($\mathbf{Z}_{retain}$) and one to discard ($\mathbf{Z}_{discard}$). Since only $\mathbf{Z}_{retain}$ needs to be retained equation 3.1 can be rewritten as:

$$\begin{aligned}\mathbf{Z}_{retain} &= \mathbf{Z} - \mathbf{B}_{discard}^{n\times i_{discard}}\mathbf{Z}_{discard}^{i_{discard}\times p} \\ &= \mathbf{B}_{retain}^{n\times i_{retain}}\mathbf{Z}_{retain}^{i_{retain}\times p} + \mathbf{E}\end{aligned} \tag{3.2}$$

If $\mathbf{Z}_{retain}$ is retained, any wavelength dependent changes can be corrected and contributions from perturbation components such as paraffin can be removed. Furthermore, the $\mathbf{B}$ term can be utilised to estimate concentrations of the components in $\mathbf{Z}_{chem}$ [135]. A more detailed introduction of EMSC and related techniques can be found in [136, pp. 139-160].

3.3 Visualisation and Exploratory Analysis

Although all of the multivariate methods described in this introduction ignore spatial information, it is still advantageous to interpret the information in the image domain in order to give some biological context. For example, it would be very difficult to identify a spectrum as being from a cell nucleus if it is not possible to see it in the context of the surrounding cell. The following methods are the most commonly applied for microspectral histopathology.

3.3.1 Intensity Based Images

Any approach that generates a value 'per pixel' can be used to visualise a hyperspectral image by refolding the result into an array with the same spatial dimensions as the original hyperspectral image. For example, maximum intensity, intensity at a single wavenumber or a fit coefficient from EMSC can all be used to generate intensity-based images. A false colour image can then be obtained in order to allow interpretation. Care should be taken to ensure that outlier pixels and the chosen colour table or bar do not unduly influence the visualisation and interpretation of the image [137]. Colour tables with discrete step changes in colour, rather than shade, should be discouraged for this reason.

3.3.2 Principal Components Analysis (PCA)

PCA is a data reduction technique that decomposes a dataset into a set of linearly uncorrelated variables called principal components (PCs) [138, 139]. PCA is useful in hyperspectral image analysis [140] because it provides information about the pixels in the form of principal component scores and the corresponding biochemistry in the loadings (see section 3.4.1 for mathematical details). Because the scores for each component are per-pixel, they can be refolded into intensity images (see figure 2.5). In addition, examining the loadings for that component alongside the scores-based intensity image allows interpretation in both spectral and image domains. For histopathology applications, this enables spectral differences between pathology groups, for example, to be discussed in terms of biological structures in the tissue section. This is vital for comparison with standard histology that relies almost entirely on interpretation of the biological structures and only uses the biochemistry as a

means to improve image contrast through the application of chemical stains such as haematoxylin and eosin (H&E).

PCA outputs are the principal components listed according to a decreasing order of explained variance. Alternative approaches include Minimum Noise Fraction (MNF) [141, 142] and Min/Max Autocorrelation Factors (MAF) [143] which order the components by signal-to-noise ratio.

PCA is applied as a processing method or, more often, as a preprocessing step before a classification method such Linear Discriminant Analysis (LDA) or Support Vector Machines (SVM) is applied. Including a PCA step reduces the influence of noise (by excluding components) and prevents over fitting by reducing the number of variables in the model, by combining those collinear variables found in the dataset together in one principal component, leaving only orthogonal components.

3.3.3 k-means Clustering

k-means clustering is an exploratory algorithm that aims to divide the spectra into k groups, or clusters [144]. Each spectrum belongs to the cluster with the nearest mean, or centroid. Its primary use in hyperspectral imaging is as a form of visualisation. Clustering creates a new vector that contains a value indicating the cluster membership of each pixel. An image can then be generated by shading each pixel according to its cluster membership. In image processing terms, the image has been segmented and is now easier to interpret. For histopathology applications, not all of the clusters will be relevant and all spectra associated with those clusters can now easily be removed from further analysis.

k-means clustering does have some disadvantages. For example, it can be difficult to choose an appropriate value for k i.e. the number of clusters. Too few and the segmented image is not informative, too many and the clusters represent noise. Methods such as the silhouette width [145] exist to try and solve this problem but are often computationally intensive and can overestimate, or underestimate the number of informative clusters.

In histopathology applications, in particular, the value of k that generates meaningful clusters biologically is often much larger than the number determined by the silhouette width. Other disadvantages include initialisation, which may result in different

clustering each time the algorithm is applied to the same image, and the inability to use any distance measure other than the Euclidean distance.

Modifications such as k-mediods [145] have been proposed to allow for the use of alternative distance measures, and other extensions are available such as Fuzzy C-Means (FCM) [146, 147]. They allow for soft-cluster membership i.e. each pixel has some degree of membership to all clusters. Spatially-guided FCM (sgFCM) [148] takes into account both the spectral and spatial information during clustering.

Furthermore, clustering performed on separate hyperspectral images often leads to regions with similar spectral signals being allocated to clusters with spectrally different centroids and colours in the different images. Common k-means on the whole dataset can overcome this problem at the expenses of significant computing resources. Self-Organising Maps (SOM), an unsupervised neural network [149], has also been used as alternative form of clustering for microspectral histopathology [150].

3.4 Predictive Modelling

A longstanding goal of microspectral histopathology has been to make predictions for the detection of disease. In a data analysis context, this is usually framed as a classification problem. Applied approaches include Linear Discriminant Analysis (LDA) [107], Partial Least Squares-Discriminant Analysis (PLS-DA) [151, 152], Support Vector Machines (SVM) [145, 153], Random Forests (RF) [154] and Neural Networks (NN) [155]. In this thesis only Partial Least Squares Linear Discriminant Analysis (PLS-LDA) has been used and therefore will be explained in greater detail in the following. For the understanding of PLS the concept of Principal Component Regession (PCR) is crucial and hence PCR is explained first.

3.4.1 Principal Component Regression (PCR)

A Principal Component Analysis (PCA) as briefly explained in section 3.3.2 can be used to extract latent variables from a high dimensional space.

To apply PCA to a set of spectra, the spectra need to be expressed as matrix. Assuming an ideal and noise free case this matrix ($\mathbf{X}$) would be expressed as linear combination of the spectra from pure components ($\mathbf{S}$) and their concentrations ($\mathbf{C}$):

$$\mathbf{X} = \mathbf{C} \times \mathbf{S} \tag{3.3}$$

Hence, the rank of $\mathbf{X}$ is defined by the number of components (number of spectra in $\mathbf{X}$). If there are more spectra in $\mathbf{X}$ than in $\mathbf{S}$ equation 3.3 becomes an overdetermined system. In this case $\mathbf{S}$ as well as $\mathbf{C}$ can be estimated from $\mathbf{X}$ if the chemical rank given by the number of components is smaller than the numerical rank (more spectra measured then different chemical components present).

PCA allows to perform such a decomposition of $\mathbf{X}$ on real data which has noise in addition to the chemical components. It is important to note however, that the results of PCA are not equivalent to real pure component spectra and actual concentrations. PCA is usually performed on centred spectra ($\mathbf{X_c} = \mathbf{X} - \mathbf{RowMean}(\mathbf{X})$). The decomposition leads to expressions relatively linked to $\mathbf{X_c}$. PCA is essentially performed as a singular value decomposition (SVD) used in various other mathematical approaches, as well.

SVD performs an orthogonal basis transformation of $\mathbf{X_c}$. The new basis is to maximise the variance covered by each axis. The transformation results in latent variables or loadings ($\mathbf{P}$) which can be interpreted as estimation of the pure component spectra and scores $\mathbf{T}$ which can be seen as estimation of the pure component concentrations:

$$\mathbf{X_c} = \mathbf{T} \times \mathbf{P} \tag{3.4}$$

$\mathbf{T}$ and $\mathbf{P}$ consist of an equivalent number of spectra (and scores) as $\mathbf{X_c}$. In addition to that, an SVD estimates singular values which indicate the variance covered by each score-loading-pair.

PCA heavily depends on the assumption that the spectra matrix is overdetermined (the chemical rank is lower than the numerical rank). Thus, relevant features are expected in the score-loading-pairs which cover much variance whereas the low variance score-loading-pairs consist of measurement noise. Additionally, an experienced spectroscopist can interpret spectral features in the structure of the loadings. For a more detailed mathematical background and examples the reader is referred to the tutorial on PCA by *Jonathon Shlens* [156].

The sorted structure of the loadings allows for feature selection based on the variance covered. Out of the scores and loadings an estimation of equation 3.3 can be made. The estimates for the concentrations $\mathbf{T}'$ and for the pure component spectral contributions $\mathbf{P}'$ are made by selecting the relevant scores and loadings and excluding the rest in an error term ($\mathbf{E}$):

$$\mathbf{X_c} = \mathbf{T}' \times \mathbf{P}' + \mathbf{E} \tag{3.5}$$

An MIR spectrum consists of hundreds to a few thousand data points. Hence, the decomposition decreases the number of parameters for regression by orders of magnitude comparing a PCR with multiple regression performed directly on the spectra. More information and mathematical background for PCR can be found in *Geladi et al.* [157].

3.4.2 Partial Least Squares (PLS) Regression

PCA projects $\mathbf{X_c}$ maximising total variance in the first principal components. The scores obtained by the projection can then be used for a regression to either classify or quantify. This approach however does not take into account any *a priori* knowledge present. Therefore, using a PCR model for classification purposes always implies the assumption that the main cause of variations in the data set are related to the modelling problem.

If *a priori* knowledge of the problem is present by having training data the concept of PCR can be modified to take this information into account. A Partial Least Squares (PLS) Regression does this by maximising the shared variance between measurement data and target variable (class for classification or concentration if used for quantification). This approach has proven to result in similar or better model quality than the unsupervised projection during PCR can provide [158].

PLS utilises the nonlinear iterative partial least squares (NIPALS) algorithm for projection. NIPALS in contrast to SVD, performs sequential extraction of score-loading-pairs. The extracted pair is linked to the variation in the target variable and the obtained loading is orthogonalised by introducing weights ($\mathbf{W}$). Each subsequent extraction is performed on the residuals of the last one. The full mathematical

explanation of the process can be found in an excellent tutorial by *Paul Geladi and Bruce Kowalski* [159].

The PLS approach as described above is only a projection which essentially resorts the variable space to accumulate the relevant information in fewer variables. In order to use this for classification or quantification it needs to be paired with a regression or classifier technique. For spectroscopic data the combination of PLS with a Linear Discriminant Analysis (LDA) has been demonstrated to provide a robust approach [160, 161].

3.4.3 Linear Discriminant Analysis (LDA)

Linear Discriminant Analysis (LDA) is a classifier based on a projection which maximises inter-group-variance while minimising intra-group-variance. For a classification into N different groups this is done by finding a $N-1$ dimensional subspace in the data set by applying a singular value decomposition on the covariance matrix of the classes similar to PCA. The mathematical details can be found in the original article by *R. A. Fisher* [162]. LDA applied to spectroscopic data on its own without regularisation however is prone to overfitting [163, 164]. Therefore it is often combined with either PCA or PLS as discussed above.

3.4.4 Implementations

The approach taken by a number of studies is to generate healthy/normal/benign vs disease type models using pixels of interest extracted from hyperspectral images. Selection of these regions of interest is either guided by a pathologist or extracted using a technique like k-means, or by a preliminary classification model trained to identify different tissue types (e.g. stroma), or a combination thereof. The predicted pathology labels can be generated on a per-pixel basis and refolded for visualisation in a similar approach described previously for k-means. Figure 3.1 shows an example human colon section where the red and green pixels are the outputs of a predictive algorithm to detect cancer. Black pixels have been rejected as "not-epithelium" and white pixels indicate the substrate, or absence of sample.

3.5 Chemometric Analysis of Discrete Frequency IR Images

Using FT-IR imaging is popular because use of the Fourier transform allows rapid collection of the entire spectrum. For biospectroscopy applications though there are regions of the spectrum that are not informative, either because they only contain noise or because they do not provide relevant information e.g. indicating the presence of disease. DF-IR has been proposed as an alternative that only collects IR images at specific ('discrete') wavelengths that are relevant to the problem being studied.

In general, the number of relevant wavelengths is expected to be far lower than those in a whole FTIR spectrum, and thus using DF-IR may speed up image acquisition, which is critical for translation of MIR imaging into histology applications. Because of the complexity of the samples in biospectroscopy, relevant targets for DF-IR imaging typically fall into bands, or blocks, covering regions of overlapping peaks that correspond to biologically important molecules such as proteins or lipids.

Thus, DF-IR imaging falls somewhere between multi- and hyper- spectral imaging. As such, many of the approaches described before, which work well for hyperspectral images, may no longer be suitable for DF-IR images. Alternative normalisation methods such as autoscaling (standardisation), or block scaling, will be more suitable due to the discrete nature of the wavelength regions being collected. Research is ongoing in this area as new instrumentation for collecting DF-IR images becomes available.

For DF-IR imaging to be successful, the right wavelengths have to be measured. The approach generally taken in the literature so far relies on FT-IR imaging combined with variable selection methods to identify the relevant wavelengths for a particular problem. A number of variable selection methods are available for this purpose, and some recent examples for wavenumber selection in DF-IR imaging include Gini coefficients [12] and Variable Importance in Projection (VIP) scores [165].

Whichever method is used, a robust validation scheme is required to prevent overfitting and accidental selection of non-informative wavelengths, both of which would be detrimental to translation of DF-IR into clinical applications. Ultimately, the selected wavenumber targets have to be tested using a large external validation set to verify their suitability for a given problem. The problem-specific nature of wavelength selection requires the selection to be applied afresh for every research question.

3.6 Applications

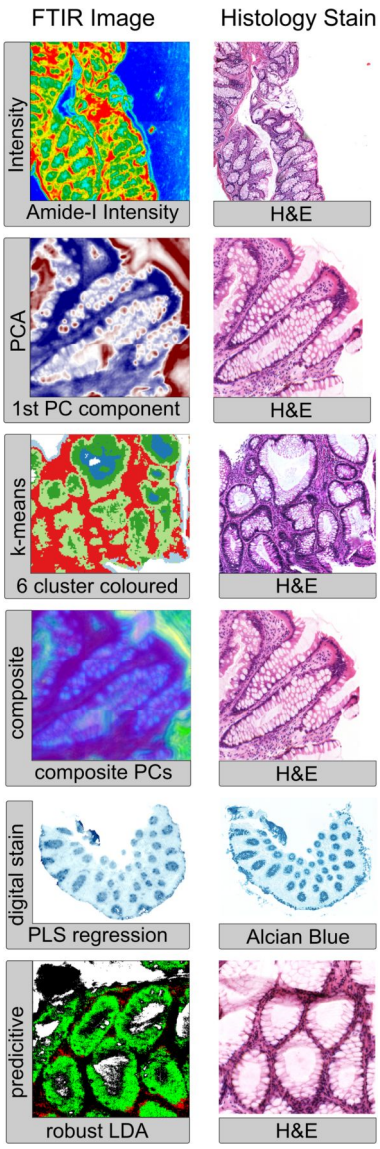

Figure 3.1: *Comparison of (left panel) different visualisation methods for hyperspectral imaging versus (right panel) a standard histology stain for columnar glands.*

MIR transmission profiles were first considered as valuable for diagnostic purposes in 1949 by Blout and Mellors [166] who obtained bulk spectra from tissue sections and blood smears. Since then research in this field did not really progress until the 1990s when FTIR microspectrometers became available [167]. Although tremendous progress in imaging technology has been made over the last decades [168], histopathological diagnostic routines have changed very little over the last hundred years [133, 169]. This could change soon with concepts of digital spectral pathology as pointed out in an excellent review by Bhargava and Madabhushi [170]. This section provides an overview of the current research on MIR imaging technology for biomedical diagnostics. Focus lies on imaging tissue sections and cells. Further interest is increasing in the analysis of biofluids, or liquid biopsies, which is outside the scope of this introduction, but the reader is directed to a review by *Baker et al.* [4] for more information on this.

As already discussed in the data processing section, IR hyperspectral images are directly correlated with the underlying biochemistry of the sample. Plotting metrics computed from IR spectra can be described as 'digital staining' i.e. an alternative to the chemical stains currently used in histopathology. Digital staining has the potential to provide more information than current chemical staining technologies. Increasingly complex information can be generated by treating three different intensity based images as a single RGB image. An example is shown in figure 3.1 which is the composite image of three selected principal components. One criticism of this approach is that the pseudo colour maps can be too colourful, which some pathologists may find off-putting. A suggested alternative is

to use approaches such as neural networks to generate images that look more like stained images and provide the equivalent of a chemically stained image without any chemical staining; so called stainless staining (124). An example using a PLS regression model to digitally stain a colon section is shown in figure 3.1. Advantages include visualising multiple stains for the same section and otherwise impossible stains e.g. for biomarkers or pathology indicators that do not currently have a chemical stain. The primary disadvantage is the decreased spatial resolution in IR images versus the visible, because of the longer wavelengths involved and the corresponding diffraction limit.

Digital staining, however, still relies upon a pathologist to interpret the resulting spatial distribution of biochemical signals as they would for conventional chemical staining, although each unstained section could be digitally stained for various different biomolecules of interest. The true benefit is gained by predicting pathology directly from the combined chemical and spatial information. *Old et al.* demonstrated classification accuracies of 100 % while denying decision for 30 % of the samples for the diagnosis of oesophageal adenocarcinoma [171]. *Tiwari et al.* described the use of a QCL microspectroscopy setup for the identification of infiltration and fibrosis in endomyocardial biopsy samples to assess transplant rejection, achieving 82.87 % overall accuracy without neglecting samples [104]. There are numerous more examples of proof of concept experiments achieving classification accuracies between 70 and 95 % [8, 12, 172–181].

The most common problem in this research however is that sample numbers are usually relatively small which makes classification models susceptible to the curse of dimensionality [170, 182]. If a single spectrum consists of more data points than there are samples, classifiers have significant chance of picking up random variations as features for classification. This can be overcome by applying dimensionality reduction methods such as PCA or increasing the sample size. Higher sample numbers however are difficult to collect, measure and analyse. A common shortcut, here, is to utilise tissue micro arrays (TMA) which are paraffin blocks consisting of selected biopsy sub-sections from different samples arranged in an array specifically used for medical research. Individual sections can then be taken that include cores of many tens to hundreds of tissues samples. This provides a good distribution of tissues, pathologies and patients, and it is simpler for the pathologist to classify each sample. The disadvantage of this is that it does not represent the large samples and variance found within individual samples that a pathologist would usually make their diagnosis from. A very good example of utilising TMAs for this purpose is given by Bhargava et

al. [183]. Another big challenge in the field is to find a uniform approach for data acquisition, to make use of the spectral information, suppressing perturbation from individual instrument response functions [184].

4 Oesophageal Cancers

4.1 Anatomy: The Physiological Oesophagus

The oesophagus is part of the gastrointestinal tract as depicted in Figure 4.1 [185]. Its primary function is to transport food from the mouth to the stomach for digestion. Its structural features can be classified in several different ways depending on the context. In this thesis a classification based on the microanatomy is most useful. Alternatively, it is also common to segment the oesophagus by its constrictions which is more convenient in a surgical context.

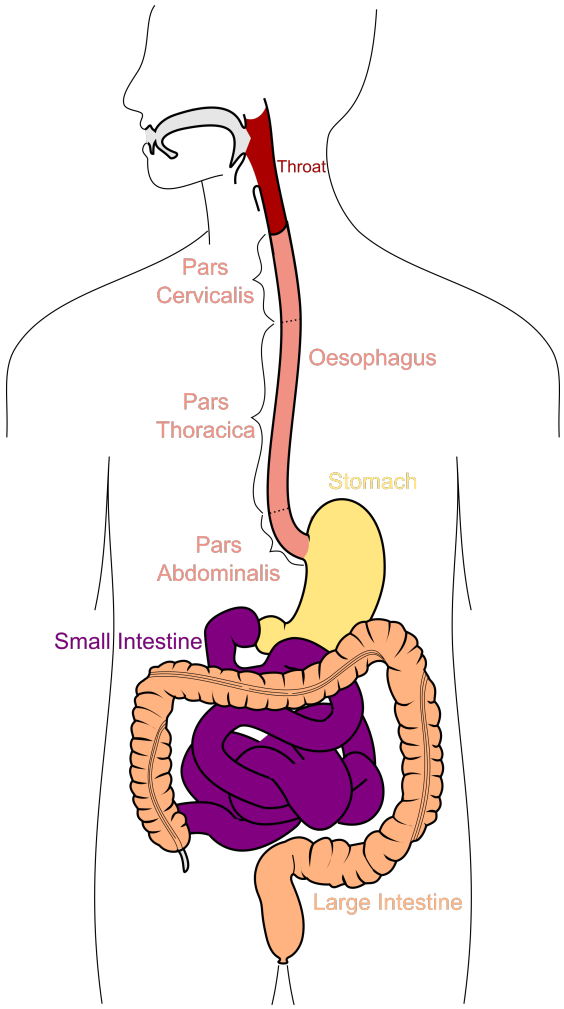

Figure 4.1: *The gastrointestinal tract [185].*

The five main structural features constituting the oesophagus (see Figure 4.2) from the inside to the outside are:

(1.) The Lumen which is the cavity food is transported through, facing (2.) the Mucosa, the innermost lining made of the mucous membrane. This layer of epithelium is followed by the Lamina Propria , a layer of connective tissue about a third of the thickness of the epithelium. It finishes with the Muscularis Mucosae, a slim layer of smooth muscle. (3.) The Submucosa is located on the outside of the Mucosa. The term describes a layer of dense connective tissue housing blood vessels, mucous glands and lymphatic tissue. It is followed by (4.) the Muscularis Propria, two orthogonal layers of muscle responsible

for the propulsive motion transporting food to the stomach. The outermost layer is the (5.) Adventitia, made of connective tissue [186].

For the purpose of this thesis it is important to see these structures in relation to their observability. At the current state of the art, infrared imaging techniques[1] can resolve tissue samples in the 1–10 µm regime. Individual biological cells as can be found in the oesophagus are on the same scale. Therefore, the cellular dimension of the different layers of the oesophagus needs to be discussed in more detail.

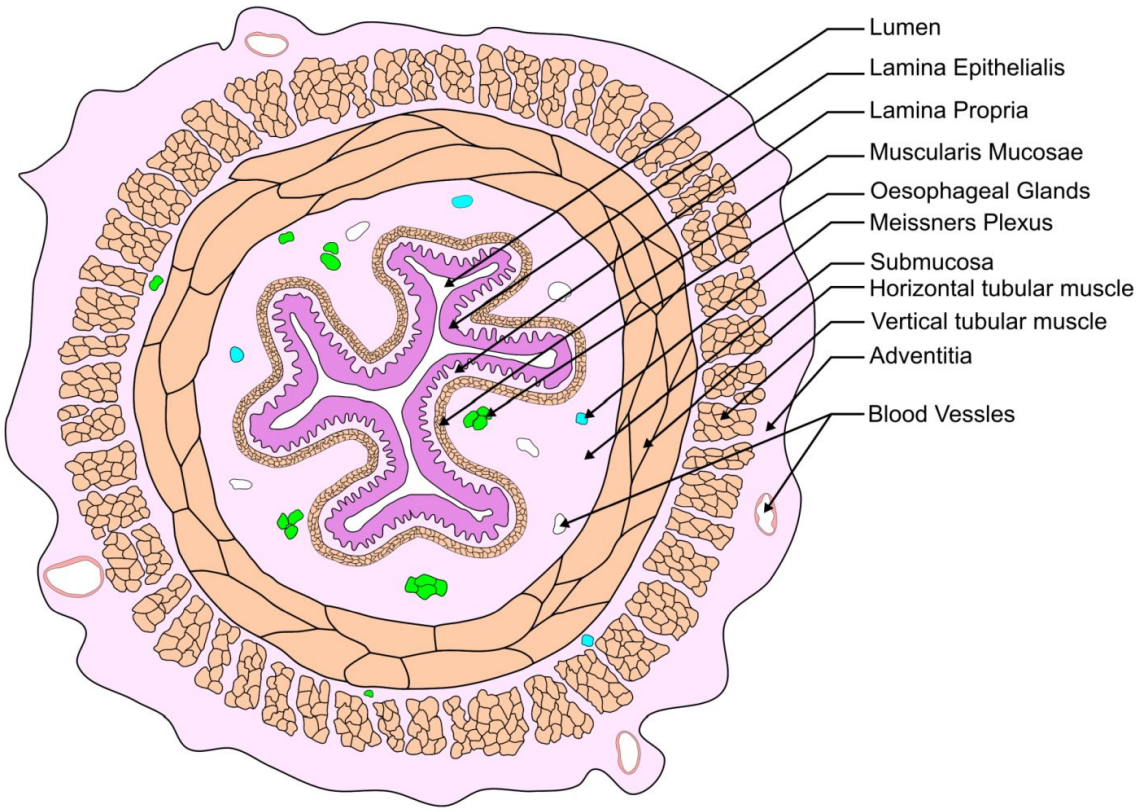

Figure 4.2: *Layers of the oesophagus.*

The Lumen essentially being a void, does not have any cellular features. There are stratified non-keratinizing squamous cells in the mucous membrane of the Mucosa. The lack of keratin however makes these cells less resistant to the mechanical strain than keratinized cells (e.g. skin). This leads to a high rate of cell loss by abrasion during the process of transporting food. To compensate for this, the epithelium is consistently regenerating itself from the basal to the superficial layers. In order to achieve consistent growth, the cells need to be connected to the nervous system

[1] Nano/nearfield imaging will not be discussed in this context as they are not capable to image large enough areas to be of histopathological relevance at this time.

and the blood supply. Cell division is most active in the basal layer of the mucous membrane facing the Lamina Propria. In this layer the cells are round and densely packed. Towards the Lumen they become flatter and level out.

The Lamina Propria is the structural interface connecting the Mucosa to the nervous system, the lymphatic system and the blood supply. It also houses the oesophageal cardiac glands and the ducts of the mucous glands which secrete mucus to lubricate the lining of oesophagus. Structurally the Lamina Propria consists mainly of loose connective tissue containing some lymphocytes, mostly helper T cells, plasma cells, and occasional eosinophils and mast cells. Large proportions however are extracellular matrix which consists mostly of collagen and other structural proteins like fibronectin.

The Muscularis Mucosae separates the Lamina Propria from the Submucosa. It is composed exclusively of smooth muscle cells. The muscle is in constant motion to ensure contact between the mucous membrane and the content of the Lumen during swallowing as well as supporting the secretion of the glands to keep the oesophageal lining lubricated.

The Submucosa is a layer of dense connective tissue adjacent to the Mucosa. It includes blood vessels, mucous glands and lymphatic tissue. It also houses Meissner‘s plexus, a collection of Dogiel cells which provides nerval innervation towards the Muscularis Mucosae and to the mucous membrane.

The Muscularis Propria consists of muscle cells oriented in a circular and a longitudinal coat. Controlled contraction of these muscles causes the propulsive motion transporting food to the stomach. Furthermore, the Muscularis Propria houses Auerbach‘s plexus, the biggest nervous node connecting the nervous system to provide motor and sensory innervation for the oesophagus.

The Adventitia is the outermost layer of the oesophagus and is built of coarse connective tissue. It creates the rigid structure of the oesophagus. The intestines, in contrast to the oesophagus, have a serosa which allows unhindered movement of the intestinal loops [186].

4.2 Pathology: The Diseased Oesophagus

There are several known risk factors for the development of oesophageal cancer. The two most common types of cancer are squamous cell carcinoma occurring in the upper oesophagus and adenocarcinoma occurring in the lower oesophagus.

Squamous cell carcinomas are strongly associated with smoking and consumption of alcohol or very hot beverages which is assumed to cause damage to the squamous cell‘s nuclei ultimately resulting in cancer. Furthermore, some genetic factors are known, as well [187]. This PhD thesis however focuses on the diagnosis of adenocarcinomas and their precursor stages. Oesophageal adenocarcinomas are mainly associated with gastric reflux.

Gastro-oesophageal reflux disease (GORD) is a common medical condition in western societies [188, 189]. It is associated with a complex set of risk factors including life style aspects like obesity [190] and smoking. Conditions like pregnancy or the need to take certain medication [191] are also considered as risk factors. Under adverse circumstances GORD can lead to an abnormal change of the oesophageal lining. Stratified squamous epithelium gets replaced by simple columnar epithelium with goblet cells which in non-pathological organisms is found in the stomach and intestines.

The change of cell functionality is referred to as metaplasia and was first observed in the oesophagus by N. R. Barrett in 1950 [192]. Therefore, it is often referred to as Barrett‘s oesophagus. The metaplasia itself is not harmful to the person developing it. The simple columnar epithelium is more resistant to chronic acid reflux from the stomach and has a protective function for the outer layers of the oesophagus in this case. Despite its acute protective function for the oesophagus the metaplasia is a precursor for adenocarcinomas. Patients diagnosed with Barret‘s oesophagus have a risk of 0.1 to 0.5 % per year to develop an adenocarcinoma [193], which is between 30 to 125 times higher than for the average member of the population [194].

There are also intermediate stages between a benign metaplasia and an adenocarcinoma, described as dysplasia. Dysplasia again can be subdivided in low and high grade [195]. Dysplastic cells carry damage beyond repair in their genome. This inhibits the tissue to revert into its original state once the external stress is relieved. Dysplastic cells are poorly differentiated and bear a high risk to progress into cancer. The grading of dysplasia however is highly subjective and varies substantially between national

guidelines [196]. Metaplastic cells in contrast to that are well differentiated and bear a lower risk for malignant transformation.

4.3 Diagnosis and Treatment of Oesophageal Cancers

4.3.1 Endoscopy

Diagnosing oesophageal cancers in clinical routine is mainly done via endoscopy. The endoscope used in this procedure consists of a long flexible tube which contains a camera to allow visual inspection as well as an instrument channel. The instrument channel can be used to insert a pincer tool with which tissue biopsies can be obtained for histological examination as depicted in Figure 4.3 (reproduced from [197] with permission of the rights holder, Elsevier.).

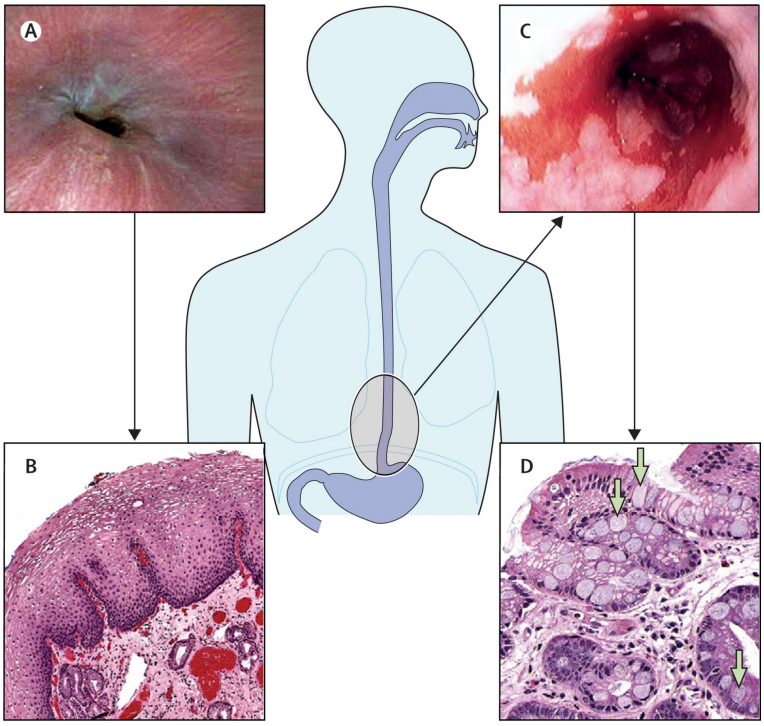

Figure 4.3: *Normal oesophagus versus Barrett's oesophagus. (A) Normal appearance of squamocolumnar junction at gastro-oesophageal junction. (B) Normal oesophageal squamous mucosa. (C) Tongues of Barrett's oesophagus radiating orad from the gastro- oesophageal junction. (D) Biopsy specimen of intestinal metaplasia (arrow points to goblet cell). Reproduced from [197] with permission of the rights holder, Elsevier.*

The visual differences observable through the white-light channel of the endoscope between normal (Figure 4.3 A) and Barrett's (Figure 4.3 B) can be much more

subtle than in the depicted example. Therefore, surgeons need years of training and experience to spot anomalies in a very subjective fashion. If the examiner suspects Barrett's, the guidelines recommend taking at least 8 biopsies [198] to investigate via histology.

4.3.2 Histology

In the histology laboratory the biopsies are fixed with 3.7 % formalin to prevent enzymes breaking the tissue down. Then the tissue is washed in solutions of ethanol and water with a gradient increasing from 70 % ethanol to pure ethanol to dry the sample. Afterwards, the ethanol is replaced by a solvent (e.g. xylene) miscible with ethanol and paraffin for optical clearing. Then the tissue is transferred into molten paraffin at a temperature of 52–60 °C. The solvent evaporates and the voids fill with paraffin which stabilises the tissue for cutting with a microtome once the paraffin block containing the tissue is cooled to room temperature. The microtome produces sections of a thickness of 2–20 µm. The sections are floated onto a water bed and transferred to a histology slide.

As the fixation procedure and chemical treatment deactivates most enzymes and alters the structure of many proteins, an alternative to this workflow is cryo sectioning if the biochemistry of the sample is of interest. In that procedure the tissue is snap frozen and sectioned at -21 °C [199]. Fresh frozen sections can be obtained within minutes after collection of the biopsies whereas formalin fixed paraffin embedded (FFPE) sections need several hours to be processed. FFPE tissue blocks however are storable in tissue archives and their sections preserve the morphology of the tissue better than fresh frozen sections.

The sections of tissue obtained from the microtome or cryotome need to be stained in order to be assessed by the pathologist. In the majority of cases haematoxylin and eosin (H&E) staining is performed. Haematoxylin stains acidic structures like DNA in the cell nucleus blue or purple. Eosin provides contrast to cytoplasmic components staining them pink (see figure 4.3 C&D).

The pathologist is assessing the H&E stains according to the 'Vienna classification of gastrointestinal epithelial neoplasia' (see Table 4.1 and indented citation) as reproduced with permission from the rights holder, Elsevier from [196])

Table 4.1: *Vienna classification of gastrointestinal epithelial neoplasia, reproduced with permission from the rights holder, Elsevier from [196]*

Category 1	Negative for neoplasia/dysplasia
Category 2	Indefinite for neoplasia/dysplasia
Category 3	Non-invasive low grade neoplasia (low grade adenoma/dysplasia)
Category 4	Non-invasive high grade neoplasia 4.1 High grade adenoma/dysplasia 4.2 Non-invasive carcinoma (carcinoma in situ) 1-150 4.3 Suspicion of invasive carcinoma
Category 5	Invasive neoplasia 5.1 Intramucosal carcinoma 1-151 5.2 Submucosal carcinoma or beyond

For biopsies diagnosed as category 1-negative for neoplasia/dysplasia (including normal, reactive, regenerative, hyperplastic, atrophic, and metaplastic epithelium)-further follow up of the lesion may or may not be necessary, as clinically indicated. In the case of category 2-indefinite for neoplasia/dysplasia-follow up is needed because of uncertainty about the real nature of the lesion. In category 3-non-invasive low grade neoplasia (low grade adenoma/dysplasia)-neoplasia is present but the risk of developing invasive carcinoma is low. Clinicians may consider local treatment of the lesion or opt for follow up. In category 4-non-invasive high grade neoplasia-the risk of invasion and development of metastases is increased. Local treatment such as endoscopic mucosal resection or local surgical treatment would be indicated. In the case of category 5-invasive neoplasia-the risk of subsequent deeper invasion and metastases is so high that treatment is urgently needed and should only be withheld in cases with clinical contraindications. In general, before a decision on treatment is made, one should always take into account the possibility of sampling error which may lead to underestimation of the grade of neoplastic change or depth of invasion. The histological diagnosis of biopsy specimens is only part of the total clinical information and should be supplemented by available endoscopic, radiological, and ultrasonographic assessments of the depth of invasion.

The following medical treatment of the patient depends on the grading by the pathologist. If metaplasia is detected, no immediate action is required. The patient is advised to stay under surveillance [200]. In some cases, medication with proton pump

inhibitors is administered to stop or delay progression to dysplasia [201]. If dysplasia is detected by the pathologist, resection, endoscopic radioablation or argon plasma coagulation is recommended to destroy the dysplastic cells [202, 203]. A major problem in the field, however, is that grading is still quite variable between observers [10].

A large proportion of adenocarcinoma cases do not need sophisticated diagnostic routines because patients often already present with symptoms like dysphagia caused by tumorous stenosis of the lumen when they first contact a physician. In that case the tumour can be diagnosed endoscopically or using X-ray imaging with barium sulphate as contrast agent. A resection of the oesophagus is necessary and patient survival rates are very low because of the advanced stage of disease [204]. Therefore, more sensitive tools are needed to aid diagnosis and detect these carcinomas earlier.

An excellent overview over the current state of the art and clinical procedure can be found in the review of *Saheen et al.* [198].

4.4 Epidemiology

About 10 % of the western world‘s population suffer from some form of oesophageal disease [188, 189, 205, 206]. The incidence of oesophageal cancer is rapidly increasing [207, 208]. It is currently the seventh leading cause of cancer deaths in the world [209]. Worldwide, squamous cell carcinoma represents 90 % of the total cases, but the subpopulation of the western world does have a much higher incident rate of adenocarcinoma compared to squamous cell carcinoma.

On a global scale, the incident rate of adenocarcinoma per 100.000 person-years is only 0.7. The western world however has a significantly higher incident rate, with the UK in particular having an incident rate of 7.2 in men and 2.5 in women. Oesophageal adenocarcinomas are particularly dangerous as only 20 % of patients survive for 5 years or longer [207]. The main reason for these poor survival rates is the fact that symptoms only occur once the cancer has progressed substantially. Therefore, most patients present at a stage where the cancer is already incurable [204]. It is estimated that only 7 % of cases in the USA are diagnosed through the current cancer control approaches and therefore more effective screening is needed [210].

4.5 New Technologies for Diagnosis of Oesophageal Cancers

The main focus in developing new approaches lies on providing tools for early detection. White-light endoscopy is not sensitive enough to reliably differentiate between Barrett's with dysplasia and Barrett's without dysplasia which leads to the necessity of taking biopsies every 2 cm. In addion to being labour intensive and severely inconvenient for the patient, this protocol is also inefficient. Only less than 5 % of the oesophageal lining is sampled which causes up to 57 % of dysplasia remaining undetected [211, 212].

4.5.1 Endoscopy

Combining traditional white light endoscopy with confocal laser endomicroscopy (CLE) has been demonstrated to double the sensitivity to detect dysplasia from 34.2 to 68.5 % [213]. It can however not be used as a standalone technique as it provides a high false-positive rate of 7.3 % without combination with white light endoscopy [214]. Furthermore, both of these techniques only function as red-flagging methods to guide biopsies and will not make physical removal of tissue obsolete.

4.5.2 Cytology

A method which does not necessarily require macroscopic removal of tissue is cytology. *Fitzgerald et al.* [215] identified Trefoil factor 3 (TFF3) a mucin-associated peptide involved in multiple biological functions like repair of the mucosa and modulation of stem cell differentiation can serve as a biomarker to detect Barrett's. An immunohistological stain has been developed to stain against TFF3 and identify goblet cells characteristic for Barrett's. This can be used in combination with a cell harvesting device referred to as Cytosponge.

The device consists of a compressed sponge on a string encapsulated in a gelatine coating. The gelatine dissolves after swallowing which causes the sponge to unfold. After unfolding the sponge is withdrawn, collecting cells on its way up the oesophageal lining. The harvested cells are then stained and scored by a gastrointestinal histocytopathologist in a binary fashion as either positive ($\geq$1 TFF3-positive goblet cell) or negative. This procedure achieved sensitivity of 80 to 90 % in a first clinical trial [216].

The Cytosponge-TFF3 test is therefore currently tested in a larger trial to evaluate its feasibility for routine use [217].

Cytological methods in general, however, have the disadvantage that they do not provide localisation information. Therefore, additional tools are required once dysplasia or adenocarcinoma are diagnosed to localise them.

4.5.3 Spectral Cytopathology

Diem et al. [218] first demonstrated the use of MIR spectroscopic methods to investigate cytology samples of the oral cavity and reported promising sensitivities and specificities of >90 %. This study however consists of only 26 patients which include only 4 tumour patients and therefore has very little clinical value. *Diem et al.* followed up with a second study [219] on Barrett's oesophagus cytological samples but again with a very small set of only 10 patients. *Old et al.* [220] demonstrated a similar spectral cytology procedure using MIR spectroscopy on a larger set of 66 patients. The study reported sensitivity and specificity respectively as follows: normal squamous cells 79.0 % and 81.1 %, nondysplastic Barrett's oesophagus cells 31.3 % and 100 %, and neoplastic Barrett's oesophagus cells 83.3 % and 62.7 %. The very low sensitivity for nondysplastic Barrett's, however, deems this approach unsuitably for screening purposes.

4.5.4 MIR Spectroscopy and Imaging

A small number of studies suggest vibrational spectroscopy could be used on bulk tissue or histological sections to tackle the issue of relatively high inter-observer variability. Comparing the results of three different pathologists, a study showed only moderate agreement between their diagnoses [10]. MIR imaging could be used to reduce this variability.

The first study to investigate the potential was performed by *Wang et al.* in 2007 utilising ATR-FTIR spectroscopy to discriminate and classify normal squamous, Barrett's, dysplastic and gastric mucosa in fresh-frozen sections [221]. The study sampled 32 patients and detected dysplasia with 92 % sensitivity, 80 % specificity, and total accuracy of 89 %. Improving inter-observer agreement between two gastrointestinal pathologists for dysplasia to $\kappa = 0.72$ versus $\kappa = 0.52$ for histology alone.

In 2009, *Quaroni et al.* demonstrated the characterisation of normal squamous, Barrett's, and adenocarcinoma tissue samples using FT-IR imaging in FFPE tissue [222]. The study links Barrett's to an accumulation of glycoproteins and significant decrease in glycogen accumulation in the surface layer of the oesophageal lining and suggests this could be harnessed for diagnostic purpose. This correlation has yet to be proven however.

In 2012, *Amrania et al.* demonstrated the use of an MIR imaging system to obtain digital staining information for diagnostic purposes [223].The study uses an instrument with filters to collect images at discrete MIR wavelength. The author of this thesis however cannot see any added value in the results of the experiment compared to a normal white light microscope. The spatial resolution is worse than standard white light microscopes and the image contrast obtained is not adding value either.

The most recent study to the authors knowledge by *Old et al.* developed a machine learning algorithm to differentiate between normal squamous, Barrett's, dysplasia and adenocarcinoma based on FT-IR imaging data from fresh frozen tissue sections [171]. The study evaluates samples of 22 patients demonstrating 100 % sensitivity and 100 % specificity in discriminating between benign and abnormal types. Neoplastic Barrett's (dysplasia or adenocarcinoma) was identified with 95.6 % sensitivity and 86.4 % specificity.

Furthermore, the start-up 'beamline diagnostics' is developing an FT-IR spectrometer workflow similar to the method developed by *Wang et al.* (discussed above) for diagnosis of oesophageal cancers (http://www.beamlinediagnostics.com/).

4.5.5 Raman Spectroscopy and Imaging

In contrast to MIR spectroscopy which is not applicable in samples with high water content Raman spectroscopy can be used to analyse clinical samples in vivo. A detailed comparison between MIR and Raman and assessment of the current state of the art can be found in a review by *Baker et al.* [224].

Kendall et al. [10] first demonstrated the use of Raman spectroscopy to differentiate between normal tissue, Barret's and neoplasia in a set of 44 patients. The study reports sensitivity and specificity for normal 97 % / 99 %; Barrett's 84 % / 98 % and neoplasia 94 / 93 %. Raman microspectroscopic techniques are however very slow

compared to MIR imaging systems and deliver comparable contrast but slightly higher spatial resolution.

The author sees main potential for Raman spectroscopic techniques in their application in endoscopic probes. *Ishigaki et al.* [225] demonstrated the use of a portable Raman system to investigate fresh ex vivo samples. They demonstrated sensitivity and specificity of 81.0 % and 94.0 % for the discrimination of normal from cancerous tissue in a set of 92 patients.

Bergholt et al. [226] developed a custom-built probe for in vivo Raman spectroscopic detection of Barrett's associated dysplasia in real-time. The probe was engineered to fit a standard endoscopic biopsy channel. By measuring Raman spectra from surface lesions before obtaining biopsies they demonstrated sensitivity and specificity of 87 % and 84.7 %, respectively, for identification of high-grade dysplasia.

As Raman spectroscopy in general suffers from weak signal, several strategies exist to boost the signal. *Feng et al.* [227] demonstrated the use of silver nanoparticles as contrast agent boosting the Raman signal via surface plasmon enhancement. They investigated paired sections of normal and abnormal tissue of 44 patients. Microdroplets of silver nanoparticles were added to the sections before measuring them. This approach achieved an enhancement of the Raman signal demonstrating differentiation of oesophageal cancer tissue from normal control tissue with 90 % sensitivity and 97 % specificity.

Another way to amplify the Raman signal is to harness non-linear phenomena like stimulated Raman scattering (SRS) or coherent anti-Stokes Raman scattering (CARS), in combination often referred to as coherent Raman scattering (CRS). An overview of these techniques can be found in a review paper by *Schie et al.* [228]. Although the author is not aware of any work with oesophageal samples, one application of CRS is particularly relevant in this context. *Ji et al.* [229] demonstrated the use of SRS microscopy to rapidly acquire in situ label-free pseudo H&E images. Ratio images of Raman signals at 2930 and 2845 cm^{-1}, reflecting the different lipid and protein contents, provide contrast to compute images similar to H&E staining.

4.5.6 Digital Pathology

Another emerging trend to improve histological routines is 'Digital Pathology' [170] which has been demonstrated by *Critchley-Thorne et al.* in 2015. The team detected

statistically significant differences between Barret's oesophagus biopsies with high grade dysplasia and nondysplastic biopsies using machine learning algorithms on H&E images [230].

5 Characterisation of MIR Imaging Systems

5.1 Introduction

Benchmarking imaging systems was first done in a standardised fashion by the United States Air Force (USAF) in 1951 who developed a standard protocol (MIL-STD-150A). This procedure was originally developed to test cameras for photography but has been adapted for the use with microscopy systems. Although the standard is outdated for photography and was replaced by ISO12233:2017 [231], the USAF chart developed in 1951 (see figure 5.1) is still widely used in microscopy.

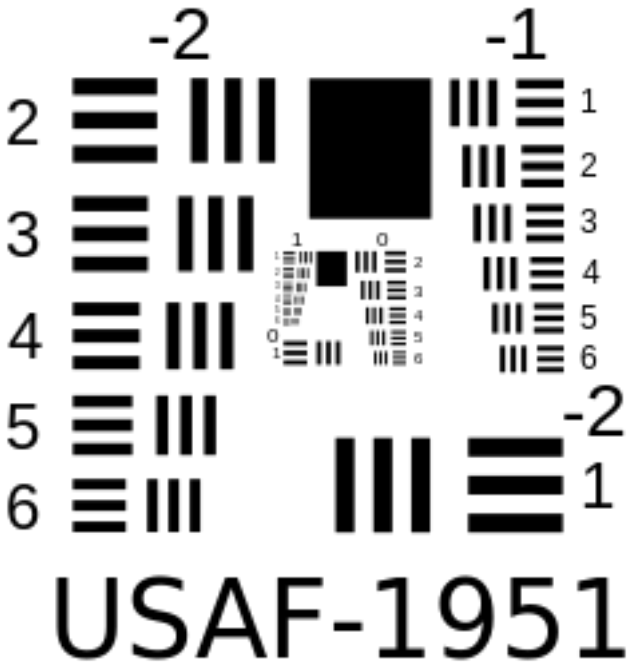

Figure 5.1: *Original 1951 US air force standard resolving power test target. Reproduced from [232].*

The original target consists of 9 groups, with each group containing 6 elements; thus there are 54 target elements provided in the full series. Each element consists of three parallel bars. These 54 elements are provided in a standardised series of logarithmic

steps in the spatial frequency range from 0.250 to 912.3 line pairs per millimeter. The series of elements spans the range of resolution of the unaided eye, down to the diffraction limits of conventional light microscopy. Commercially available targets usually are printed as metallic chromium on a 50 mm × 50 mm glass slide.

The spatial resolution of an imaging system can be obtained by evaluating the image of the slide. The spatial resolution defined by the Rayleigh criterion [233] requires a contrast between a feature and the background of at least 25 %. The size of the smallest feature which fulfils this requirement can be taken as a measurement of the spatial resolution of the system. This approach is demonstrated in the following. The next paragraph is work of the author and was reproduced with permission of the rights holder, Elsevier from *Nallala et al.* [234]. It demonstrates the use of a commercially purchased USAF target to characterise a 25 × magnification Cassegrain objective used on an Agilent Cary 620 MIR microscope:

In order to measure the highest resolution of the system, rather than the pixel size, the elements 4, 5 and 6 of group 7 on the USAF target were measured using the objective with the highest numerical apperture (NA) at the highest magnification (0.81 NA and final magnification of 63 ×). The lines of this group are separated by 2.76, 2.46 and 2.19 µm respectively. Figure 5.2 shows the images obtained by visualising the average intensity per pixel of a low wavenumber region (figure 5.2A, 1400–1000 cm^{-1}) and a higher wavenumber region (figure 5.2B, 3900–3800 cm^{-1}). Figure 5.2C shows a close-up of the smallest structures (from figure 5.2B) of the USAF target for the region 3900–3800 $cm^{-1}$and below it the corresponding intensity profile along the coloured cross sections. The differences in intensity along the cross section show that all of the structures of the target are clearly resolvable in the high wavenumber region. The Rayleigh criterion for optical resolution requires a difference in detected intensity of at least 25% to consider two points being separated is clearly fulfilled for all structures here [233].

However, this only gives discrete resolution for specific wavelengths and estimating the resolution of an image when using multivariate analysis of an entire spectrum is still a subject of ongoing research. The USAF target features of element 6 of group 7 2.19 µm where resolved with a pixel size of 0.66 × 0.66 µm. Further, pixels were binned to explore how reduction in the sampling frequency affects the resolution of the USAF target features. For this, pixels from figure 5.2C were binned two times (figure 5.2D) and four times (figure 5.2E) and their respective intensity profiles plotted (corresponding plots below figure 5.2D and E, respectively). The USAF target features

were still resolvable (following the Rayleigh criterion) for figure 5.2D , while the structures become no more resolvable as can be observed by the loss of the intensity plot in figure 5.2E.

Overall, the plot shows a decreasing intensity profile for resolving the USAF target features as the sampling frequency decreases. It has to be noted that the difference in spatial resolution between the vertical and horizontal axis especially in figure 5.2C, is an inherent effect caused by the sampling geometry. In transflection mode, only half of the objective is illuminated by the source whereas the other half of it is used to collect the transflected light. This effectively results in a lower opening angle along one of the axis and therefore decreases spatial resolution along that axis.

5.2 Design of a New Microscopy Test Target

The main reason for the USAF target still being used in microscopy, despite being outdated elsewhere, is that it is easier to manufacture on micro scale and validate. The modern benchmark targets for photography usually involve patterns with contrast gradients which can not be manufactured with lithographic methods to this date. Commercially available chrome on glass targets however do have some limitations and do not represent a common scenario for bioimaging.

First of all, glass is poorly transmissive in the MIR and therefore prohibits the use of transmission imaging, which is most often used to image biological materials. Secondly, chrome is also not an ideal material for spectral imaging in the MIR. It has in general a very low transmissivity and does not show sharp characteristic features. Thirdly, the pattern itself can be improved, as the original 1951 USAF pattern is already outdated for use in photography and was replaced by ISO12233.

These boundary conditions led to designing a new resolution test chart. In order to be able to use transmission MIR imaging, CaF_2 is used as a substrate material instead of glass. A material with characteristics more suitable to make the features (instead of metallic chromium) is Polymethylmethacrylate (PMMA). PMMA has a decent transmittivity and characteristic spectral features. PMMA can be spin coated onto CaF_2 easily. Furthermore, it can be manipulated by electron beam lithography to obtain detectable features. However, the pattern used for ISO12233 is too sophisticated to be manufactured by electron beam lithography. Therefore, it was decided to go back to the original 1951 USAF pattern and adjust it for the purpose at hand.

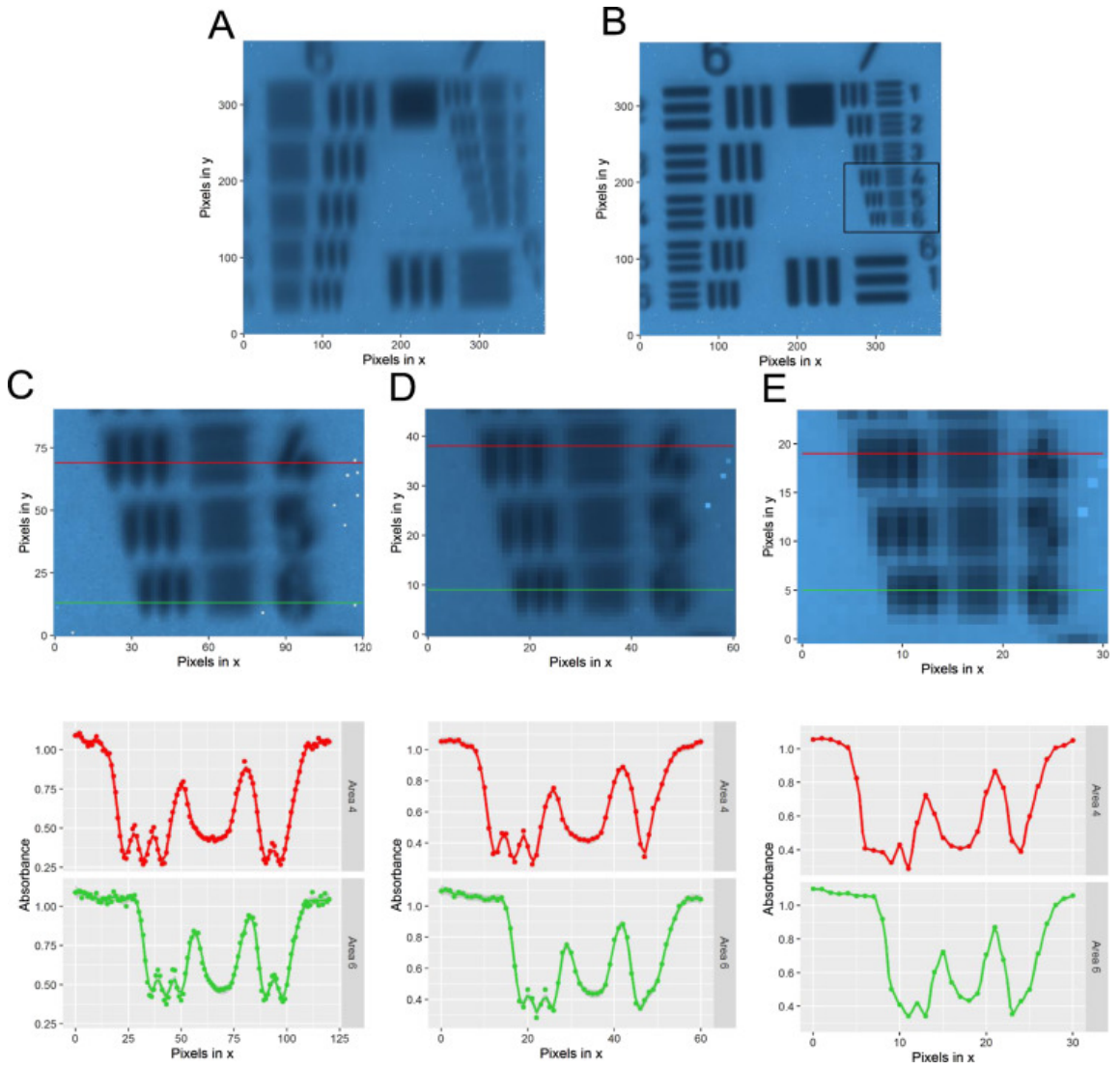

Figure 5.2: *FTIR image of chrome on glass USAF 1951 target of the elements 4, 5 and 6 of group 7 measured using 0.81 NA infrared objective at 63× magnification corresponding to a pixel size of* $0.66\,\mu m \times 0.66\,\mu m$. *(A) Average intensity per pixel in the region 1400–1000* cm^{-1}*; (B) average intensity per pixel in the region 3900–3800* cm^{-1}*;(C) zoomed in area of the boxed region from B with its corresponding average intensity along the coloured lines; (D)* 2×2 *binned image of C with its corresponding average intensity along the coloured lines; (E)* 4×4 *binned image of C with its corresponding average intensity along the coloured lines. Reproduced from Nallala et al. [234].*

As the original definition in MIL-STD-150A itself is not publicly accessible, the thesis relies on a secondary citation of it given by *Earl F. Glyn* [235] (see figure 5.3).

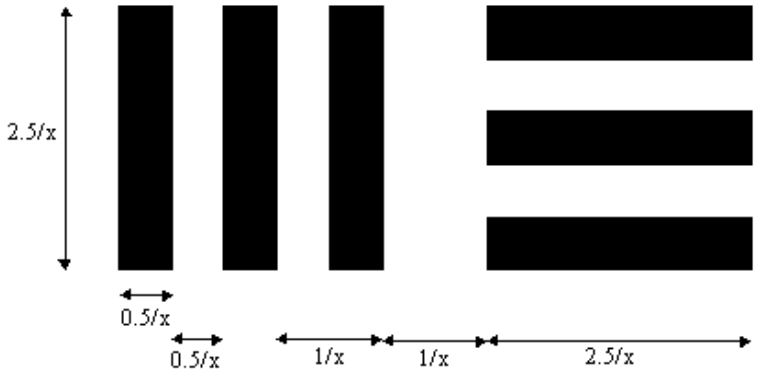

Figure 5.3: *Definition of the original 1951 US air force standard resolving power test target element. Reproduced from Glyn et al. [235]: From MIL-STD-150A: "The patterns of lines are parallel lines 2.5/x millimeters long and 0.5/x millimeters wide with space 0.5/x millimeters wide between the parallel lines, where x equals the number of lines per millimeter."*

Since the distance between two elements($D(E_i, E_{i+1})$) in one group is not further specified in the citation it was defined to $D(E_i, E_{i+1}) = 4x_i$ to have sufficient spacing.

In order to be able to study Mie scattering related effects using the target the USAF pattern is extended by circular features. The target consists of elements (see figure 5.4) which are made up by features. An element consists of a 3 × 3 array of circles, a set of 3 vertical lines and 3 horizontal lines. The size (x) of a feature (in mm) is given by equation 5.1:

$$x = \frac{0.5}{2^{Group+1+(Element-1)/6}} \tag{5.1}$$

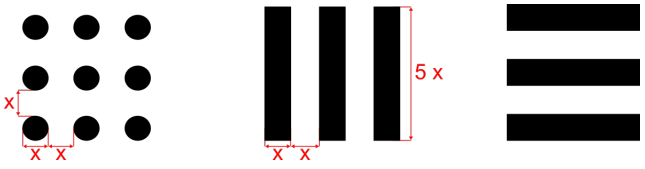

Figure 5.4: *New resolving power test target element and relationship of feature sizes (x)*

Six elements in different sizes make a group and two groups make a layer. A rectangle of the size of the next smaller layer is added to each layer as well for calibration

purposes. The target designed here covers the groups 4 to 9 with feature sizes ranging from 32 µm to 0.55 µm , as displayed in table 5.1.

Table 5.1: *Feature sizes for new resolution test chart.*

	Group Number					
Element	**4**	**5**	**6**	**7**	**8**	**9**
1	31.25	15.63	7.81	3.91	1.95	0.98
2	27.84	13.92	6.96	3.48	1.74	0.87
3	24.80	12.40	6.20	3.10	1.55	0.78
4	22.10	11.05	5.52	2.76	1.38	0.69
5	19.69	9.84	4.92	2.46	1.23	0.62
6	17.54	8.77	4.38	2.19	1.10	0.55

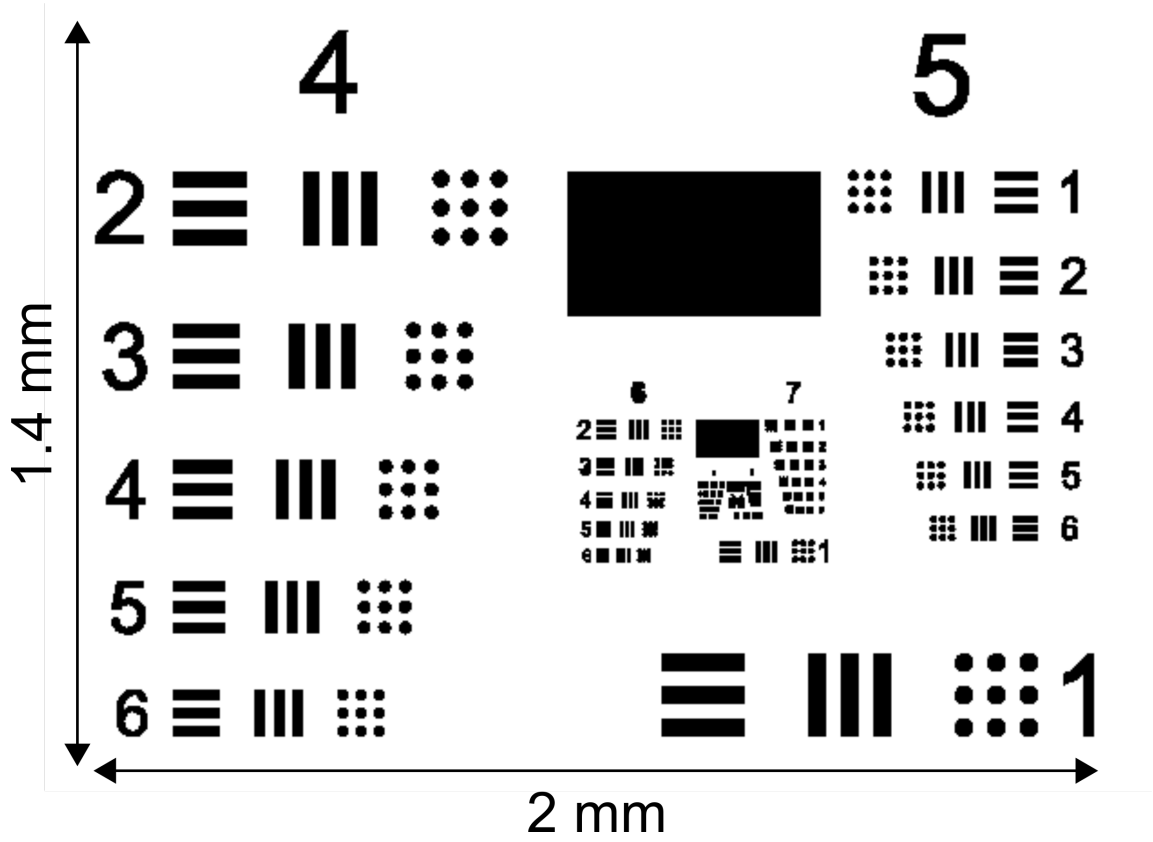

Figure 5.5: *New resolution test target.*

5.3 Manufacturing of New Target

The targets are manufactured by standard clean room procedures. First, approximately 1 ml of PMMA 950K A11 (Microchem; dissolved in Anisole), is pipetted onto a 1 cm×1 cm CaF_2 chip (Crystan; 0.5 mm thickness) and spun in a spin coater at 4000 rotations per minute for 3 minutes. After spinning, the chip is placed on a hot plate at 180 °C for 2 minutes. This procedure evaporates the solvent and cross links the PMMA and results in a layer of approximately 2 µm thickness.

Afterwards, an additional aluminium layer of approximately 15 nm thickness is evaporated onto the PMMA to provide conductivity for electron beam lithography. Then the pattern is written by electron beam lithography. After lithography the aluminium is removed with microposit MF-319 developer (Microchem). The written features are then developed by bathing the substrate in a developer solution consisting of 15:5:1 Isopropylacohol:Methyl-isobutyl-ketone:Methyl-isopropyl-ketone for 60 s. The developer dissolves the areas exposed to the electron beam and leaves the cross linked areas intact.

The procedure can be adapted to also produce features made of gold in order to obtain a high contrast, as gold is reflective in the MIR. To make gold targets, the negative of the pattern needs to be written with electron beam lithography. Following the development, gold can be evaporated onto the substrate. Afterwards, the substrate is put into acetone which dissolves the cross linked PMMA and leaves behind the features as metallic gold. As the last step the chip is mounted in a custom 3d-printed holder of standard microscopy slide size (see figure 5.6).

Figure 5.6: *Photograph of new resolution test target.*

5.4 Characterisation of New Targets

5.4.1 White-light Microscopy

The manufactured targets were characterised using a Zeiss Axio Scan Microscope. The target manufactured with features made of deposited gold is displayed in figure 5.7. The manufacturing worked down to group 9 or 10 which is already outside of the resolution of the white light microscope used for characterisation. Using the target, the microscope's spatial resolution can be estimated to be between 690 and 780 nm, as feature 3 of group 9 is still resolved but feature 4 is not.

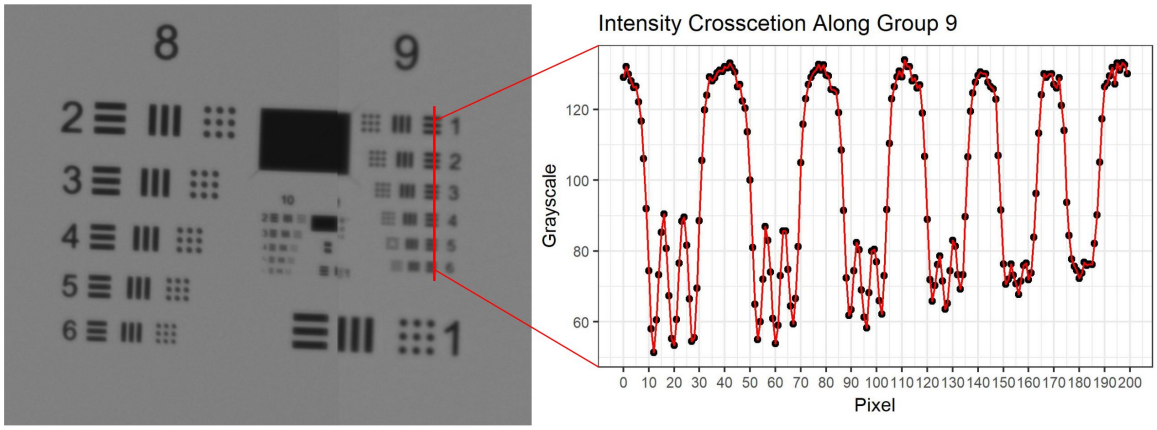

Figure 5.7: *Microscope image of manufactured resolution test chart made of 30 nm gold on CaF_2 with intensity profile.*

Figure 5.8 shows a target made of PMMA on CaF_2. Manufacturing the features in PMMA proves to be difficult as the adhesion of the PMMA to the CaF_2 is rather poor for the small features.

Writing the pattern as a negative works better, as depicted in figure 5.9. The PMMA does however show cracks.

5.4.2 FTIR Imaging

In order to investigate the usability the new targets have also been imaged on an Agilent Cary FTIR system (Agilent 670 FTIR spectrometer coupled with an Agilent 620 FTIR microscope). The system consists of a Globar source, and a liquid nitrogen cooled 128×128 pixels focal plane array (FPA) mercury cadmium telluride detector. A Cassegrain IR objective with numerical aperture (NA) of 0.62 and 15×

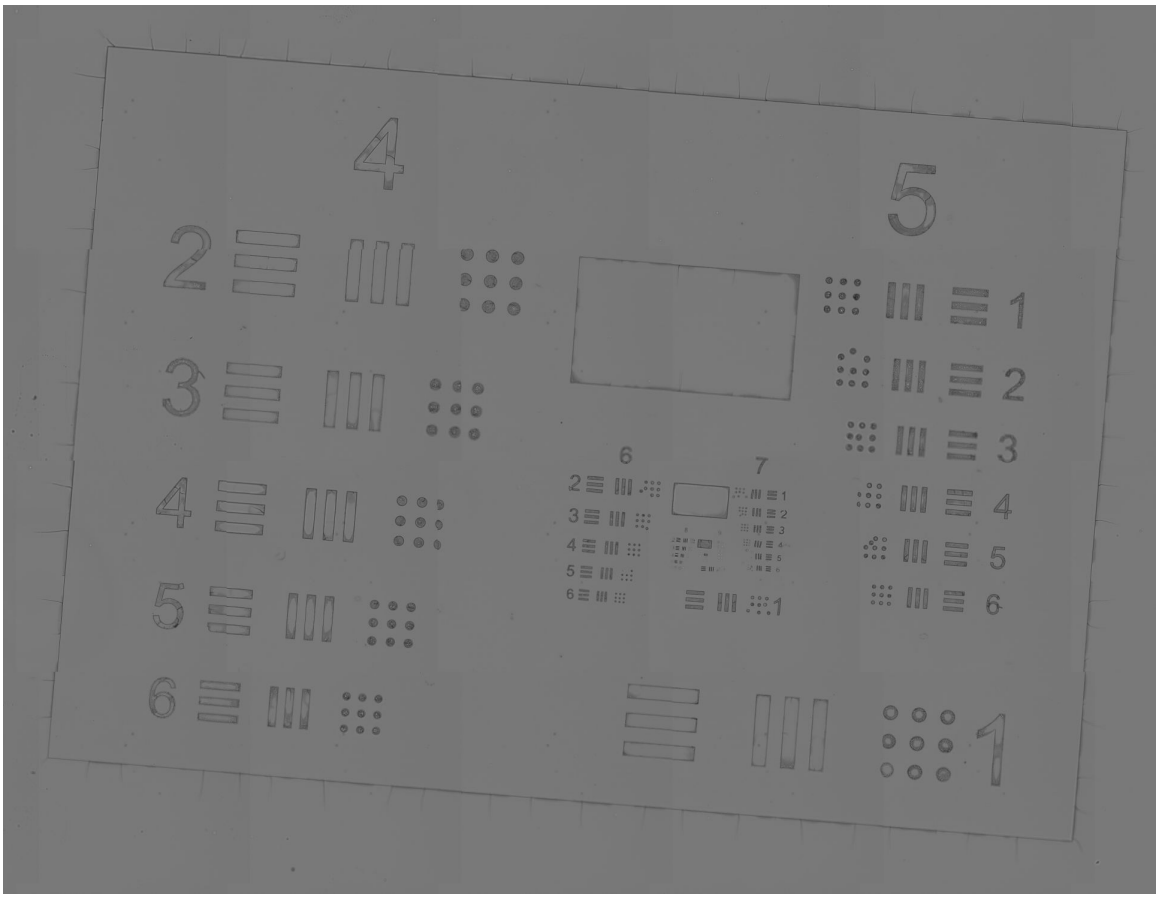

Figure 5.8: *Microscope image of manufactured resolution test chart 2.5* µm *PMMA on* CaF_2.

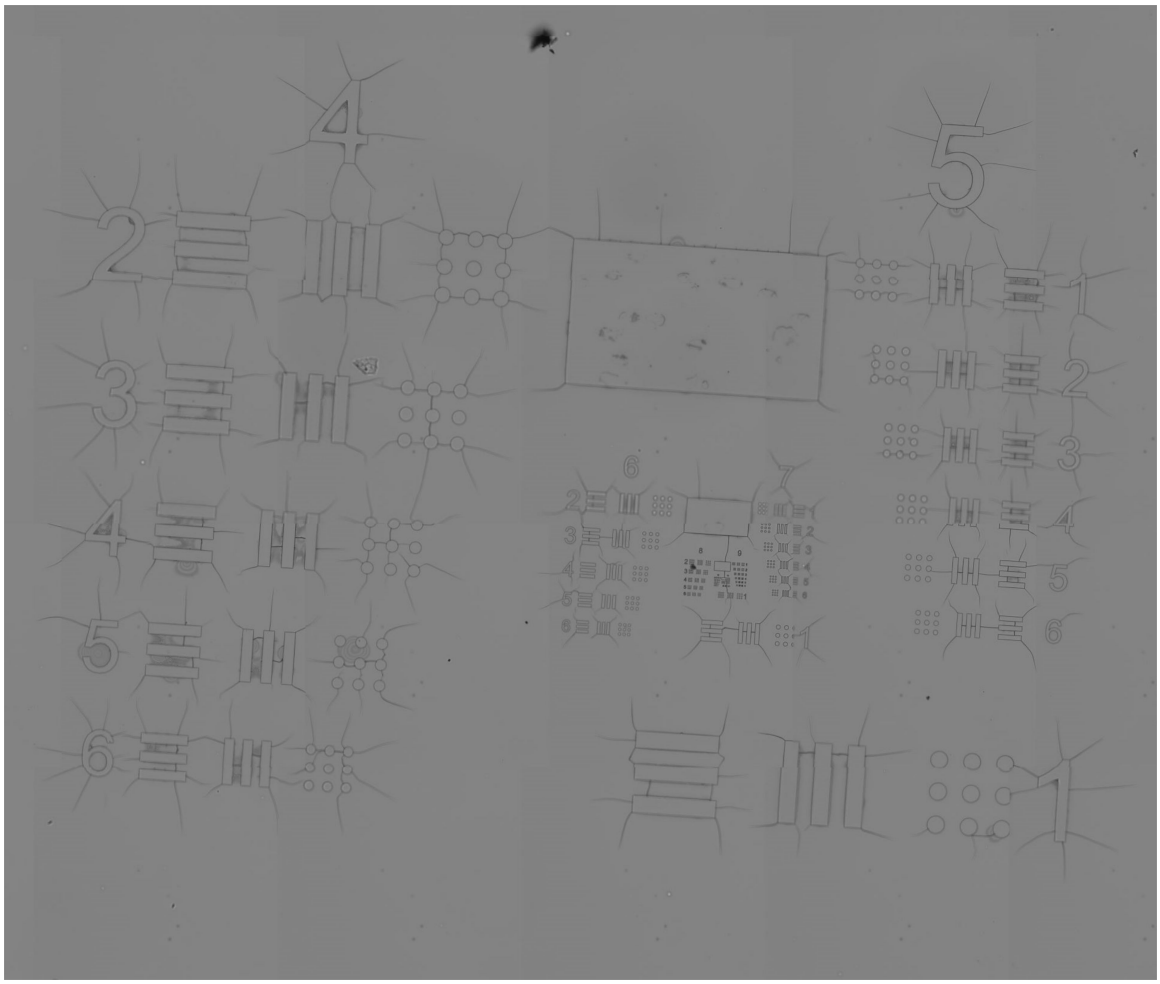

Figure 5.9: *Microscope image of manufactured resolution test chart with negative pattern in 2.5* µm *PMMA on* CaF_2.

magnification was used for imaging, resulting in an effective pixel size of 5.5×5.5 µm (1.1×1.1 µm with high magnification optics). The interferometer was configured to provide 4 cm^{-1} spectral resolution.

Figure 5.10 shows the MIR transmission spectrum (A) from the target and the corresponding hyperspectral image (B). First off all it is to note that the image itself contains artefacts produced by the imaging system. The image consists of a grid of 3×4 acquisitions stitched together to form a big mosaic image. This process unfortunately is done by Agilent software in an automated fashion with no possibility to fine tune for the user. The individual tiles are not aligned correctly as evident in the horizontal bars forming feature 2 of group 4. Feature 1 of group 5 is also not aligned correctly as the tiles do overlap which is not accounted for. This results in the image displaying 4 bars instead of 3. The border areas between tiles have to be seen critically in the evaluation. Figure 5.10 C shows the absorbance values for the cross section along feature 1 to 5 of group 5, highlighted in subfigure B in red for different wavelength (colour coded in subfigure A, as well).

As discussed in section 5.1 already, these intensity profiles can be used to estimate the spatial resolution of an imaging system. Here the effect of different spatial resolution for different wavelengths in the hyperspectral image is evident. In the profile of the 2947 cm^{-1} image, all elements are clearly resolved (apart from element 5 which is covered by a piece of dust), whereas for 1148 cm^{-1}non of the elements are resolved any more. Another interesting observation is the fact that the contrast does not appear to be homogeneous across the field of view of each individual tile. This can be seen in the stitching artefact present at feature 1 of group 5 where the two lower bars are present in both tiles but show different absorbances.The spectral profiles (see figure 5.11) scanned across a feature 5 of group 4 do not show major spectral distortions.

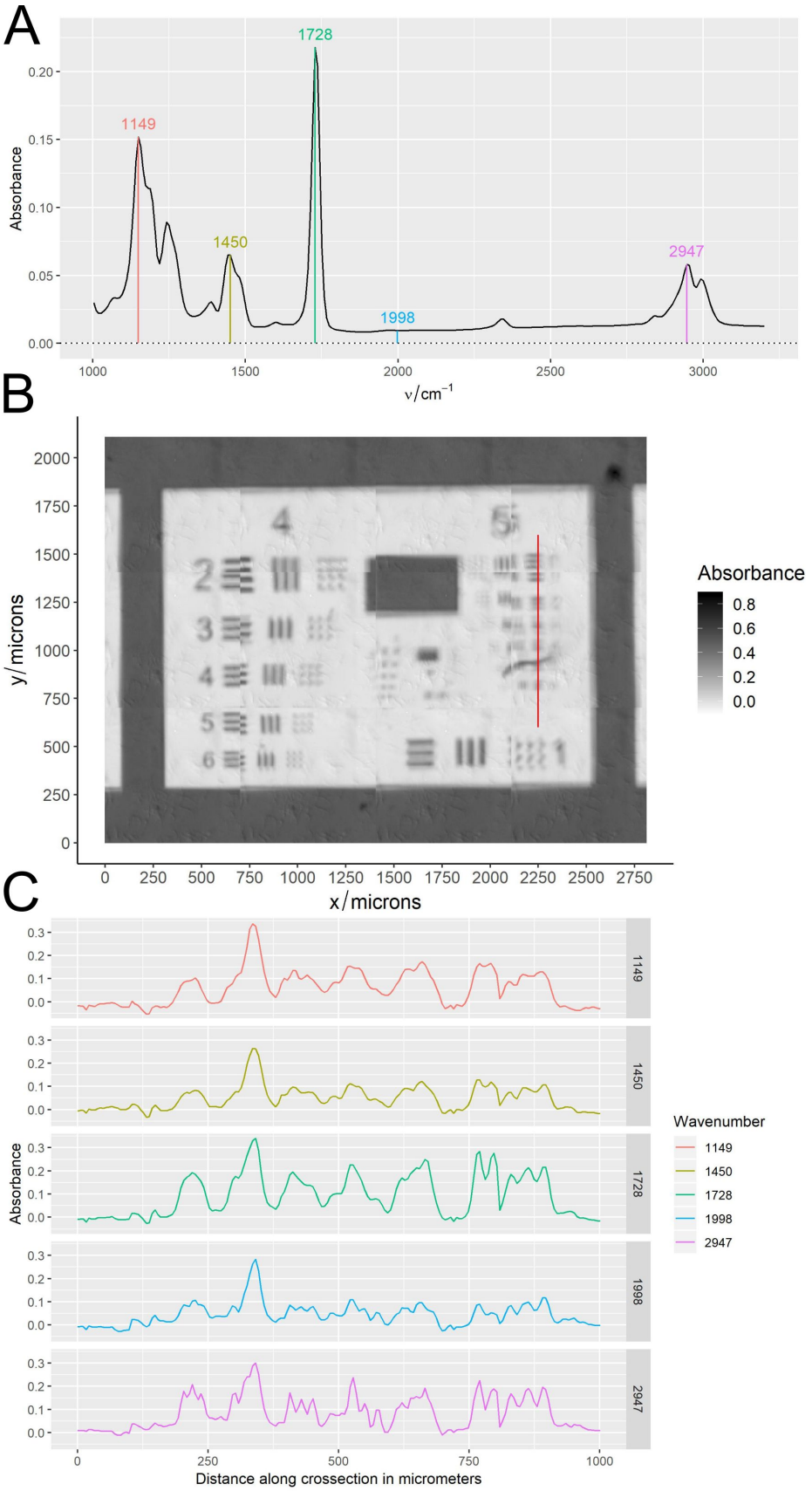

Figure 5.10: *FT-IR spectrum of target composed of PMMA (A). MIR image of PMMA positive feature resolution target (B). Absorbance cross section along red line in subfigure B (C).*

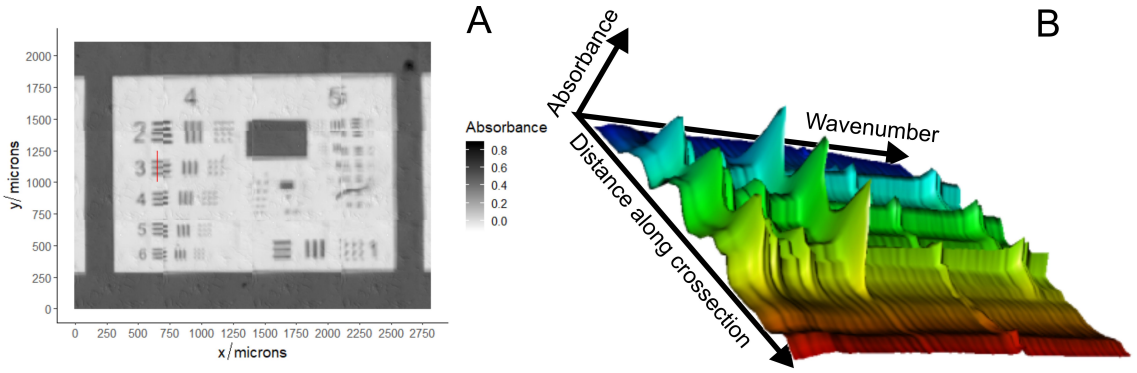

Figure 5.11: *(A) MIR image of PMMA positive feature resolution target and (B) spectral profile of the finger print region across feature 5 of group 4 (red line in A)*

5.5 Discussion

The design of a new resolution test chart was demonstrated here covering spatial features from 31.25 µm to 550 nm in size. Much work in this regard remains to be done until the new design can be used routinely. The stability of PMMA is an issue for example which needs to be addressed. A promising alternative is the photoresist SU-8 which is chemically highly stable, but difficult to spin coat onto CaF_2. Furthermore the dot features can be used to investigate scattering phenomena often being a problem while working with biological cells.

6 QCL Imaging for Oesophageal Histopathology

6.1 Introduction

Evaluation of histological tissue sections is the standard procedure to diagnose cancers, yet evaluating those is a time intensive and highly subjective process [10]. In order to speed up the process and to make it less observer dependent, MIR imaging has been proposed as a tool which, in combination with machine learning approaches, has shown promising results in several proof of concept studies [8, 103, 104, 133, 171, 172, 174, 175, 178–181, 222, 234, 236]. Two recent reviews on this topic were presented by *Hermes et al.* [1] and by *Wrobel and Bhargava* [237]. Yet the clinical translation of this technology is still in its development phase. In order to achieve an observer independent workflow, much work regarding standardisation of procedures remains to be done [184]. This chapter evaluates the influence of sample preparation on MIR hyperspectral data analysis and compares two DF-IR systmes to an FTIR.

There are two main procedures for obtaining histological sections of biopsy tissue for clinical diagnostics. In order to preserve the biochemical information contained in the specimen, the tissue biopsy can be snap frozen in liquid nitrogen and cut with a cryomicrotom. This however often produces artefacts in the sections due to folding and ripping of the sections. The other option, which is much more common, is to apply chemical fixation with formalin and then embed the specimen in paraffin prior to cutting with a microtom.

Formalin fixed paraffin embedded (FFPE) sectioning tends to produce less cutting artefacts and the remaining tissue block can be archived in a tissue bank, but the fixation procedure removes all of the volatile components of the sample such as free lipids. Most clinical workflows use FFPE sections as they are much more stable and therefore more convenient to work with. Therefore, this study focuses on the evaluation of FFPE samples.

The use of FFPE samples has been demonstrated with Fourier Transform microspectrometers (FTIR) utilising incoherent light sources such as a globar. The influence of

the paraffin for this setting has been evaluated by *Nallala et al.* [113]; they also propose a chemometric workflow to eliminate spectral contributions of the paraffin referring to it as 'electronic deparaffination'. This work builds on the study of *Nallala et al.* by considering the effect of coherent light sources as well. Furthermore, the effect of electronic deparaffination on the downstream machine learning procedure to classify pathology groups from FFPE tissue sections is evaluated.

6.2 Material and Methods

6.2.1 Tissue Samples

The sample investigated is a tissue micro array containing two samples each, from 35 patients with oesophageal adenocarcinoma and 5 healthy controls. Three consecutive sections (7 µm tick) have been purchased from US Biomax. The first section has been mounted on a calcium fluoride slide (Crystan) for investigation with an FTIR system, the second one on a MirrIR slide for investigation with QCL discrete frequency imaging, and the third one on a standard histological glass slide to provide gold standard reference information from a histopathologist via H&E staining as depicted in Figure 6.1.

6.2.2 Data Acquisition

FTIR images were obtained using an Agilent Cary FTIR system (Agilent 670 FTIR spectrometer coupled with an Agilent 620 FTIR microscope). The system consists of a globar source, and a liquid nitrogen cooled 128×128 pixels focal plane array (FPA) mercury cadmium telluride (MCT) detector. A Cassegrain IR objective with numerical aperture (NA) of 0.62 and 15× magnification was used for imaging, resulting in an effective pixel size of 5.5×5.5 µm. The interferometer was configured to provide $4\,\mathrm{cm}^{-1}$spectral resolution.

QCL discrete frequency (DF) imaging was performed on an Agilent LaserDirect IR imaging system with a transflection sampling geometry. The instrument scans a diffraction limited laser spot over the sample and was configured to record absorptions point by point with 3 µm step size via a 0.72 NA refractive objective and a room temperature bolometer detector. The laser source was tuned to acquire images every $8\,\mathrm{cm}^{-1}$between 950 and $1800\,\mathrm{cm}^{-1}$.

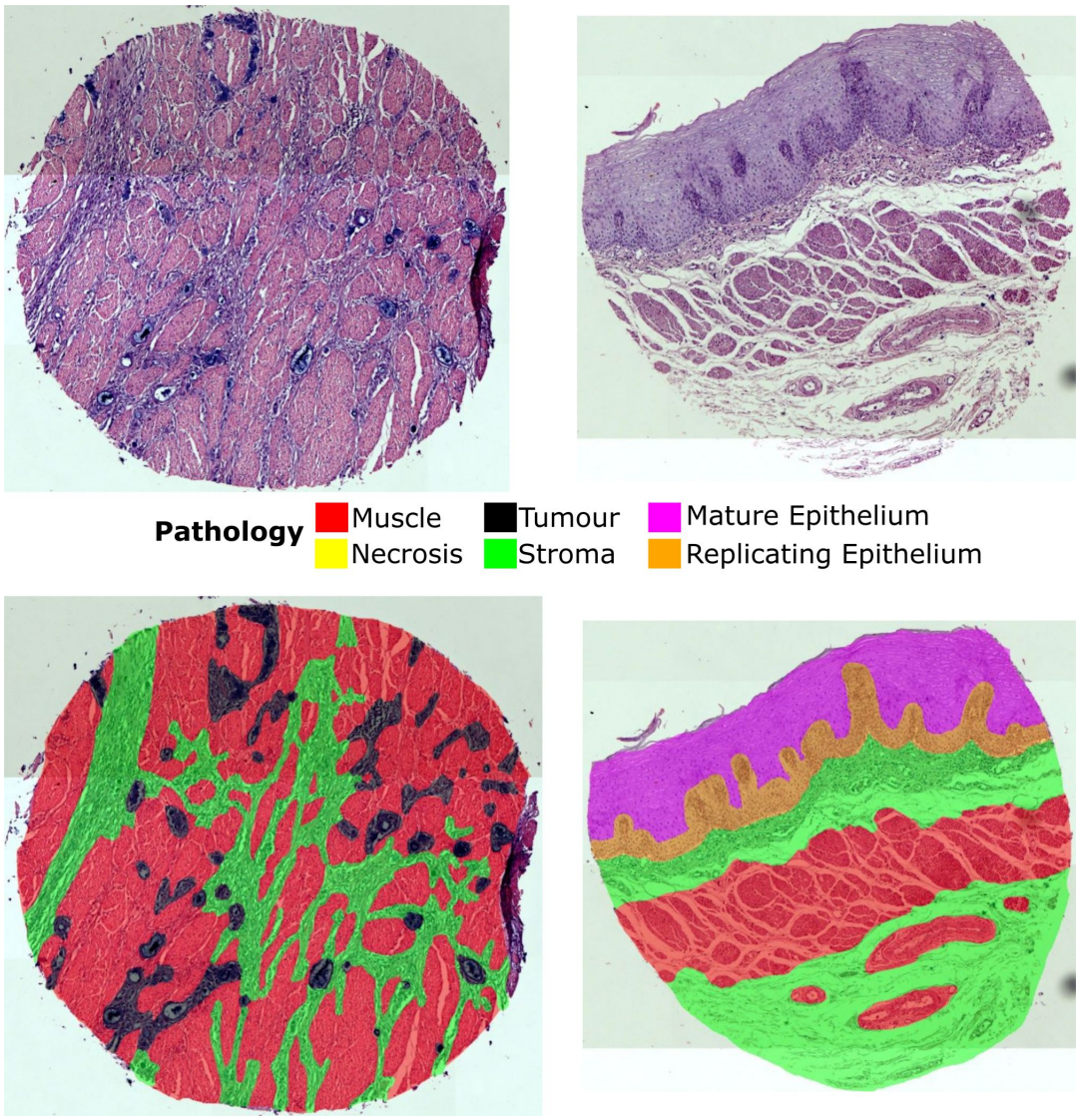

Figure 6.1: *Tumour (left) and healthy (right) sample (top) annotations (bottom)*

A second set of DF images of wavelengths, that were specifically selected based on the study by *Old et al.* [171] was measured using an in-house built QCL system. Namely at the frequencies (in cm^{-1}) of: 995, 1024, 1030, 1045, 1082, 1108, 1117, 1143, 1162, 1216, 1238, 1254, 1271, 1304, 1338, 1353, 1369, 1374, 1395, 1440, 1452, 1465, 1475, 1483, 1510, 1535, 1546, 1563, 1587, 1632, 1653, 1658, 1673, 1687, 1727, 1743, 1765, 1780.

The system consists of a multi chip QCL unit (LaserTune, Block engineering) covering the mid-IR fingerprint region from 770 to 1940 cm^{-1}, with wavelength dependent peak output power between 10 and 100 mW. A 0.56 N.A. image formation lens provided a diffraction limited laser spot on the sample, which was scanned across the image area using a high-speed linear motor microscopy stage (Prior). The transflected radiation was recorded using a liquid nitrogen cooled, single-element MCT detector. The design process and configuration of the system is described in great detail by *Mittal and Yeh et al.* [238].

For both imaging procedures, the samples were measured first when they were still embedded in paraffin. Then the paraffin was removed by submerging the sample in n-hexane overnight, afterwards the samples were measured again using the same acquisition settings. A second subset version of the mask was created as well leaving clearance between pathology borders and leaving out areas that are difficult to classify.

The H&E stained section was imaged under a standard white light microscope (Zeiss AxioScan) with 10× magnification in reflection mode. The images obtained were printed out and handed over to an expert pathologist (Prof. Neil Shepherd) for annotation.

6.2.3 Image Preprocessing

The annotations obtained from the pathologist were digitalised using the original white light images. The images were loaded into the open source software GIMP and a false-colour mask was drawn manually and exported as a separate file (png).

The MIR images obtained from both FTIR and DFIR systems were loaded in their proprietary formats onto Matlab, then cropped and co-registered with the H&E images and the pathology masks using Matlab‘s built-in image registration tools. This procedure assigned pathology information to every pixel of the MIR image.

6.2.4 Spectral Preprocessing

The coregistered data were loaded into R via the 'hyperSpec' package. All images were cropped to uniform spectral range of 1000 to 1800 cm^{-1}. The images from the sections still embedded in paraffin were then electronically deparaffinated using a modified version of the algorithm proposed by *Nallala et al.* [113] written in-house. The images after chemical deparaffination were baseline corrected using a linear baseline fit. After baseline correction or paraffin removal, respectively, the hyperspectral images were filtered excluding all areas that did not contain sample or had extremely low signal. The specific workflow with exact parameters and algorithms can be found in Appendix 4.

6.2.5 Data Analysis

The pre-processed images were further analysed in R using supervised classification tools provided by the packages 'caret', 'pls' and 'MASS'. The fully pre-processed dataset was split into test and training data. A 7-fold cross-validation scheme was set up selecting five patient samples each from the tumour patients and the healthy controls at random repeating this procedure to obtain 5 different splits each (See Appendix 5.1 for details). Figure 6.2 visualises the hierarchy, whilst the samples used for each model can be found in Table 6.1

Table 6.1: *Samples used in PLS-LDA training sets*

Set	Tumour Samples					Healthy Samples				
1	A2	B6	C10	E3	F8	H2	H8	H4	H8	H10
2	A4	B8	D1	E5	F9	H8	H5	H6	H9	H5
3	A6	B9	D4	E8	G1	H5	H6	H1	H9	H1
4	A8	C2	D5	E9	G3	H2	H7	H1	H9	H8
5	A9	C3	D7	F1	G5	H8	H6	H5	H7	H6
6	B1	C5	D10	F3	G7	H3	H7	H7	H9	H8
7	B3	C8	E1	F6	G9	H10	H9	H3	H5	H8

6.3 Results

It has been previously demonstrated by *Old et al.* [171] that mid-IR spectroscopy can be utilised to classify pathology of oesophageal tissue. Here the performance of discrete frequency systems in comparison with conventional FTIR imaging system is

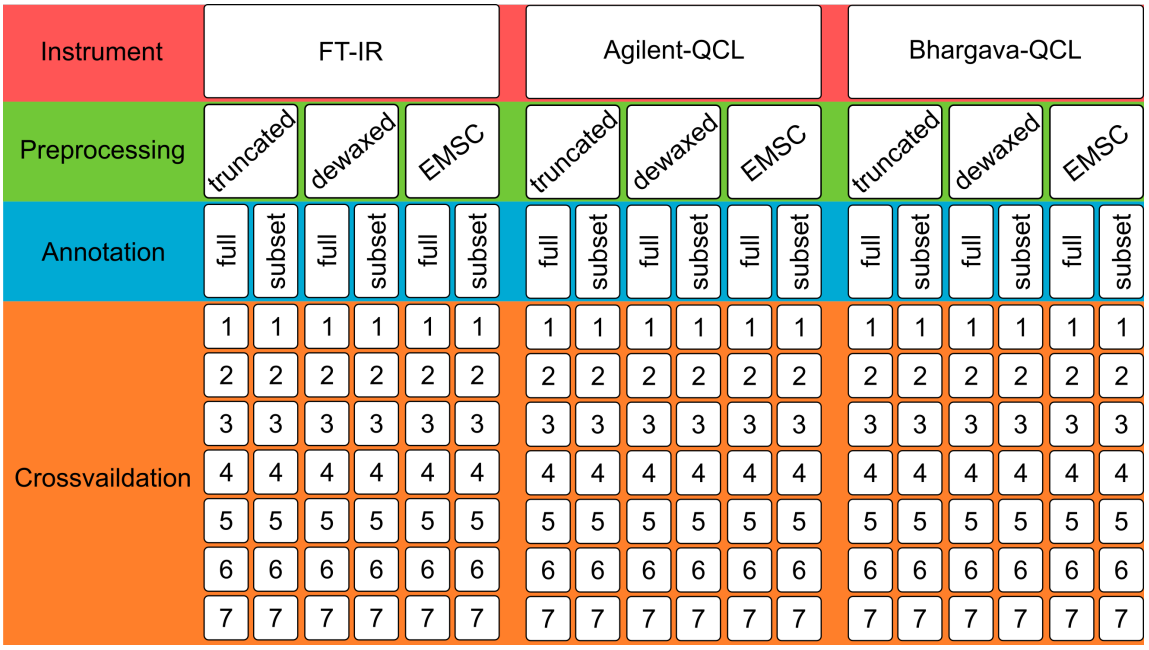

Figure 6.2: *Hierarchy of the design of experiments*

assessed based on sample processing. Therefore, the set of oesophageal tissue samples has been measured on both systems prior and after chemical removal of paraffin.

6.3.1 Instrumental Comparison

As depicted in figure 6.3, the images (raw data) obtained on the DF imaging systems (figure 6.3 A-D) compare well to those obtained on the conventional FTIR (figure 6.3 E-F). In the spectral dimension the number of channels measured with the DF systems can be scaled to the available measurement time, resulting in the potential for much faster acquisitions. Imaging the sample depicted in figure 1 took about 20 min on the FTIR system (1506 channels, 10k pixels), 1h 20min on the Agilent QCL system (106 channels, 31k pixels) and 20 min on the Bhargava‘s group system (40 channels, 70k pixels). Despite the decreased spectral resolution in the DF spectra, the general spectral quality for a region of interest (figure 6.3 G) is comparable. The image signal-to-noise ratio (SNR) for each channel (figure 6.3 H) is of the same order of magnitude, as well (see Appendix Section 3 for details on how SNR was calculated). There is however a notable difference in absolute intensity between the QCL systems and the FT-IR. One factor contributing to this is the fact that the QCL systems working in transflection effectively have double the interaction path length explaining a factor of two.

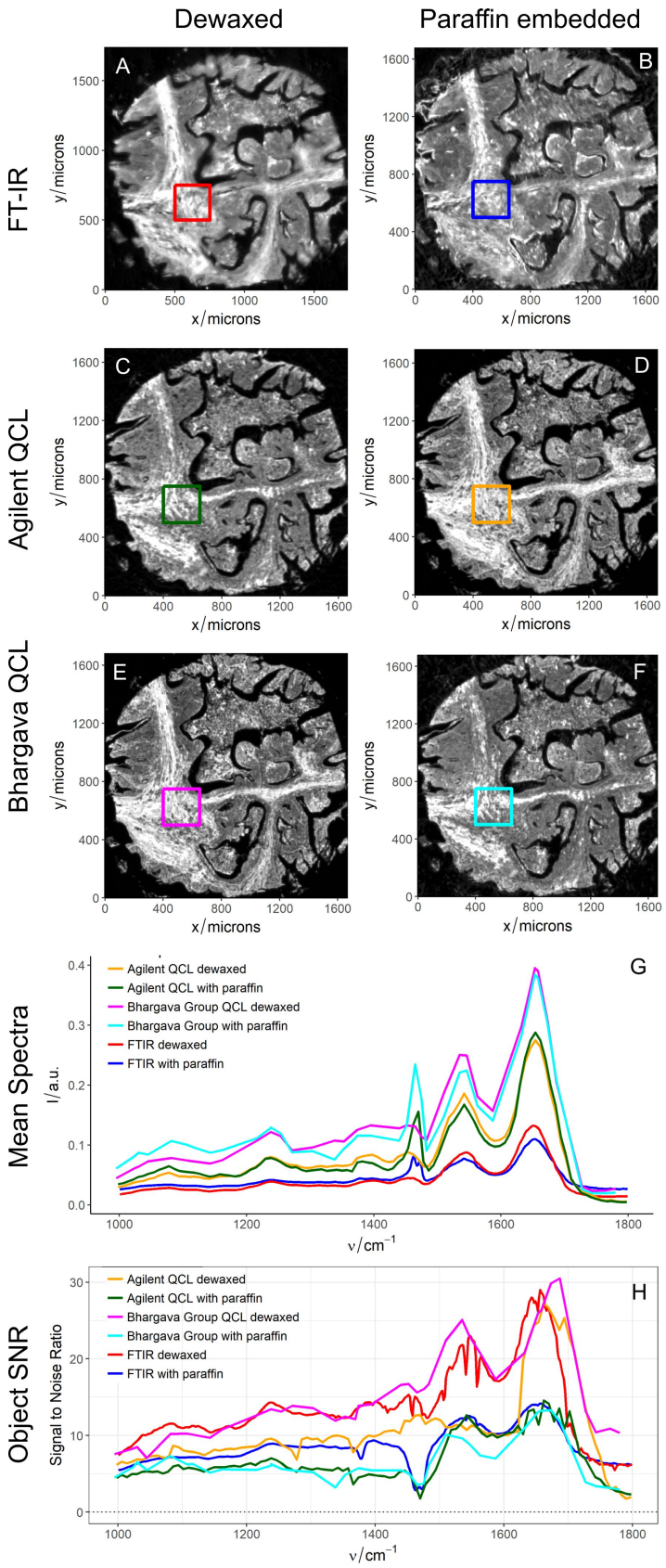

Figure 6.3: *A-F: MIR absorbance images at 1658 cm^{-1} for FT-IR and QCL systems with paraffin and dewaxed (7µm sections). G: Mean spectra of boxed areas in A-F colour-coded. H: Object signal-to-noise-ratios for images A-F.*

6.3.2 Dewaxing and Electronic Deparaffination

To evaluate the influence of paraffin embedding on the performance of classification, models have been compared for the dewaxed data as well as for the paraffin embedded. There are currently two different strategies to deal with the contribution of paraffin.

The first approach is to cut off the frequencies at which paraffin absorbs from the spectra and discard them during analysis.

The second, more sophisticated approach is to model the spectral contributions of the paraffin through a linear model which is referred to in the literature as extended multiplicative signal correction (EMSC) [113, 239] or as multiplicative curve resolution (MCR) [240]. This work uses a new algorithm written in-house in R.

The algorithm models the spectral profile of the paraffin based on the areas surrounding the tissue (where paraffin is the only component) and estimates contribution scores in the tissue using a non-negatively constrained linear model [241]. Thus a weighted paraffin contribution can be subtracted from each pixel spectrum. The algorithm is described in great detail with the full R code in Appendix Section 4.

6.3.3 Predicting Pathology Groups

After curating the 3 datasets: dewaxed data, truncated data and EMSC corrected data, the images from each data set were used to set up a PLS-LDA model calculating an LDA discriminant function from the first 10 PLS components. The model is set up to discriminate between 6 pathology groups, two malignant types namely ‘necrosis‘ and ‘tumour‘, and 4 benign types: ‘stroma‘, ‘muscle‘, ‘replicating epithelium‘ and ‘mature epithelium‘. The model training was performed in a cross validation scheme splitting the tumour patients into 7 groups of 5 patients each and assigning 5 random samples from the healthy patients (see Appendix section 5.1). For each of these splits, two models were trained, one utilising the full annotation of the entire image and the second one with further curation of sub-regions of interest where the assignment of pathology has a higher certainty.

The resulting 126 models were then used to obtain predictions from the samples not used in training. The overall performance has quite large variability between samples as well as between models, as discussed in more detail in Appendix section

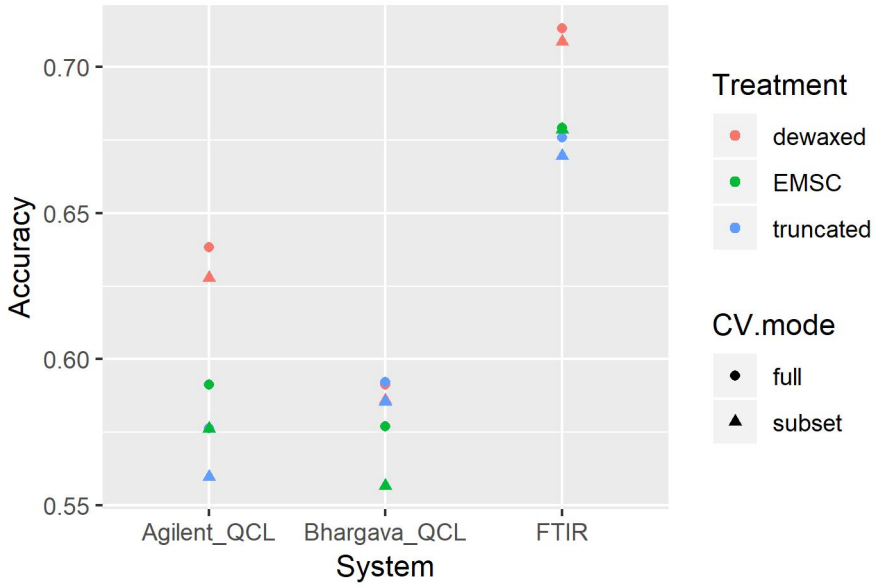

Figure 6.4: *Average model performance for PLS-LDA models for prediction of pathology groups.*

5.2. The mean accuracies for the systems, treatments and different annotation masks are plotted in Figure 6.4.

Considering the individual accuracies, chemical dewaxing is clearly working better than electronic approaches. The overall accuracies however are considerably low.

6.3.4 Discriminating between 'Benign' and 'Malignant' at the Pixel Level

In order to improve on the low accuracy, another layer was added to the classification method. The primary relevant information for the pathologist is whether the tissue is classified malignant or benign. If the pathology groups were aggregated into these two types, the overall accuracy increased substantially as depicted in figure 6.5.

The accuracies for the healthy samples increased even more than the overall performance, as depicted in figure 6.5. It is the tumour samples that showed worse performance, with a few samples in particular being classified with very low accuracies. This matches expectations, as oesophageal cancers are very diverse in appearance [242, 243] and the sample set was relatively small.

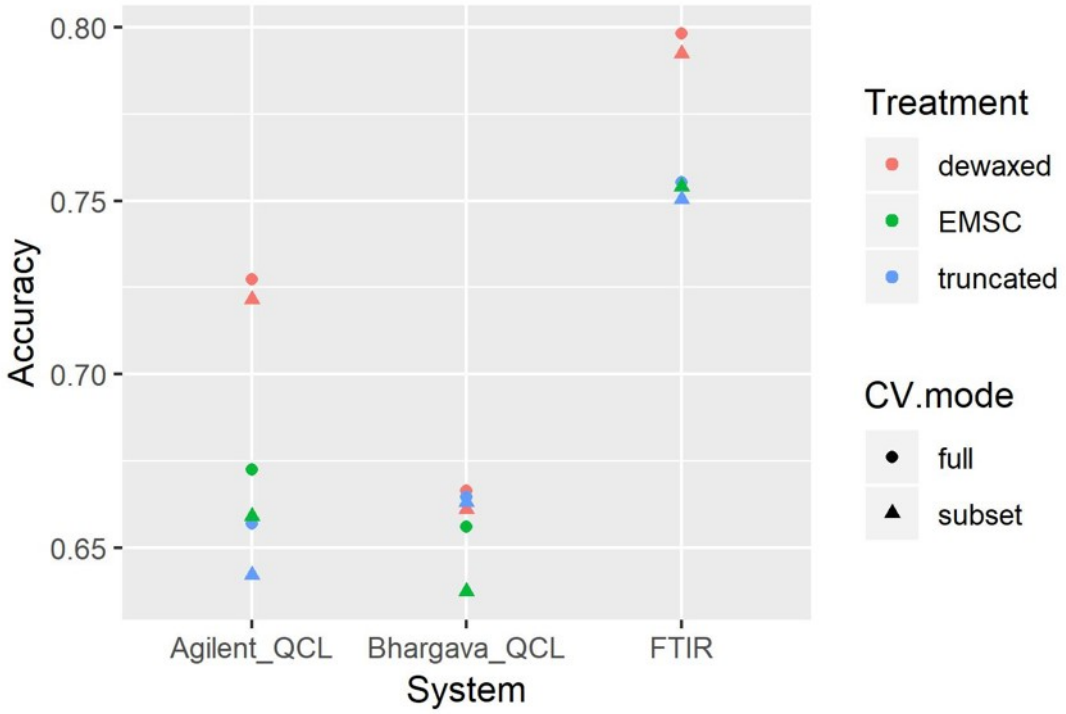

Figure 6.5: *Average model performance for PLS-LDA models for classification between benign and malignant.*

6.3.5 Whole Sample Threshold Voting

To further improve the classification, whole sample classification or threshold voting has been deployed as demonstrated by *Old et al.* [171]. Every sample with more then 30% of the pixels classified as malignant was therefore regarded as a tumour sample . This approach does result in 93 % accuracy (see Table 6.2 for classifier metrics and Appendix section 6 for details).

6.4 Discussion

FFPE tissue sections were used to discriminate pathological features using MIR hyperspectral imaging. Results clearly suggest that chemical dewaxing is the favourable sample preparation method and yields in better results than EMSC or truncation.

Data from the FTIR imaging system outperform those from the two QCL systems in terms of prediction accuracy. Data acquisition times for the data sets were similar for all three systems (ca. 15min per tissue core). It is however important to note

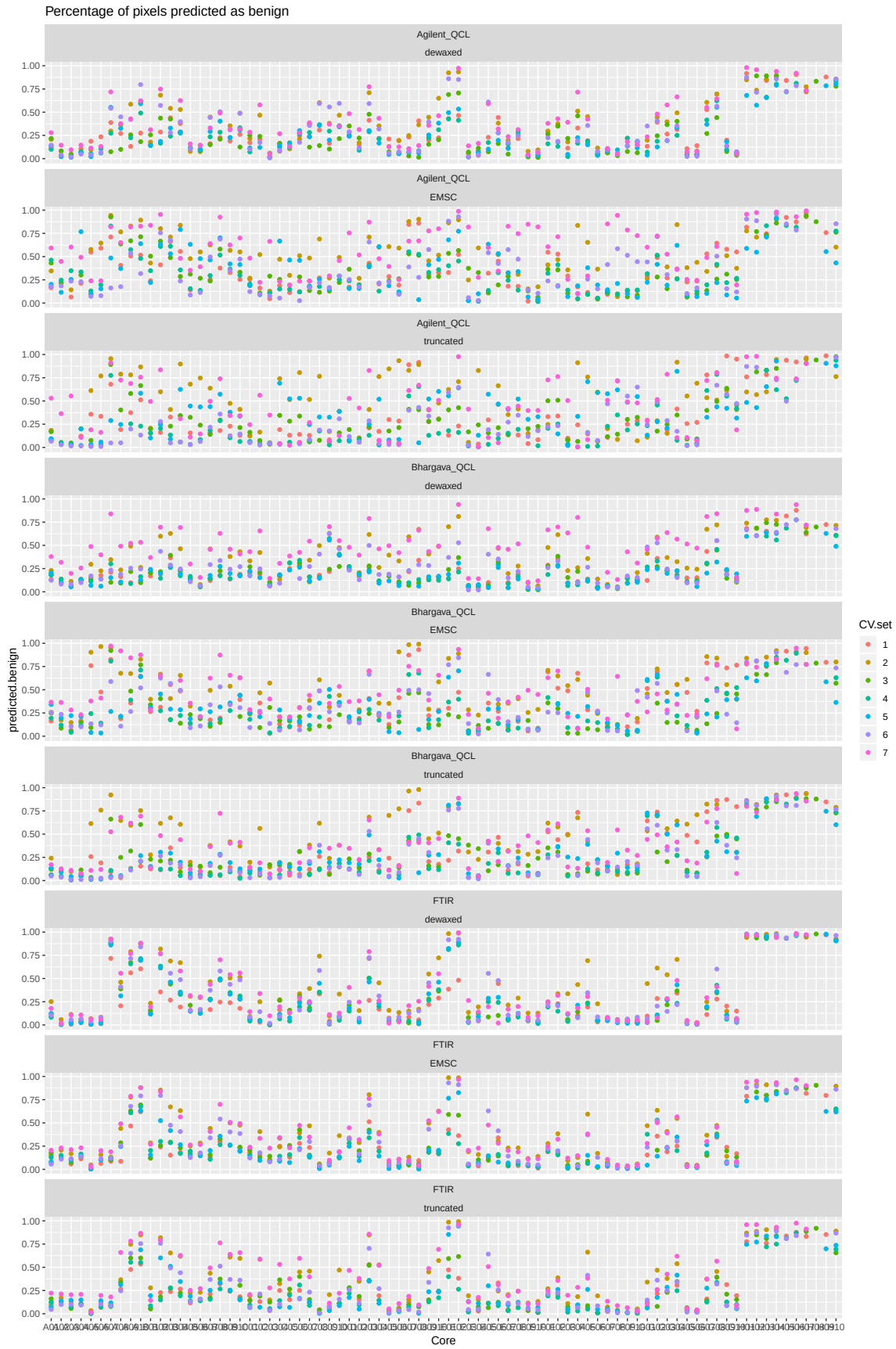

Figure 6.6: *Average model performance for PLS-LDA models for classification between benign and malignant for all samples.*

Table 6.2: *Performance metrics averaged over all 'full' PLS-LDA models.*

Confusion Matrix		
	Reference	
Prediction	Cancer	Healthy
Cancer	3838	59
Healthy	257	301

Summary Statistics	
Accuracy	0.9291
Kappa	0.6192
Sensitivity	0.9372
Specificity	0.8361

that it was not the aim of this study to optimise the acquisition speed for each system. The main focus during method development was on spectral quality. There are however different studies that have previously demonstrated methods to optimise the acquisition rates. Those require prior knowledge of the classification task. In FTIR imaging, spectral and spatial denoising can be used to increase acquisition rates while maintaining data quality [244]. The acquisition speed of DF imaging systems scales directly with the number of frequencies required for sampling the spectrum, therefore variable importance projections can be used to identify the most relevant frequencies and tailor the method exactly to the resources available [165].

This work developed an extended version of EMSC paraffin correction improving on the work of *Nallala et al.*[113] by estimating paraffin spectral contributions in a more robust fashion from the sample directly, instead of relying on separately measured library spectra.

The chemical removal of paraffin prior to MIR imaging has been debated in the scientific community, with some controversy between scientists in favour of removal and others opposing it. Especially with coherent DFIR systems, this question had not been addressed yet. *Piling et al.* [12] hypothesised that measuring tissue sections on DFIR systems without chemical deparaffination would prevent optical artefacts, assuming the paraffin serves as a refractive index matching medium essentially decreasing scattering contributions to spectra.

In this study, scattering artefacts could not be identified either in the data from the FTIR nor in those from the QCL systems. The study by *Piling et al.* used a different type of DFIR system, set up in transmission geometry rather than transflection geometry used in the present study. It is however known for FTIR imaging that

transflection geometry is more prone to spectral artefacts [245]. There are indications that coherent DFIR systems suffer worse from those artefacts [100]. The origin of these pertubations, however is still debated [102].

Piling et al. suggested that the presence of paraffin is beneficial in transmission geometry, but do not provide evidence to support this claim. A different set of studies by *Gerwert et al.* [236, 246] which utilised the same type of transmission DFIR system as *Piling et al.* did use chemically dewaxing and did not report artefacts. This should however be directly addressed in a further study comparing systems which do not differ in sampling geometry as this is a confounding factor which can only be discussed indicatively here.

Looking at these two approaches in context of this work, there are no advantages to report for leaving paraffin on the samples. This study rather suggests that there are even benefits to removing it chemically as indicated by the better classifier performances for the dewaxed samples. As reported by *Fullwood et al.*[247] and *Nalalla et al.* [113], across a variety of different chemical dewaxing methods, none of them was capable to remove paraffin entirely from the sample. These studies furthermore report that the remaining paraffin content correlated with the tissue types and their density. Therefore, paraffin remainder could potentially be used as an indirect marker for tissue density.

The classification models as such do not perform as well as it was expected. The challenge is clearly the small sample set with an unbalanced number of healthy controls. Having only 5 samples per group is clearly not enough to capture and account for the high variance in biological materials. The samples size is too small to be able to infer whether this approach would work in a clinical routine. As theoretically determined by *Beleites et al.* [248], to reliably demonstrate whether these kinds of models work, hundreds of samples per group would be required. This issue is further discussed in the outlook (see section 8.2.1).

7 Upconversion MIR Imaging

Disclaimer: This chapter is an adaptation from a submitted paper manuscript entitled: 'Video-rate, mid-IR hyperspectral upconversion imaging' [249]. The manuscript was still under review to the date of submission. The setup of the imaging system was built by the main author of the publication Saher Junaid and fellow co-author Chaitanya Kumar. The author contributed the samples to the experiment and did the data analysis.

7.1 Introduction

Mid-IR hyperspectral imaging (HSI) is of major interest in diverse fields from medical diagnostics [11, 133, 223, 234, 250], to environmental monitoring [251–253], geology for mineral identification [254], and within the food industry [255]. The widespread applicability of the mid-IR wavelength range (e.g. 2 to 15 µm) is intimately linked to intrinsic properties of molecular absorption.

As MIR spectroscopy and imaging delivers highly specific information, applications are in need of sensitive, faster detectors, and cameras operating at room temperature to efficiently harness this potential [253]. FTIR spectroscopy is toady's preferred technique for MIR imaging as discussed in chapter 2. A major limitation to those systems is, that the cameras used for MIR detection are predominantly based on MCT, InSb or microbolometers, which either require cryogenic cooling and are of high cost or have poor noise characteristics [256].

Moreover, for HSI, large data storage and complex post-processing software is currently needed to transform raw data into useful information [106]. Recent developments in mid-IR hyperspectral microscopy including tunable QCL illumination combined with either raster scanning [238] or microbolometer array detectors [236] have shown their potential to outperform FTIR systems for special applications.

Non-linear frequency upconversion provides an alternative route to enabling fast, room-temperature mid-IR spectroscopy and imaging, due to orders-of-magnitude

higher sensitivity and speed compared to direct mid-IR detectors [74]. A significant drawback in previous demonstrations of upconversion imaging has been the need for extensive post-processing to obtain a large field of view (FoV), which in turn prevents its use for fast 2-D data acquisition or real-time video-frame-rate imaging [74, 257, 258].

In this chapter, first attempts utilising upcoversion for MIR spectral histopathology are presented. Initial feasibility experiments are discussed first. This experience gained was afterwards used to build a high-speed upconversion mid-IR monochromatic imaging system. A synchronously-pumped OPO served as MIR illumination source. This was combined with an upconversion detection scheme utilising a lithium niobate crystal as non-linear medium, transferring the MIR signals to the NIR wavelength range for image acquisition with a standard CCD camera.

7.2 Preliminary Experiments with Upconversion

7.2.1 Globar and Upconversion

In a very first attempt to use upconversion detection for biomedical diagnostics we tried imaging a tissue section mounted on CaF_2 in collaboration with DTU Fotnik. An upconversion module as described by *Dam et al.* [74] was used with globar illumination. Figure 7.1 shows the image obtained.

The quality of the image was poor, as the spatial resolution was too low and there was no way to recover the hyperspectral information therefore the experiment was not further evaluated. Increasing the spatial resolution however was not possible as the module did not have sufficient sensitivity to image at higher magnification with the globar.

7.2.2 QCL and Upconversion

As the setup of the upconversion module in combination with globar illumination did not provide satisfying results the globar was swapped for a 6 µm wavelength QCL and the magnification optics were upgraded to provide higher magnification. Figure 7.2 shows the image obtained.

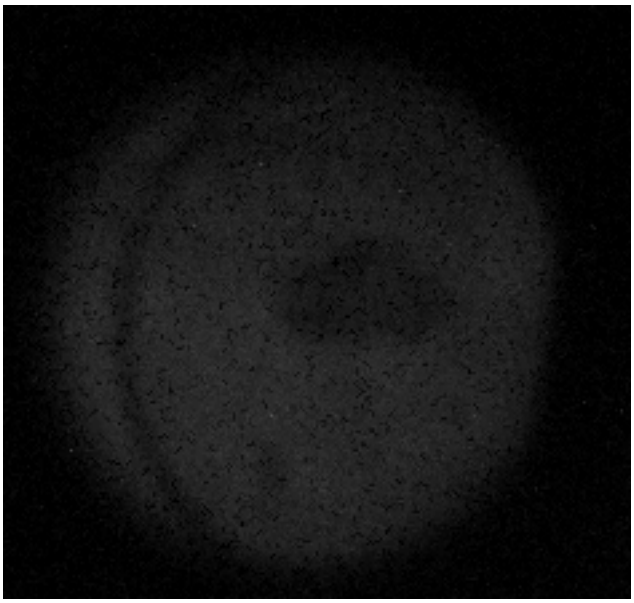

Figure 7.1: *Mid-IR image of tissue section measured with globar illumination on upconversion module described by Dam et al. [74].*

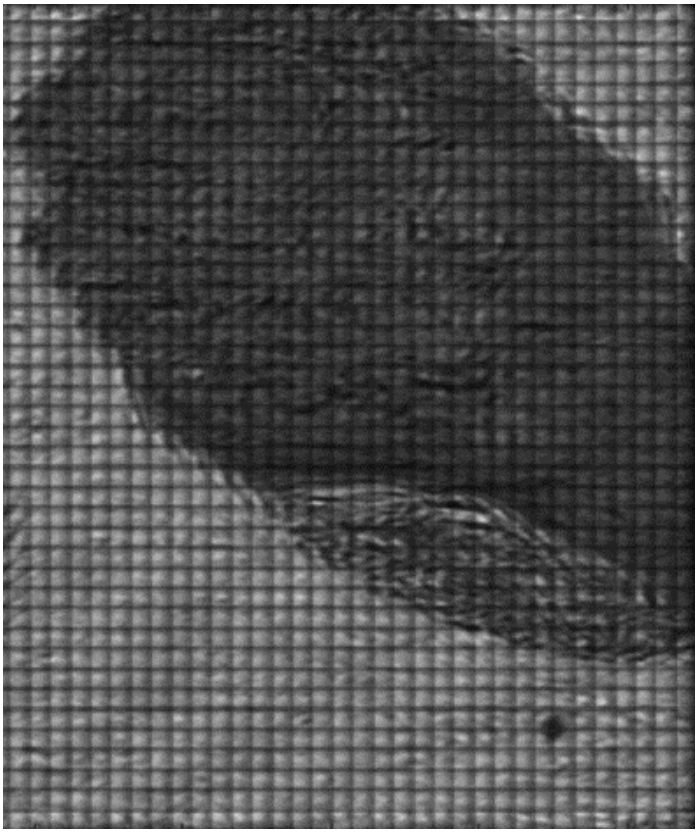

Figure 7.2: *Mid-IR image of tissue section measured with QCL illumination on upconversion module described by Dam et al. [74].*

The image has better magnification but still very poor contrast therefore the setup replaced by the experiment described in the following section 7.3.

7.2.3 Supercontinuum Source and Upconversion

A second experiment with the same sample was conducted utilising a supercontinuum source and a different upconversion approach as described previously by *Huot et al.* [259]. The setup (see figure 7.3) consisted of 1550 nm erbium fiber laser as the pump source for both the supercontinuum generation as well as the upconversion. The pulse was then separated into two arms with a 90 to 10 fibre coupler. The higher power pulse was propagated through single-mode silica fibers and a passive thulium-doped non-linear fibre to generate a supercontinuum emission of 1.8 to 2.6 µm with an average power of approximately 200 mW. The supercontinuum was then transmitted through the sample. After passing through the sample the beam was recombined, using convex gold mirrors (pump beam passed through a hole in the middle of the mirror), with the pump beam focused in a non-linear lithium niobate crystal for upconversion to 860 - 970 nm. The upconverted signal was then detected with a standard CCD.

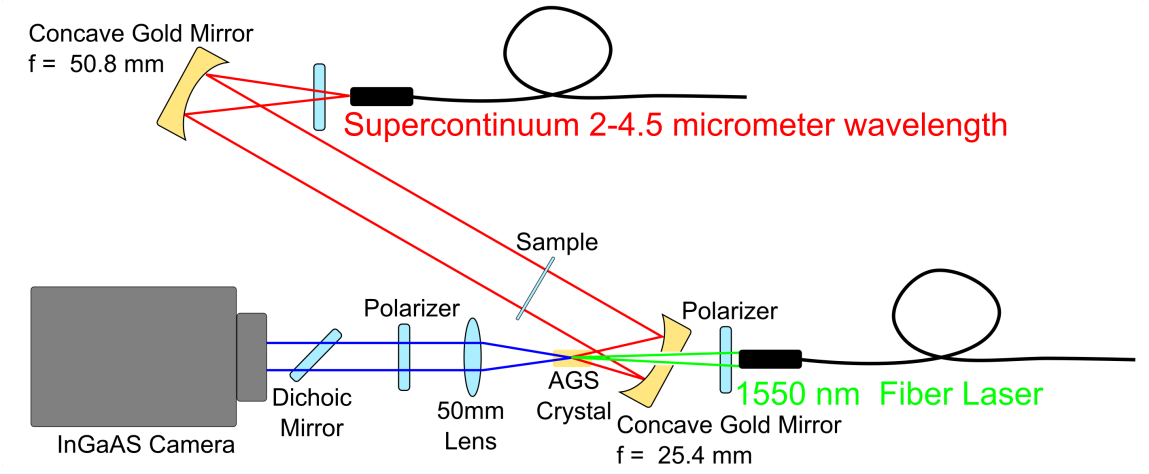

Figure 7.3: *Sketch of Optical Setup of MIR imaging system described in Huot et al. [259].*

As the upconversion phase matching strongly depends on the angle of incidence of the beam into the non-linear upconversion crystal, (as described in 2.3.3) illuminating the sample with a broadband source results in an effect similar to placing a grating in the illumination path in the image. The angles are different for each pixel resulting in the different wavelength being upconverted in different parts of the image [258].

This profile was measured by scanning a fibre optic probe mounted on a micrometer stage across the upconversion profile in the image plane. Figure 7.4 shows an image obtained on the setup with the wavelength profile overlaid onto the image. This process lacks accuracy, however, as the only point of reference to co-register the scan with the image was the hole in the gold mirror.

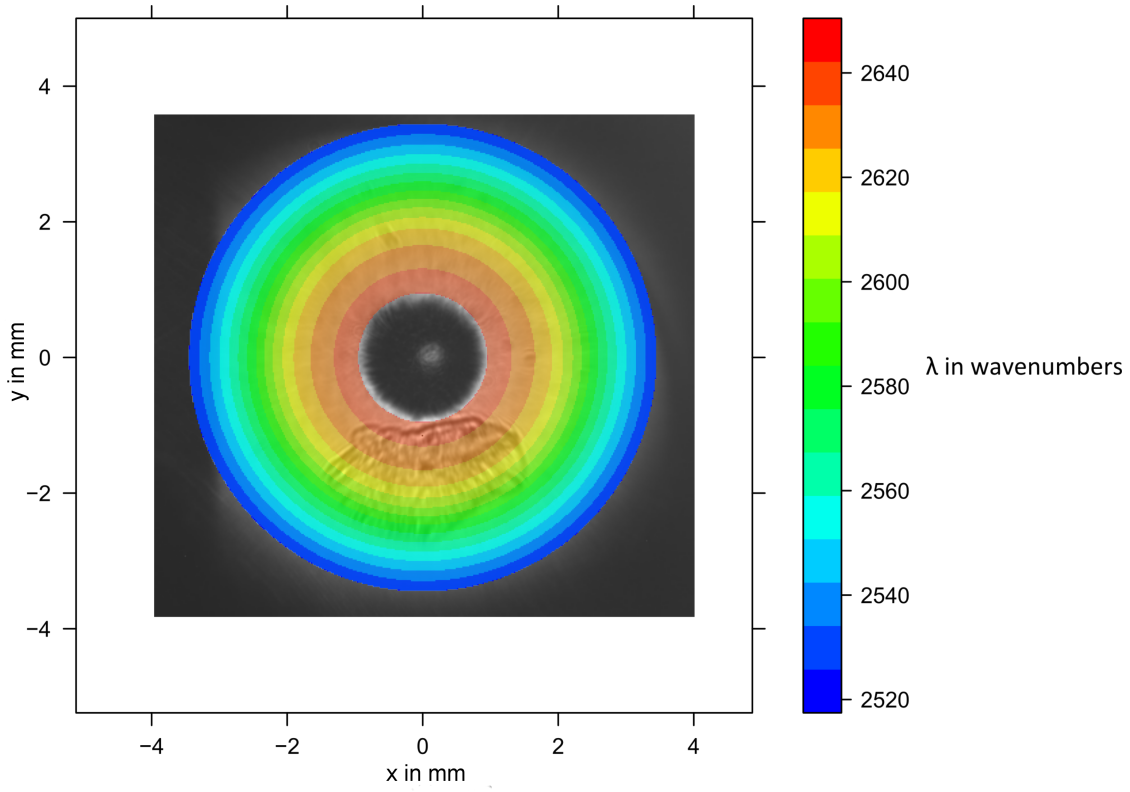

Figure 7.4: *Mid-IR image of tissue section measured with supercontinuum illumination on upconversion arrangement described by Huot et al. [259]. The image is overlaid with a visualisation of an estimation for wavelength upconverted at the respective pixels.*

7.3 OPO Upconversion Optical Setup

Disclaimer: This subsection is a description of the OPO upconversion setup built by S. Junaid and C. S. Kumar, modified from [249]. The author was involved in the preliminary experiments leading to building this instrument and assisted in defining the required specifications.

As the preliminary experiments suffered from poor optical design, this was addressed by building a new system in an integrated approach.

The setup (see figure 7.5) for upconversion of monochromatic images uses the idler beam from a ps OPO as the MIR illumination source. The OPO is synchronously pumped at 1064 nm by a ps Yb-fiber laser operating at a repetition rate of approximately 80 MHz (Fianium, FP1060-20; approximately 20 ps pulse length; approximately 1 nm bandwidth). The power of 15 W, was split 2:1. 10 W to pump the OPO, and 5 W (attenuated to 1.5 W to avoid saturation of the CCD camera) serving as a pump field for the upconversion process via sum-frequency-generation (SFG).

The synchronous upconversion pumping scheme inherently locks the mid-IR OPO pulses and the pump laser pulses, minimising timing jitter to ps scale. This intrinsic feature of synchronously-pumped ps OPOs allows operation of the upconversion setup in passive fashion, using a fixed delay line to synchronise the MIR OPO pulse and the pump pulse to coincide inside the non-linear crystal [260]. Therefore, synchronous pumping is highly efficient, as the high peak power pulses interact in perfect temporal synchronism, resulting in efficient upconversion.

A MgO-doped periodically-poled $LiNbO_3$ (MgO:PPLN) crystal is used as the non-linear medium in the OPO, generating the signal and the idler beam. The crystal is operated at constant temperature. Depending on the desired wavelength, either the signal or the idler beam is accessible for illumination. The signal wavelength can be tuned in the range of 1.43 to 1.98 µm with a bandwidth of <2 nm. The idler beam correspondingly covers the range of 2.3 to 4.1 µm with a bandwidth of 4 to 6 nm depending on the specific IR wavelength. The illumination bandwidth defines the spectral bandwidth of the monochromatic images shown later. Further details of the OPO can be found in [261].

In this work, only the idler beam was used for illumination of the object. Its beam diameter was scaled to approximately 10 mm, defining the FoV in the object plane. Depending on the wavelength, an average power of 750-900 mW was available for illumination of the sample.

After passing the sample, the beam was focused (and recombined with the delayed remainder of the pump beam) into a lithium niobate non-linear crystal for upconversion via birefringent phase-matching. The large transverse dimension of bulk the lithium niobate crystal compared to a PPLN analogue, allows the use of a large pump beam diameter, enabling high spatial resolution in the upconverted images as the pump beam acts as a soft Gaussian aperture [76].

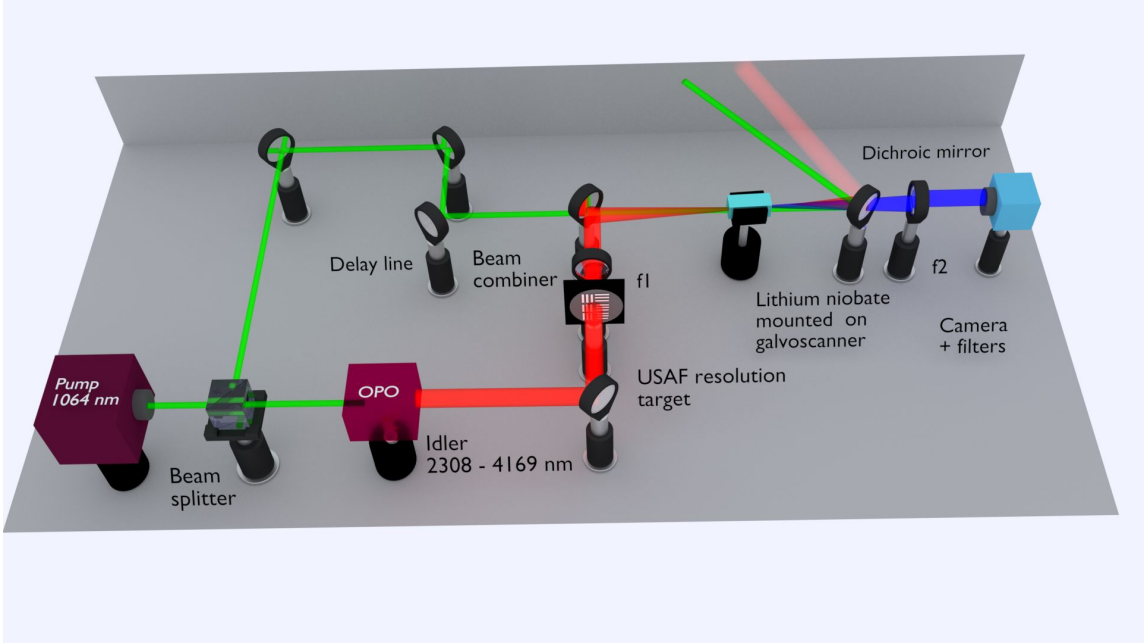

Figure 7.5: *Setup for upconversion-based imaging, reproduced from [249]. The idler beam from a ps OPO was used as an illumination source. A synchronised ps 1064 nm laser source functioned as a pump source for the OPO as well as for the upconversion. The beams were spatially and temporally overlapped in the non-linear crystal (lithium niobate) for efficient upconversion. The phase-matching condition was scanned by rotating the crystal in synchronism with the camera integration time. Lenses, (f_1 = 50 mm) and f_2 (50 mm, and 100 mm), were used at the front and back focal plane of the 4f setup. filters (short-pass 950 nm, long-pass 700 nm) were used to block the residual pump and stray light.*

The upconversion setup is implemented in a $4f$ configuration, the upconversion process takes place in the Fourier plane relative to the object. A first lens (f_1=50 mm) Fourier transforms the two-dimensional mid-IR object field to the centre of the lithium niobate crystal, where synchronous upconversion to the NIR takes place. The second lens (f_2 = 50 mm and 100 mm) Fourier transforms the upconverted NIR signal back to form the image at the CCD camera chip, see again figure 7.5. A silicon CCD camera (Andor Luca S) was used for the image acquisition. Residual pump and stray light were blocked by filters (short-pass 950 nm, long-pass 700 nm).

To increase the field of view beyond the angular phase-matching acceptance of the non-linear crystal, angular rotation of the crystal was utilised [262]. Rotation of the lithium niobate crystal angle by about 1° is implemented by mounting the crystal on a Galvano-scanner (GVS), using 'tangential phase- matching', see figure 7.6. This rotation increases the field of view by a factor of approximately 5 compared to a fixed crystal angle.

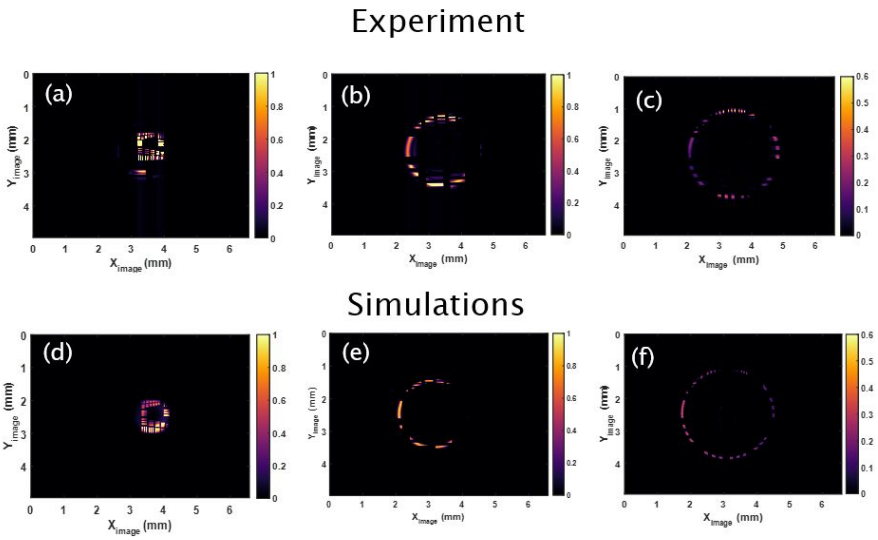

Figure 7.6: *Upconverted images of a USAF resolution target at 3.1* µm *by varying the crystal rotation angle (-4.7°, -4.3°, -4.0°), (d-f) and corresponding simulated images at the same angles, reproduced from [249].*

The FoV, using this approach, is limited primarily by the lens optics. The concept is not specific to this setup and can be applied universally for any upconversion imaging system. Another important feature of the scanning technique is the elimination of image post-processing for large FoV monochromatic image upconversion. By integrating all the upconverted sub-images, while scanning the crystal angle in a predefined range, a large FoV is obtained without the need for post-processing.

The monochromatic mid-IR upconversion imaging acquisition scheme was realised with 2.5 ms acquisition time per frame, thus effectively achieving video frame rate. The demonstrated spatial resolution estimated from an USAF chart comes to 35 µm within a 10-mm-diameter FoV in the object plane, see figure 7.7 and 9 µm with a 3 mm FoV.

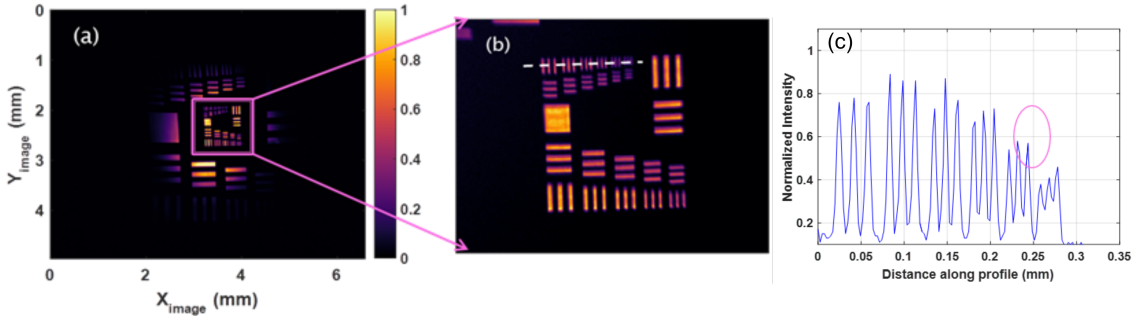

Figure 7.7: *(a) Upconverted image of a USAF resolution target at 3.1* µm *rotating the crystal by 1° using a GVS synchronised to the camera integration time of 2.5 ms. (b) Magnified version of the smallest features of the resolution target i.e. square box in (a), f_2 was changed from 50 mm to 100 mm focal length for magnification. (c) Intensity profile along the white line in (b) and pink circle highlights the smallest features, reproduced from [249].*

7.4 Methods

Disclaimer: The following sections are the authors own work contributed to the manuscript [249].

7.4.1 Tissue Samples

The sample used for investigation was a tissue micro array containing two samples each, of 35 patients with oesophageal adenocarcinoma and 5 healthy controls. Two consecutive sections have been purchased from Biomax.us. The first section has been mounted on a CaF_2 slide (Crystan) for investigation in the Mid-IR. The second biopsy was mounted on a standard histological glass slide to provide a gold standard pathology classification from a histopathologist (Prof. Neil Shepherd) via H&E staining. Here one healthy and one tumour sample were selected for investigation.

7.4.2 FTIR-Data Acquisition

FTIR images were obtained using an Agilent Cary FTIR system (Agilent 620 FTIR microscope coupled with an Agilent 670 FTIR spectrometer). The system consists of a Globar radiation source, and a liquid-nitrogen cooled 128 by 128 pixel focal plane mercury-cadmium-telluride detector. A Cassegrain IR objective with numerical aperture (NA) of 0.62 and $15\times$ magnification was used for imaging resulting in an effective pixel size of $5.5 \times 5.5\,\mu\text{m}$. The interferometer was configured to measure spectra with $4\,\text{cm}^{-1}$ spectral resolution.

7.4.3 Image Preprocessing

The annotations obtained from the pathologist were digitalised using the original white-light images. The images were loaded into the open source software GIMP and a false-colour mask was drawn manually and exported as a .png file. The MIR images obtained from the FTIR as well as from the OPO-upconversion system were loaded from the proprietary formats using MATLAB.

7.4.4 Upconversion Image Acquisition

To produce hyperspectral data, 62 HSI upconversion images were acquired (2.5 ms exposure time each) in the 2770 to $3345\,\text{cm}^{-1}$range. Namely at the frequencies (in cm^{-1}) of: 3344.48 3326.68 3304.69 3258.39 3245.70 3224.77 3198.98 3175.61 3154.57 3145.64 3139.72 3128.91 3126.95 3107.52 3107.52 3096.93 3086.42 3073.14 3069.37 3057.17 3048.78 3042.29 3036.74 3026.63 3025.72 3022.97 3015.68 2999.40 2997.60 2993.12 2979.74 2971.77 2969.12 2962.96 2956.83 2949.85 2942.91 2938.58 2936.00 2924.83 2923.98 2916.30 2904.44 2902.76 2896.03 2886.00 2877.70 2872.74 2869.44 2867.79 2857.96 2856.33 2849.00 2846.57 2836.07 2821.67 2814.52 2798.77 2790.96 2789.40 2779.32 2769.32

The biopsy images were then loaded into R via the ‘hyperSpec‘ package [263]. For comparison, an FTIR imaging system was included, with cropped in the spectral dimension, to match the spectral range of the OPO-upconversion system. The upconversion spectra were then smoothed using a Loes-function [263] and analysed using R‘s generic k-means functionality.

7.5 Biomedical Application

The mid-IR illumination beam diameter was scaled to match the size of the medical biopsy samples, which are 2 mm in diameter. The beam was then transmitted through the biopsy sample, followed by 5x magnification to match the upconversion system. See figure 7.8(a). The sample shown in the setup, figure 7.8(a) was a 7 µm thick section of a tissue micro array purchased from Biomax.us (sample ID: ES8011a), see section 7.4. The acquisition of two hyperspectral images, with and without the biopsy sample inserted, allowed for a pixel-by-pixel calculation of the transmittance of the sample, in this case at 3.34 µm , see figure 7.8(b). The spatial resolution at the object plane was approximately 9 µm .

The speckled pattern observed in figure 7.8(b) can be atributed to the temporal and spatial coherence of the illumination source. The bandwidth of the mid-IR OPO pulse was approximately 5 nm, exceeding the Free Spectral Range (FSR) of the 1 mm CaF2 substrate by 30 %, thus significantly reducing fringing from multiple reflections in the substrate. To remove the speckle arising from the spatial coherence in the image 5(b), a spinning, ground glass diffuser (Thorlabs DG10-1500) was inserted into the beam path. In this configuration, the illumination source was first reflected from the diffuser (figure 7.8(a)) and then scaled to match that of the biopsy. Figure 7.8(c) shows the image acquired using diffused, effectively incoherent light. As can be observed the coherent interference patterns were minimised, however the CCD camera integration time was increased to 400 ms to compensate for the insertion of the diffuser.

This HSI set-up was used subsequently. Figure 7.9 (bottom row) shows two stained biopsy images representing cancerous and healthy oesophageal tissue and the corresponding annotations, respectively. Figure 7.9 (first row) compares 2 biopsy images obtained with the FTIR and upconversion system respectively. Figure 7.9, (third row) shows the result of the k-means clustering in the spatial domain. Both morphology as well as the spectral classification of the images correlate well with the histopathology (figure 7.9 bottom row).

The FTIR images appear to resemble the pathologist‘s classification slightly better. These differences could be attributed to the better signal to noise ratio of the FTIR spectra. Figure 7.9 (second row) shows the k-means centre spectra.

To further compare the two systems, the images for the tumour sample are compared in the following way. In a real world application, the total intensity information is highly unreliable as it depends on the thickness of the sample. Sample thickness

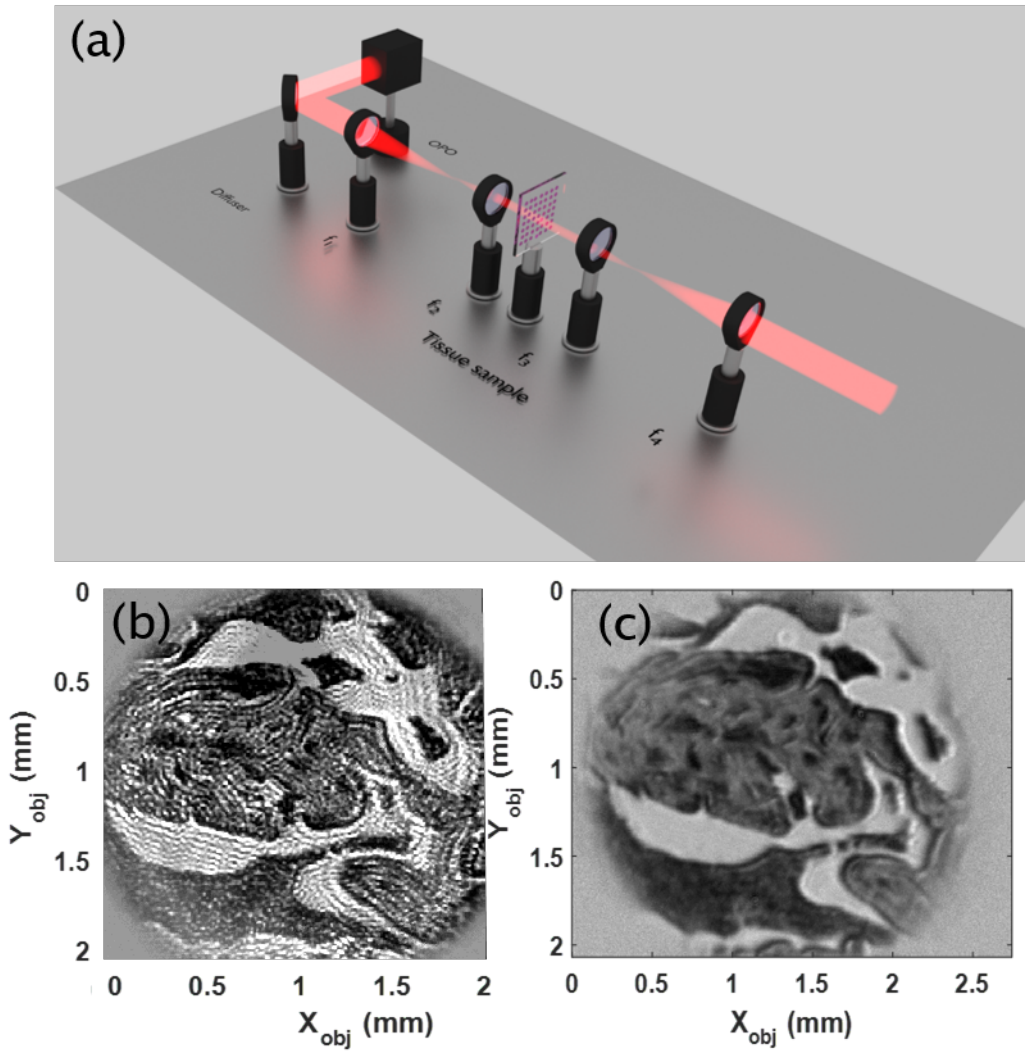

Figure 7.8: *(a) Magnification setup for the imaging of the tissue sample to resolve the smaller features of the sample. The original size of the beam emitted from the OPO is 10 mm, which is reduced to 2 mm, using a pair of lenses: $f_1 = 250$ mm, $f_2 = 50$ mm. (b) Image of the tissue sample acquired using upconversion at 3.34* µm *wavelength. (c) Image when using incoherent illumination, reproduced from [249].*

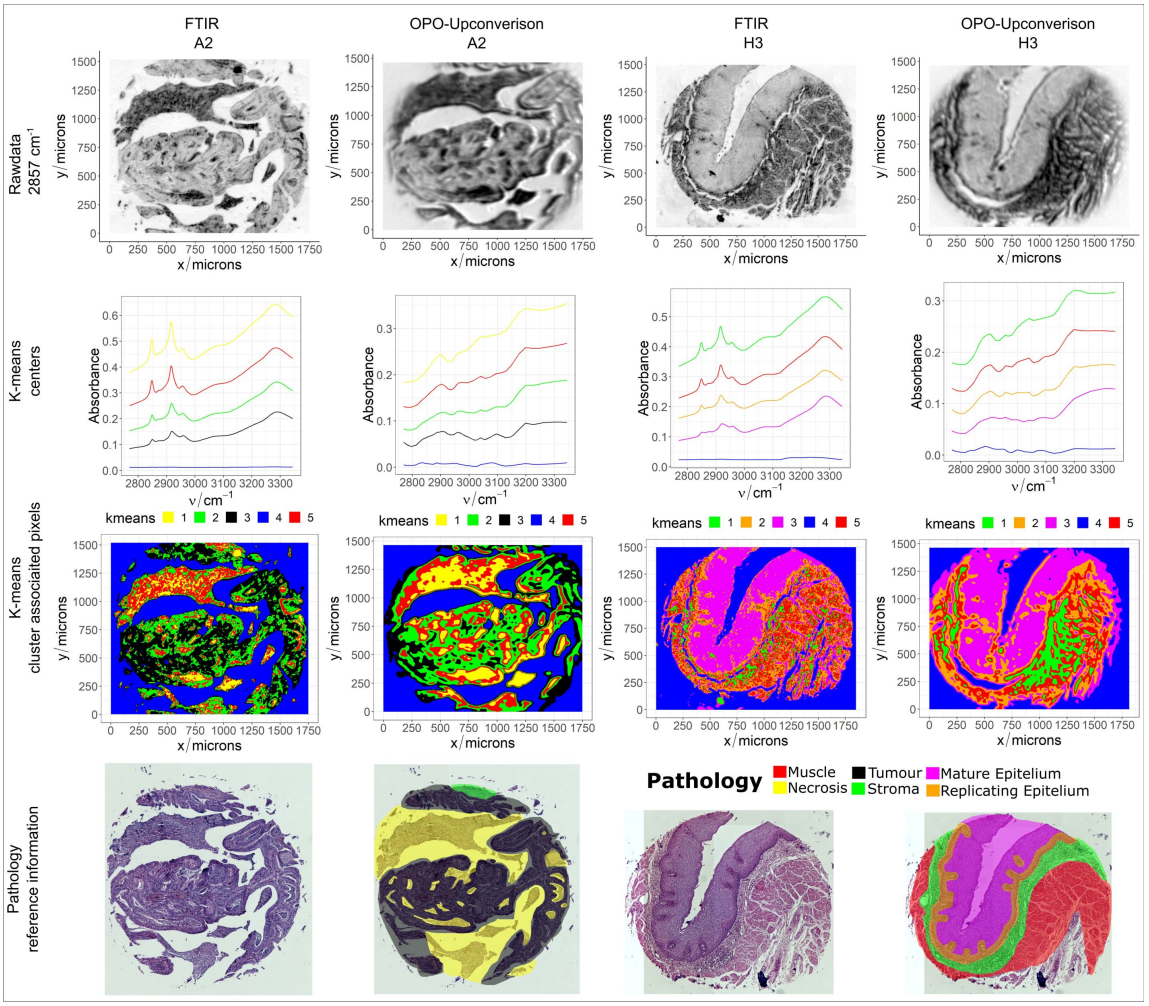

Figure 7.9: *(Top row) Images of the tissue sample acquired using FTIR and upconversion, spectral analysis of the cancerous and healthy tissue sample, based on upconversion imaging and FTIR. (Bottom row) Stained biopsies evaluated by a pathologist and colour-coded according to pathologies annotated, reproduced from [249].*

however, has a high uncertainty for histological sections because it is sensitive to environmental factors, such as humidity and the sectioning procedure. In this specific case, the information can be utilised, as images of the exact same sample are compared, hence figure 7.9 shows non-normalised centre spectra.

In a clinical routine application however, spectra need to be normalised to account for variations in sample thickness (effecting the optical path length in Beer-Lambert type models). Figure 7.10 shows the k-means centres for both systems with the spectra normalised to the 3300 cm^{-1}channel prior to calculating the k-means centres (after clustering however). Normalising to the 3300 cm^{-1}channel, effectively expresses every spectrum relative to it's amide vibration intensity. This expression allows interpreting the relative chemical composition of each pixel in relation to other pixels while discarding the total intensity information. Discarding this information however sacrifices contrast between tumour and other pathologies in the images with the OPO-upconversion setup.

As can be seen in figure 7.9 the regions labelled as tumour are the areas with the lowest total signal. The loss of contrast can be attributed to the fact that the signal difference between the lipid signal (2850 to 3000 cm^{-1}) and the amide peak (starting at 3100 cm^{-1} and being cut of at the high wavenumber end of the spectrum) reaches the same magnitude as the noise and therefore degrading the contrast without the information of total intensity. The separation between the other three pathology classes follows the same pattern between the setups, showcasing that the system delivers hyperspectral imaging capability.

7.6 Conclusion and Outlook

A mid-IR monochromatic imaging system based on upconversion with an enlarged field of view, capable of operating at video frame-rate (40 Hz), without the need for post-processing of the images was presented for the very first time. In the setup, a 2.5 ms exposure time still required an attenuated pump beam to avoid saturation, showing that a potential frame rate of 1 kHz could be realised using a faster silicon CCD camera.

The high efficiency was obtained using a passively synchronised pumping setup. We obtained 64 kpixels in the upconverted images, applying an only 1° of crystal rotation with respect to the tangential phase-matching angle. The FoV was increased by a

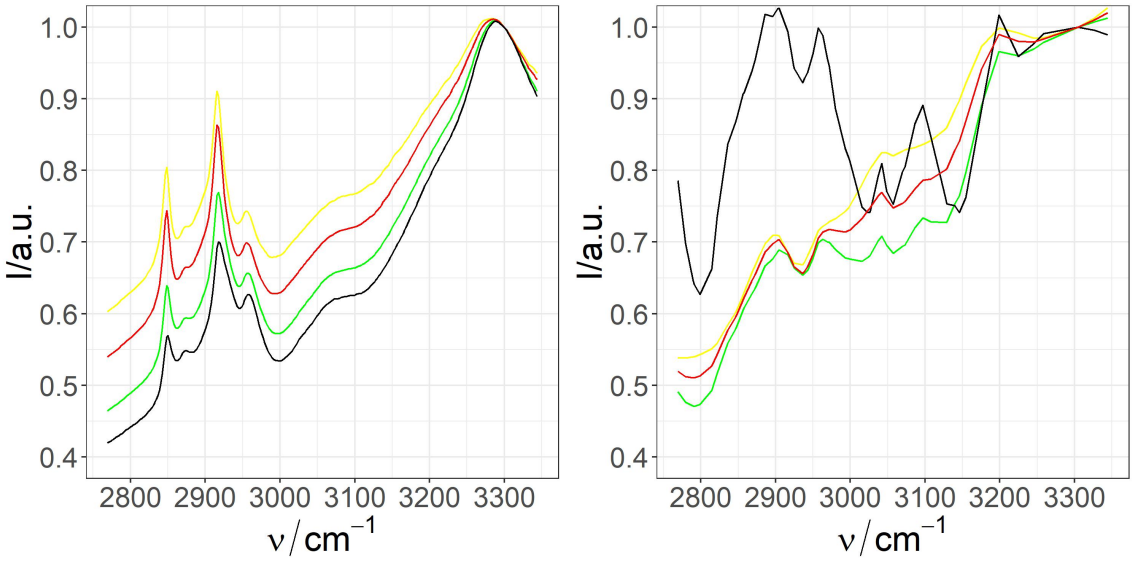

Figure 7.10: *k-means centres (see figure 7.9 2nd row col 1 and 2) for tumour samples. FT-IR left and OPO-upconversion setup. Spectra were normalised to the intensity of the 3300 cm^{-1} channel. Black: Tumour, red: Muscle, green: Stroma, yellow: Necrosis (blue background spectra were discarded).*

factor of 5 compared to a static design, corresponding to an increase of 25 times in the number of pixels. This number can be further increased by applying a larger numerical aperture at the input side, combined with a correspondingly larger crystal rotation angle. Eventually, the angular interrogation of the non-linear crystal for upconversion will be limited by image distortion, originating from refraction at the crystal surfaces. The mid-IR upconversion system operates at room temperature, unlike other low noise mid-IR cameras with single photon detection capability, and with extremely short response time, here demonstrated with 20 ps pulses.

Longer wavelengths could be upconverted using different non-linear crystals such as $AgGaS_2$ (e.g. 5-12 µm). This first application of a MIR OPO-upconversion instrument provided hyperspectral data from human tissue biopsy sections. It was demonstrated that a set of images from 62 wavelengths can enable preliminary, unsupervised clustering of tissue types, with a similar performance to FTIR imaging. Much work regarding stability and reproducibility for upconversion setups remains to be done, however, before this technology can compete with the performance of a state of the art FT-IR imaging system.

8 Discussion & Summary

The experiments discussed in this thesis showcase that the field of infrared imaging undergoes rapid change at the moment. In this chapter the findings are discussed in a broader context. First off all, addressing the new technologies each on their own and finally highlighting potential synergy effects which could result from their combination. After discussing the imaging technology the author wants to address how this technology might be integrated into clinical routines.

8.1 Discussion of Technological Aspects

8.1.1 Impact of New Source Technology on Conventional MIR Imaging

Before 2010 only globars and occasionally synchrotorons were utilised as light sources for MIR imaging systems. Now the portfolio of spectroscopists has increased by QCLs, supercontinuum sources and OPOs. The effects of these sources on hyperspectral imaging are however not fully understood. Deploying these new sources in conventional fashion (MCT or bolometer camera for detection) bares some challenges as discussed before. All of these sources are laser based technologies. Lasers are spatially more coherent and usually polarised in contrast to thermal sources.

This has the consequence that first of all commonly used reflective optics are less favourable to build an imaging systems, as the coherence does not allow for Schwarzschild optics such as Cassegrain objectives to be used. The central obscuration of a Cassegrain is highly dependent on the coherence of the illumination beam as discussed in chapter 2 and figure 2.4.

Furthermore, coherent sources are prone to speckle in wide-field imaging systems. This can be avoided by deploying a point imaging geometry, which on the other hand constrains measurement speed, as it is inherently slower than wide-field imaging.

Another way to avoid speckle is to break the coherence of the laser with a diffuser element as discussed in chapter 7. This however decreases the intensity of the source

and limits acquisition speed as the camera needs to record a full rotation of the diffuser disk.

It is also important to note the difference between tunable monochromatic sources (QCL and OPO) and broadband sources (supercontinuum). In a point scanning geometry, broadband sources are advantageous as they can be combined with a diffraction element to provide spectral resolution measuring a full spectrum with each acquisition. In a wide-field setup monochromatic sources can be utilised if the relevant information can be extracted from a few specific frequencies instead of a full MIR spectrum. If a full spectrum is required, a broadband source is potentially still favourable.

8.1.2 Impact of New MIR Detection Technology on Imaging

Considering new upconversion type cameras as discussed in chapter 7 design constraints for a MIR imaging systems change compared to a conventional setting as discussed in subsection 8.1.1. First of all the non-linear crystal imposes further wavelength constraints as it needs to be transmissive for both the MIR signal and the visible or NIR pump laser. To this date no crystal exits which is transmissive throughout the whole MIR, while having a high non-linear refractive index. This work utilised a bulk lithium niobate crystal enabling upconversion of MIR photons between 2 and 4.5 µm. Other bulk crystals, e.g. $AgGaS_2$, extend beyond 4.5 µm, thus affirming the generic nature of the proposed concept and enabling further extension of the upconversion imaging into the 5 to 15 µm range.

Designing an imaging system then depends on the sources as the angle dependency of the upconversion (see figure 2.2) process needs to be taken into account. Building a wide-field imaging system, a monochromatic source would be favourable, as a system could be built utilising ‘tangential phase-matching‘ as discussed in chapter 7 getting the spectral resolution from the source. This scheme, however, can not easily be used with a broadband source as the images would consist of several rings containing different frequencies (see figure 7.4) and therefore can not be integrated into a single camera frame without losing the spectral information.

An alternative to the approach described above, would be to deploy a broadband source in point scanning geometry coupled to an upconversion spectrometer (as described by *Tidemand-Lichtenberg et al.* [78] for example) which to the authors knowledge has not been done to this date.

Deploying a monochromatic source in combination with upconversion detection in point scanning geometry as described by *Tseng et al.* [264] does not provide any added value compared to a Peltier cooled single element MCT[1]. The upconversion detector does have a much higher technical complexity and to this date does not beat the MCT in noise equivalent power and also is not likely to be significantly cheaper either.

A different added benefit of upconversion detection however could be gained if a visible or NIR camera could be put to dual use in a system providing VIS/NIR capability together with MIR imaging. Furthermore, there is also the possibility to use the pump laser to excite Raman signals, as well.

8.2 Discussion of Clinical Aspects

Putting the clinical findings into perspective the major finding of the thesis is the conclusion, that when working with paraffin embedded samples, it is clearly favourable to remove the paraffin, but not strictly necessary. This is a constant point of debate in the community.

8.2.1 Statistical Aspects

A major concern regarding the results is the statistical validity as only very few samples have been available to build classification models from. Furthermore, not all clinically relevant features for addressing adenocarcinomas were present in the dataset. The dataset consisted of samples harvested from oesophageal resections and did not contain areas with Barrett‘s oesophagus or dysplasia. This limitation of the sample set was attributed to the fact that access to the different imaging systems was limited and therefore one sample was chosen to focus on comparing the technical aspects based on the data obtained from that sample. It remains an open question whether MIR imaging is a suitable tool to differentiate between all the possible clinical cases occurring in oesophageal tissue. Addressing this question comprehensively however is a project far beyond the resources available within a single PhD project if a comparison between several techniques is aspired.

[1] The paper itself compares against a liquid nitrogen cooled MCT and argues that the added value is in making the liquid nitrogen redundant, which is only valid for cameras and not to single element detectors.

The 40 samples investigated in this thesis are not representative for larger populations and even though a resampling strategy to minimise bias in the classification models was developed, there are factors which can not be represented by resampling. Therefore, it is sensible to assume that the models obtained are over optimistic from an information theory point of view. The problem lies in the fact that the data space has a very high dimensionality compared to the number of samples available for training [265]. This has partially been addressed by the fact that the actual learning has been performed on the data subspace projected by the PLS. The PLS decreases the dimensions (different frequencies measured) from hundreds to 10 which decreases the magnitude of the problem but still the sample size is too small as a typical rules-of-thumb recommends at least 5 samples per dimension [266].

In order to build a classifier to asses oesophageal samples based on the Vienna classification [196] (see section 4.3.2 and table 4.1), a data set is needed containing at least 100 statistically independent samples per group [248] for testing the classifier alone. Assuming the same amount of samples is required to train a classifier, this results in a minimum of 1000 samples (1600 if subgroups should be taken into account) required to prove with statistical confidence whether MIR imaging is a tool suitable to support pathologists in their decision making. Measuring such an amount of samples is however not as straight forward as it seems as such an experiment is likely to reveal technical challenges (discussed in section 8.2.2) which have been irrelevant for smaller models.

8.2.2 Technical Aspects

As discussed in section 8.2.1, in order to prove that MIR hyperspectral imaging could be useful for histopathological applications an experiment on a much larger scale measuring thousands of samples needs to be conducted. Technology is not the major limitation here, since such an experiment could be conducted on state of the art FT-IR microscopes. FT-IRs are producing high quality images in terms of spectral quality. The main limitations in data acquisition on FT-IRs are spatial resolution and measurement speed. QCL systems can address these speed constraints and potentially also deliver higher spatial resolution. FT-IRs in theory could also deliver higher resolution then demonstrated in this thesis. All the work on tissue samples however has been conducted with an effective pixel size configuration of 5.5 µm although an effective pixel size of 0.66 µm is achievable as demonstrated in chapter 5 with the

setup. The problem with that configuration however, is that the globar is too weak a source to deliver acceptable SNR in the images in a practical time.

The question which spatial resolution is required to build a good classifier however, still remains unanswered. A very small study by *Lloyd et al.* [267] found that there seems to be an effect comparing performance between a setup with 1.1 µm pixel size to 5.5 µm but the data set was too small to be significant. In this work there was no clear difference found relating to spatial resolution between the QCL point scanning images recorded compared to the FT-IR images (see figure 6.3).

A further challenge for a large scale experiment is the reproducibility of measurements across individual systems and over time. This is a very well known problem with Raman hyperspectral mapping systems [268]. So far, this has not been a major issue for MIR imaging. Most experiments were conducted on FT-IR systems, which are referenced against Helium-Neon laser. Typically tey are very stable, resulting in the FT-IR systems calibrations being stable as well. Moving away from those, towards QCL or upconversion detection, would introduce a various moving components into the systems which are difficult to monitor whether they stay in alignment or drift and cause various different artefacts as reported occuring in Raman systems [268].

Assuming MIR can be used to aid decision making in pathology, in order to be useful in clinical routines, a MIR system must be integratable into current workflows. Therefore it must be fully automated and has to be able to be operated by a technician without expertise in complicated optical setups.

Ideally, those workflows would not utilise CaF_2 or BaF_2 substrates as they are expensive and very fragile. Alternatives are either low-e slides for transflection imaging, silicon substrate for QCL imaging or even standard glass histological slides for high wavenumber imaging.

8.3 Summary

This work has demonstrated the use of a new transmission resolution test target to characterise MIR imaging systems in chapter 5. The new chart enables transmission imaging in contrast to the conventional chromium on glass charts.

Chapter 6 discussed paraffin influencing samples to be measured with MIR imagining systems. Spectral contributions of paraffin are correctable using EMSC models like

the one developed in this thesis. The EMSC approach developed here deploys an correction estimating paraffin spectral contributions from the paraffin surrounding the sample instead of relying on library spectra, making it less sensitive to variations in the paraffin.

This correction however requires more data points per spectrum to be measured compared to chemically dewaxed samples. This is not a problem with conventional FT-IRs as they always acquire the full spectrum over the entire MIR wavelength range. If discrete frequency set-ups are to be used in the future, they are required to utilise fewer wavelengths, in order to gain a speed advantage over FTIRs. In this case accounting for paraffin via an EMSC model requires measuring more frequencies and therefore more measurement time making it less favourable compared to chemical paraffin removal.

In chapter 7 the first ever experiment combining an MIR-OPO providing 3-5 µm wavelength radiation, with an upconversion detection scheme was discussed. This approach is particularly interesting for clinical routines as it would allow working with standard glass clinical histology slides, which is not possible via fingerprint (6-12 µm) MIR imaging. This work demonstrated that those set-ups are in principle suitable for MIR imaging of biological materials. Yet much work needs to be done to improve the technology, to make upconversion on a par with state of the art FT-IR systems.

8.4 Conclusion

In conclusion this thesis presented that there are numerous MIR techniques evolving at the moment. All of these techniques have proven to have advantages over particular other techniques but none of them seems to outperform the conventional techniques in all aspects to this date.

This work demonstrated the advancement and evaluation of mathematical deparaffination in comparison to chemical dewaxing. The direct comparison of dewaxed and electronically deparaffinated samples highlights that chemical dewaxing is favourable if the experiment allows for it.

With regard to novel technologies the use of QCLs, supercontinuum sources and upconversion detection have been explored in different proof of concept experiments. From those it can be concluded that upconversion and supercontinuum are still not mature enough to be used in a routine setting but show great potential to reach that

point in the future. QCLs however are technologically more mature already and offer a potential to improve data aquistion speeds drastically compared to conventional FTIR systems.

8.5 Outlook

8.5.1 Providing Clinical Evidence

As discussed previously, the data set produced in this work is to small to be significant from a clinical perspective. In order to evaluate the potential of MIR imaging for clinical use, a study with over 1000 patients is needed. Such a study could potentially be done on carefully selected archive tissues.

Despite being relatively slow in acquisition speed, FT-IRs would still be the systems favoured for this approach as they tend to provide the best data quality in terms of SNR and spectral coverage. Having a data set allowing statistically significant analysis would furthermore enable to explore to which extend spectral coverage and SNR can be traded for faster acquisition.

As discussed in section 3.5 there are several strategies which can be deployed to estimate which frequencies need to be measured to achieve maximum discrimination power while substantially decreasing overall spectral coverage.

8.5.2 Photothermal Imaging

Another technique with the potential to dramatically change the field of MIR microspectroscopic imaging is photothermal spectroscopy. This technique only starts to emerge to the date this thesis is written, nevertheless the author sees great potential in this being applied for clinical MIR imaging in the future.

The general idea of probing photothermal effects is well established in combination with atomic force microscopy [16]. As conventional MIR transmission and transflection imaging is inherently limited by the diffraction limit of the infrared beam to scan the sample, these techniques are limited to micrometer resolution in the best case. Photothermal imaging is a detection technique which circumvents the diffraction limit of the MIR beam by not measuring its depletion, but instead probing the sample with a visible beam at the same time to sense the transient photothermal effect induced by

the absorption of MIR photons. Therefore, it is diffraction limited only by the visible probing beam achieving sub-micron resolution [269]. This concept has now been extended to also be applicable to wide-field imaging [270]. Photothermal microscopy therefore also has great potential as a tool for clinical application having the significant advantage that it can be applied to thick samples and is not dependent on CaF_2 substrates and liquid nitrogen cooled detectors.

8.5.3 Authors Opinion

From the personal perspective of the author much work remains to be done to demonstrate whether MIR is a good tool for histopathology. Having spent over five years in that research sector the community of scientists appears quite homogeneous an while titles of talks changed, the conclusions did not change much during those 5 years: ‘more samples are needed and closer involvement of clinicians‘. The key challenge appears to be of less of scientific nature rather than ‘logistic‘. No research group seems to acquire enough samples for truly meaningful experiments (1000 patients and more).

It seems that clinicians apart from a very few exceptions, see vibrational (MIR and Raman) imaging techniques as a toy of a group of people with the metaphorical hammer looking for a nail. In order to change this perspective, it is necessary to demonstrate significant added value of these techniques, compared to the standard clinical workflows such as H&E staining.

It is the authors impression that large parts of the community see machine learning and chemometrics as a magic which will solve their problems if they just acquire enough data. In order to overcome this, closer collaboration with statisticians is urgently required, to prevent people from doing experiments which from a statistical perspective were bound to be meaningless from the start.

The author hopes that the formation of the International Society for Clinical Spectroscopy (CLIRSPEC) will direct the community towards achieving these goals addressing the authors concerns.

Supporting Information QCL Imaging

1 Setup

This document has been generated using R and Rstudio in markdown. Grey blocks depict Rcode to illustrate how calculations were performed. Please note that much of the code could have been written more efficiently, however the author decided on purpose to present it in a way that is optimised for readability.

The first block of code here shows the R-packages used.

```
Packages <- c("hyperSpec","FTIR","gtools","plyr", "dplyr",
              "ggplot2","gridExtra", "matrixStats", "caret",
              "knitr", "MASS", "pls")

lapply(Packages, library, character.only = TRUE)
```

Loading the images of the first sample, labelled A1 on the TMA: https://www.biomax.us/tissue-arrays/Esophagus/ES8011a.

Obtained on the different instruments as described in Materials and Methods.

```
data = list()
data[["Agilent QCL Dewaxed"]] <-
  readRDS("F:/Data/QCL_Paper_supporting_information/Agilent_QCL_dewaxed_rawdata.RDS")
data[["Agilent QCL paraffin embedded"]] <-
  readRDS("F:/Data/QCL_Paper_supporting_information/Agilent_QCL_rawdata.RDS")
data[["Bhargava QCL Dewaxed"]] <-
  readRDS("F:/Data/QCL_Paper_supporting_information/Bhargava_QCL_dewaxed_rawdata.RDS")
data[["Bhargava QCL paraffin embedded"]] <-
  readRDS("F:/Data/QCL_Paper_supporting_information/Bhargava_QCL_rawdata.RDS")
data[["FTIR Dewaxed"]] <-
  readRDS("F:/Data/QCL_Paper_supporting_information/FTIR_dewaxed_rawdata.RDS")
data[["FTIR paraffin embedded"]] <-
  readRDS("F:/Data/QCL_Paper_supporting_information/FTIR_rawdata.RDS")
```

2 Raw Data

Define a function to plot the data in the ggplot2 framework.

```
PlotIMG <- function(Image, title) {

p <- qplotmap(Image) +
      scale_fill_gradient(low = "black", high = "white")+
      theme_classic() +
      theme(legend.position = 'none',
            plot.background = element_rect(fill = "transparent", colour = NA),
            text = element_text (size = 14)
            )+
  ggtitle(title)

p
}

grobs <-  list()

for (i in seq_along(data)) {
  grobs[[i]] <- PlotIMG(data[[i]], names(data)[i])
}

grid.arrange(grobs = grobs,
             ncol=2)
```

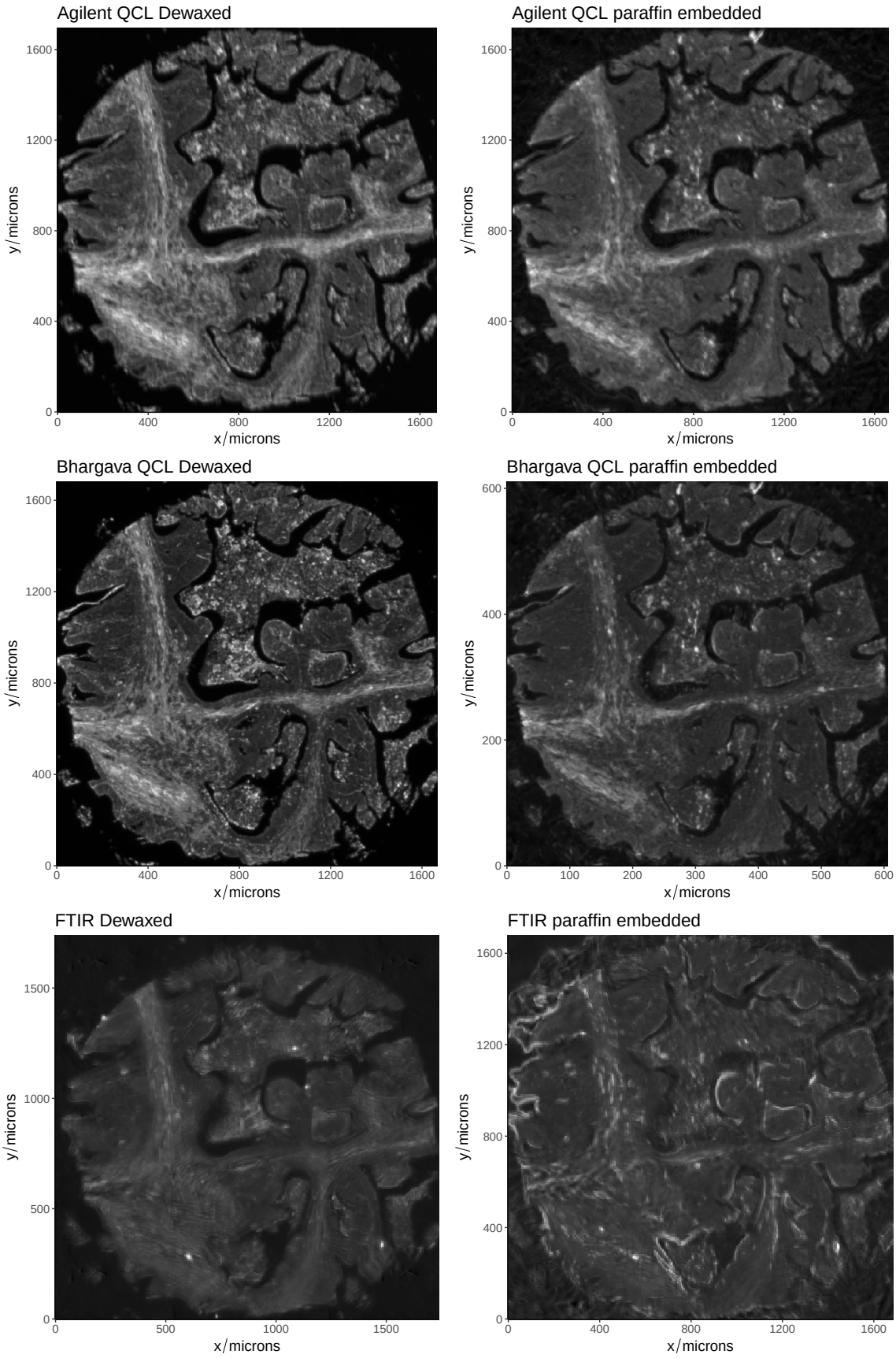
Agilent QCL Dewaxed
Agilent QCL paraffin embedded
Bhargava QCL Dewaxed
Bhargava QCL paraffin embedded
FTIR Dewaxed
FTIR paraffin embedded
y/microns
x/microns

3 Estimating Signal to Noise Ratios

Signal-to-noise ratio (SNR) is a common metric for image quality. There are various ways to calculate the SNR. For imaging, noise generally is estimated as the standard deviation of the background of the image. In this specific case, we have images of oesophageal tissue (the object) that also contain empty areas surrounding the tissue (the background).

In order to differentiate between object and background, we use k-means clustering and estimate the background as the cluster whose centroid has the lowest intensity at the channel closest to the Amide-I peak maximum (1650 cm-1). The procedure is shown for the FTIR data in the following:

```
spc <- data[["FTIR Dewaxed"]]

k=8 #number of clusters to be computed
set.seed(32) #fix randomisation seed
cluster =  kmeans(spc[[]],
                  centers = k,
                  iter.max = 100
  )

means = decomposition(spc, cluster$centers, wl(spc))
spc$kmeans = as.factor(cluster$cluster)

centroidPlot <- qplotspc(means,
                         mapping =  aes( x = .wavelength,
                                         y = spc,
                                         colour = .rownames,
                                         group = .rownames )
                          )+
  scale_color_manual(values =rainbow(k))+
  theme_bw() +
  theme(plot.background = element_rect(fill = "transparent",
                                       colour = NA),
        legend.position = 'none',
        legend.background = element_blank(),
        text = element_text (size = 14)) +
  scale_x_continuous(breaks=seq(1000, 1800, by = 200))+
  scale_y_continuous(breaks = seq(0, 0.6, by = 0.1))

clusterMap <- qplotmap(spc,
```

```
                        mapping = aes_string(x = "x",
                                             y = "y",
                                             fill = "kmeans")) +
                scale_fill_manual ("kmeans",
                                   values = rainbow(k),
                                   guide = guide_legend(title = "Cluster")
                                   ) +
                theme_bw()+
                theme(plot.background = element_rect(fill = "transparent",
                                                     colour = NA),
                      legend.position = 'top',
                      legend.background = element_blank(),
                      text = element_text (size = 14))
grid.arrange(
  clusterMap,
  centroidPlot,
  ncol=2,
  top = textGrob(paste0("K-means to separate sample and background"),
                 gp=gpar(fontsize=20,font=3)),
  bottom = textGrob(paste0("Cluster ", which.min(means[[,,1650]]),
                           " chosen to represent background"),
                    gp=gpar(fontsize=12,font=3))
  )
```

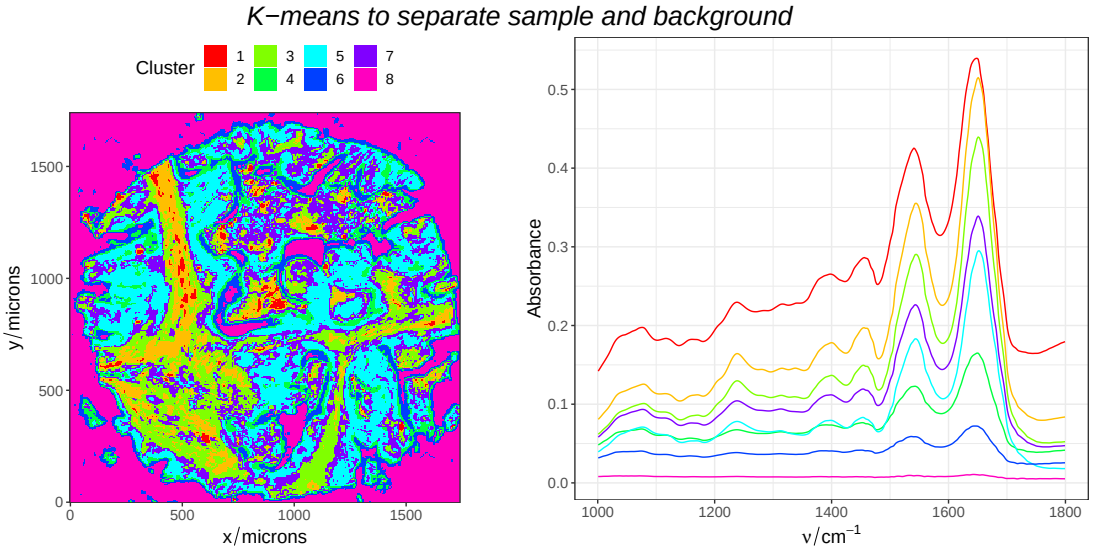

Cluster 8 chosen to represent background

```
bg <- spc[spc$kmeans ==   which.min(means[[,,1650]])]
signal <- spc[!spc$kmeans ==   which.min(means[[,,1650]])]
```

The signal-to-noise ratio for every channel can now be obtained by deciding the mean value of the absorption intensity for each channel by the standard deviation of the background for that channel.

```
estSNR = function(spc) {

k=8 #number of clusters to be computed
set.seed(32) #fix randomisation seed

cluster =  kmeans(spc[[]],
                  centers = k,
                  iter.max = 100)

means = decomposition(spc, cluster$centers, wl(spc))
spc$kmeans = as.factor(cluster$cluster)

bg <- spc[spc$kmeans ==   which.min(means[[,,1650]])]
signal <- spc[!spc$kmeans ==   which.min(means[[,,1650]])]

bgSds <- mean(bg)
bgSds[[]] <- colSds(bg[[]])

SNR <- mean(signal) / bgSds
SNR
}
```

4 Paraffin Correction Algorithm

In order to correct for the spectral contributions of the paraffin, its spectral profile is needed. In previous approaches, those profiles were obtained from data recorded separately and assumed to be invariant from the paraffin in the object. As this invariance cannot be demonstrated and is likely to play a role, in the approach used here the paraffin profiles are obtained from the areas of the image that do not contain the actual sample. This approach is especially practical for processing tissue microarray data, as measuring those always involves measuring paraffin areas as well. It might be less practical for processing data from entire histological sections as obtained in hospital routines.

In order to separate paraffin from sample areas, k-means clustering is used in the same fashion as described above for calculating the SNR.

```
spc = data[["FTIR paraffin embedded"]]

k=8 #number of clusters to be computed
set.seed(32) #fix randomisation seed

cluster =  kmeans(spc[[]],
                  centers = k,
                  iter.max = 100
  )

means = decomposition(spc, cluster$centers, wl(spc))
spc$kmeans = as.factor(cluster$cluster)

p1 <-  qplotmap(spc,
                mapping = aes_string(x = "x",
                                     y = "y",
                                     fill = "kmeans")) +
    scale_fill_manual ("kmeans",
                       values = rainbow(k),
                       guide = guide_legend(title = "Cluster")
                       )+
  theme_bw()+
  theme(plot.background = element_rect(fill = "transparent",
                                       colour = NA),
        legend.position = 'top',
        legend.background = element_blank(),
        text = element_text (size = 14))

p2 <- qplotspc(means,
               mapping =  aes( x = .wavelength,
                               y = spc,
                               colour = .rownames,
                               group = .rownames)
               )+
  scale_color_manual(values =rainbow(k))+
  theme_bw() +
  theme(plot.background = element_rect(fill = "transparent",
                                       colour = NA),
        legend.position = 'none',
        legend.background = element_blank(),
        text = element_text (size = 14)) +
  scale_x_continuous(breaks=seq(1000, 1800, by = 200))+
  scale_y_continuous(breaks = seq(0, 2, by = 0.25))
```

```
grid.arrange(p1,
             p2,
             nrow = 1,
             top = textGrob(paste0("K-means Results"),
                            gp=gpar(fontsize=20,font=3)),
             bottom = textGrob(paste0("Cluster ", which.min(means[[,,1650]]),
                                      " chosen to represent paraffin",
                                      " areas as modeling reference"),
                               gp=gpar(fontsize=12,font=3)
                               )
             )
```

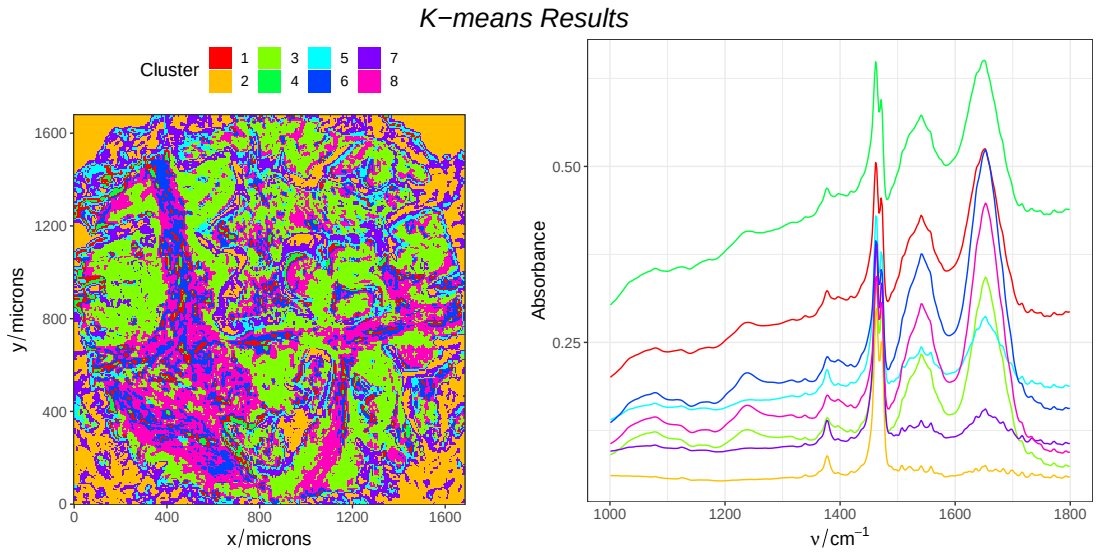

Cluster 2 chosen to represent paraffin areas as modeling reference

```
paraffin <- spc[spc$kmeans ==   which.min(means[[,,1650]])]
sample <- spc[!spc$kmeans ==   which.min(means[[,,1650]])]
```

The object containing the spectra representing the paraffin background are now fed into a principal component analysis to identify the main variations.

```
pca_model <- prcomp(paraffin[[]], center = FALSE)
```

Those spectral variations can be assumed to be independent on the sample and therefore will be treated as perturbations of the 'interesting' spectral components originating from pathology. The versions of the EMSC used in the literature and described before suggest using the first n loadings, where n is a parameter of choice that is never adequately defined.

Here the number of loadings to be used for modelling the spectral variation is chosen based on two criteria. First the total variance covered by each principal component (PC) is assessed (see figure below). In this case the most of the variance is covered in PC1, especially given that the PCA was performed on non-mean centred data. Investigating the variance alone however does not help in estimating the number of relevant PCs. It is possible to argue for anything between 10 and 15 PCs depending on the sample complexity.

```
qplot(x = 1:20, y = (pca_model$sdev^2 / sum(pca_model$sdev^2))[1:20]) +
  scale_y_log10(breaks= c(1, 0.1, 0.001, 0.0001))+
  ylab(expression(log10(sigma^2)))+
  xlab("Principal Component")
```

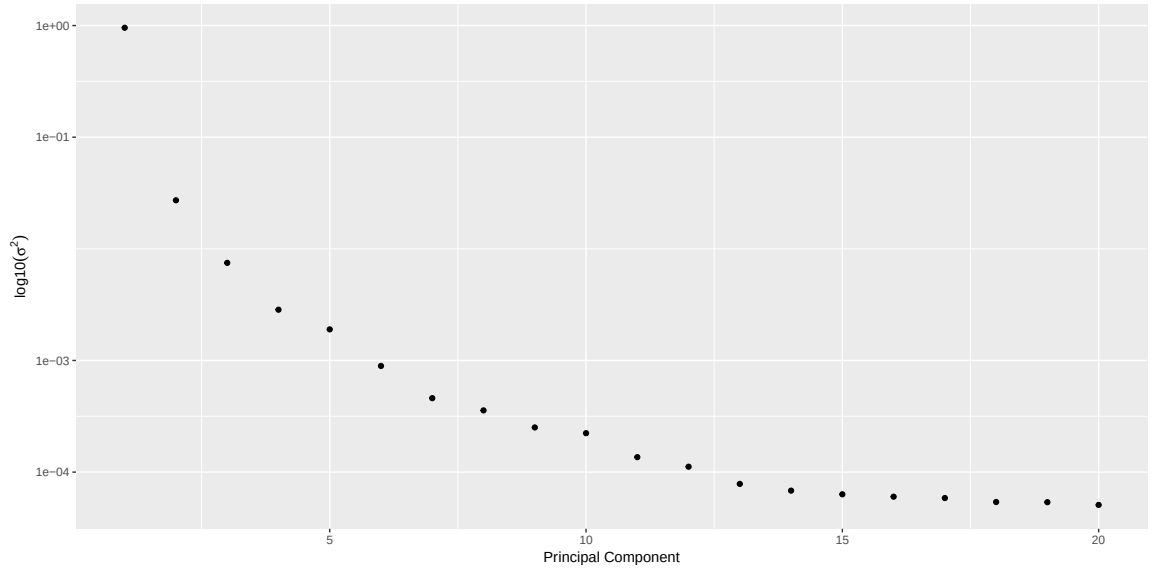

In addition to the variance explained, the structure of the PCs, also referred to as loadings, can be utilized to judge their importance. In the figure below, the first 20 loadings are depicted.

```
loadings_all <- decomposition (paraffin,
                               t (pca_model$rotation),
                               scores = FALSE)
n.plot = 20
loadings <- loadings_all[1:n.plot]
loadings$PC <- 1:n.plot
loadings$PC <- as.factor(loadings$PC)
levels(loadings$PC) <- rownames(loadings)

qplotspc(loadings[1:n.plot],
```

```
        mapping = aes (x = .wavelength,
                       y = spc,
                       group = .rownames),
        spc.nmax = n.plot
       )+
  facet_wrap (. ~ PC,
              ncol = 2,
              labeller = labeller(),
              scales ="free") +
  xlab( expression(Wavenumbers / cm^-1)) +
  ylab(expression(Intensity/a.u.))
```

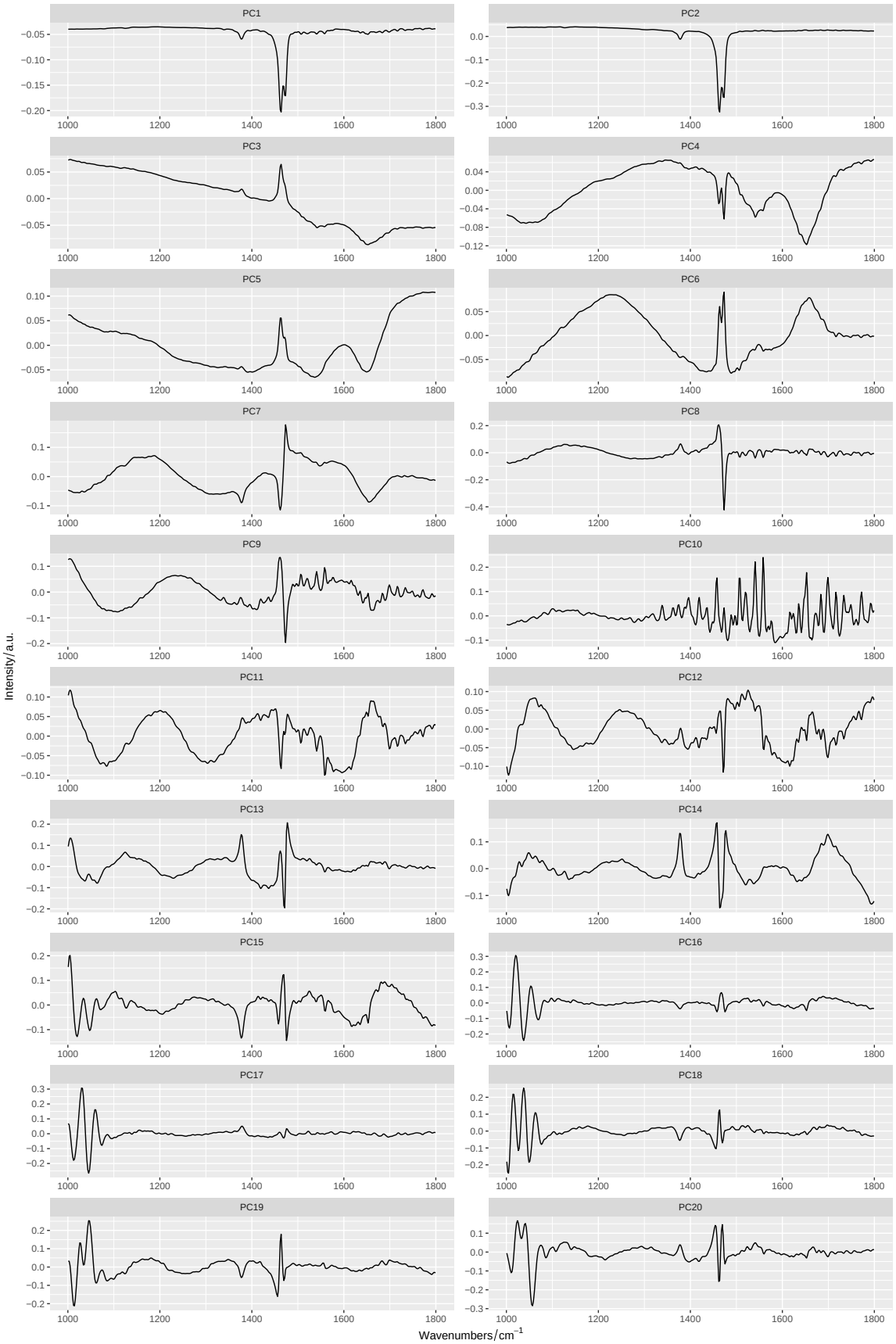
PC1
PC2
PC3
PC4
PC5
PC6
PC7
PC8
PC9
PC10
PC11
PC12
PC13
PC14
PC15
PC16
PC17
PC18
PC19
PC20
Intensity/a.u.
Wavenumbers/cm^{-1}

The first two loadings can be interpreted as the paraffin IR spectrum, loading 3 to 9 show baseline effects (3-6) and paraffin peak position shifts (7-9). Loading 10 is clearly recognisable as a water vapour spectrum. The loadings above number 10 however are more difficult to interpret, whilst they explain less and less variance in the data, and therefore they are not considered any further.

If the loadings would be used for spectral decompositions as depicted above, there would be the issue that spectra could become negative, as the PCA does not favour axis directions. If the loadings shall be used in a non-negative decomposition, this issue needs to be addressed. In order to do so, the loadings can simply be inverted if they represent the inverse of a spectrum as observable in PC 1 and 2. Therefore, each loading is checked in that it is established whether its absolute maximum is a positive or negative value. In case of a negative value, the loading can be inverted by multiplying the loading vector by a factor -1. The author tried to circumvent this problem by using a non-negative matrix factorisation (NMF) instead of the PCA, but unfortunately its R implementation of the NMF package cannot handle the volume of data in this project in a practical fashion (computation times of more than 17h for a single image).

```
  flip_loadings <- function(object){
    flip_operator <- (abs(rowMins(object[[]])) < abs(rowMaxs(object[[]])))*2 -1
    # if pos  =1; if neg = -1
    object * flip_operator
  }

loadings <- flip_loadings(loadings)
```

In summary, the first 10 loadings of the PCA were selected and inverted in case of negativity. In order to use these to correct the paraffin contributions in the sample spectra, these loadings can be subtracted. This subtraction however needs to be performed in a weighted fashion as it is unknown how strong these contributions are in each individual spectrum. The weights can be estimated via a linear decomposition or in this case a non-negative linear least squares decomposition, as an ordinary least squares decomposition would allow for negative spectra.

As a least squares fit however fits the entire spectrum, in order for this to work reliably, a reference spectrum is needed as well. A spectrum obtained from fresh frozen cut oesophageal tissue is used in this case and visualised in the figure below. It is important to note here that this reference spectrum needs to be the same for

all samples in a study as otherwise the reference spectrum used could introduce an artificial bias to classification models.

```
load (file =paste0("D:/OneDrive - University of Exeter",
                   "/PhD/2017_01_26_Oesophagus_TMAs/tmp/tissue.Rdata"))

#spline spectrum to same wavenumbers as sample.
tissue <-  spc.loess(tissue,newx = wl(spc))

qplotspc(tissue)+
  ggtitle("Tissue Reference Spectrum")
```

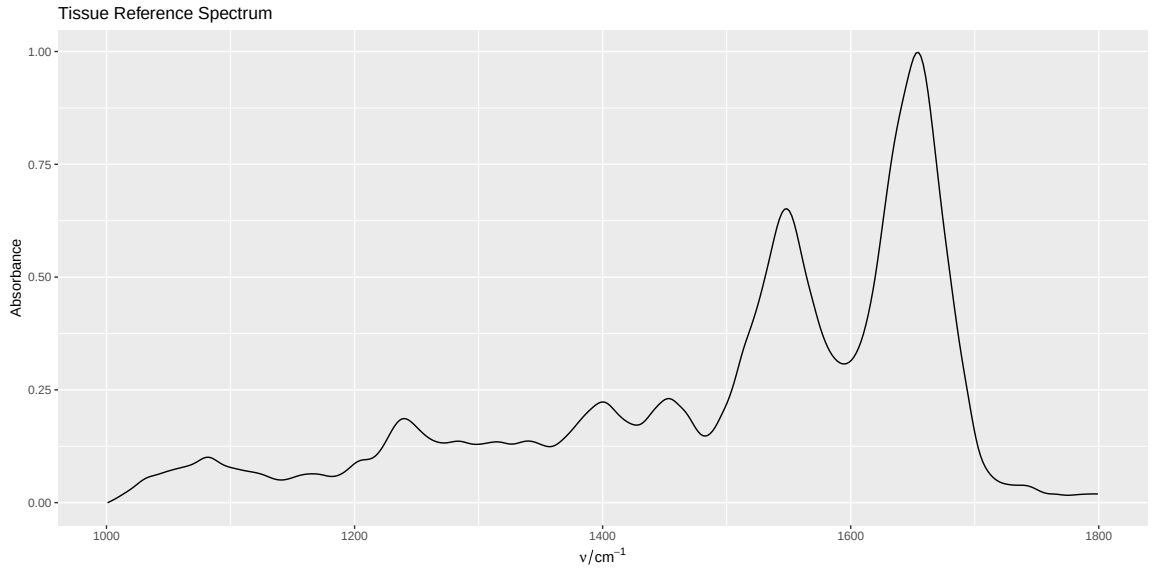

The components for correction are then normalised as visualised below. Furthermore, we introduce two more components for fitting a 0th and 1st order baseline via a Vandermonde matrix.

```
#renaming hacks to make the plot work correctly
loadings$PC <- as.character(loadings$PC)
tissue$PC <- "Tissue Reference"

#normalise everyting to  0 to 1 range
estimates <- normalize01(flip_loadings(loadings[1:10]))
#baseline fitting
ref <- vanderMonde (estimates,
                    1,
                    normalize.wl = normalize01)
ref$PC <- c("0th order Baseline", "1st order Baseline")
ref <- hyperSpec::collapse(tissue, ref, estimates)
```

```
ref$PC <- factor(ref$PC, ref$PC)

qplotspc(ref,
         mapping = aes (x = .wavelength,
                        y = spc,
                        group = .rownames),
         spc.nmax = 20
         )+
  facet_wrap ( ~ PC  , ncol = 2, labeller = labeller())+
  xlab( expression(Wavenumbers / cm^-1)) +
  ylab(expression(Intensity/a.u.))
```

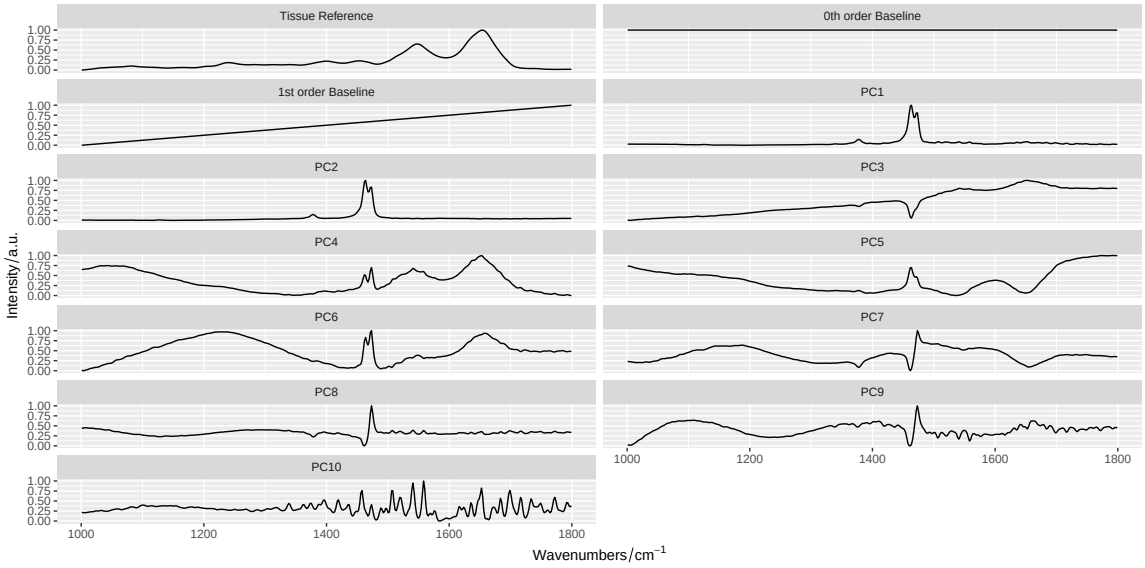

The components are then used to compute the non-negative least squares decomposition (NNLS) of the data using `fcnnls` from the `NMF` package. This seems to be the fastest implementation for the non-negative least squares method in R.

```
#actual EMSC part1
scores <- fcnnls(t(ref[[]]), t(spc[[]]))
#the NMF package works on column representations
#whereas hyperSpec works on collums, thus the mutliple use of t()
scores <- t(scores$x)
```

The scores obtained this way are an estimate for the magnitude of each of the perturbations modelled by the EMSC. The total of these perturbations is subtracted as the sum of each loading multiplied by its score obtained from the NNLS, only keeping the modelled reference and the residuals (which contain the actually relevant information).

```
#actual EMSC part 2
spc[[]] <-  spc[[]] -  scores[,2:13, drop = FALSE] %*% ref[[2:13,, drop = FALSE]]
```

After correction of the paraffin contributions, k-means clustering can again be used to identify and then discard all areas that can be considered as 'voids', as they should ideally not contain anything else apart from paraffin (whose spectral contributions were already eliminated).

```
k=5 #number of clusters to be computed
set.seed(32) #fix randomisation seed
cluster =  kmeans(spc[[]],
                  centers = k,
                  iter.max = 100
  )

means = decomposition(spc, cluster$centers, wl(spc))
spc$kmeans = as.factor(cluster$cluster)

p1 <-  qplotmap(spc, mapping = aes_string(x = "x",
                                          y = "y",
                                          fill = "kmeans")) +
    scale_fill_manual ("kmeans",
                       values = rainbow(k),
                       guide = guide_legend(title = "Cluster")
  ) +
  theme_bw()+
  theme(plot.background = element_rect(fill = "transparent",
                                       colour = NA),
        legend.position = 'top',
        legend.background = element_blank(),
        text = element_text (size = 14))

p2 <- qplotspc(means, mapping =  aes( x = .wavelength,
                                  y = spc,
                                  colour = .rownames,
                                  group = .rownames
)
)+
scale_color_manual(values =rainbow(k))+
  theme_bw() +
  theme(plot.background = element_rect(fill = "transparent"
                                       ,colour = NA),
        legend.position = 'none',
```

```
        legend.background = element_blank(),
        text = element_text (size = 14)) +
  scale_x_continuous(breaks=seq(1000, 1800, by = 200))+
  scale_y_continuous(breaks = seq(0, 2, by = 0.25))

grid.arrange(p1,
             p2,
             nrow = 1,
             top = textGrob(paste0("K-means Results"),
                            gp=gpar(fontsize=20,font=3)),
             bottom = textGrob(paste0("Cluster ", which.min(means[[,,1650]]),
                                      " chosen to represent empty",
                                      " areas to be deleted"),
                               gp=gpar(fontsize=12,font=3)
                               )
             )
```

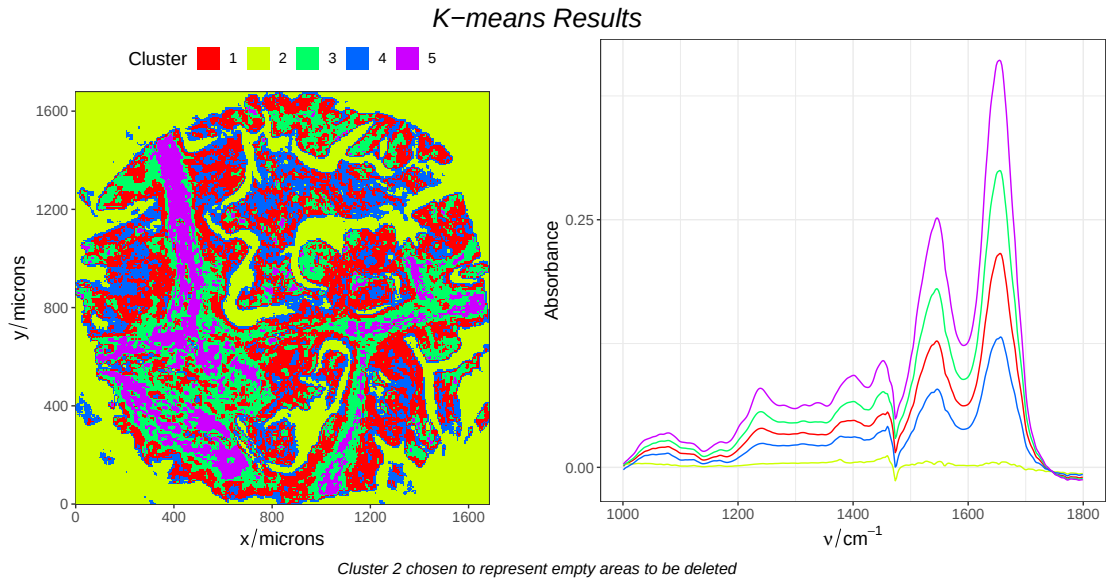

As depicted above, the 'void' areas can now be removed and only the spectra containing the actual sample are used for classifications of histopathological features.

5 Classification Routines

5.1 Validation Datasets

In order to validate the trained models, a scheme to mix cross validation and bootstrapping was developed. The dataset is highly imbalanced with only 5 healthy patients

versus 35 tumour patients. In order to build balanced models, the dataset is split into 7 sets of 5 tumour patients. For each patient, a random sample is drawn. These samples are then matched with 5 samples drawn with replacement from the 10 samples of the 5 healthy patients.

```
set.idx  <- list()

for (i in 1:7) {
#selecting samples form tumour patients
  idx <-  seq(1, 70, by= 14)+(2*i-1) - sample(0:1,5, replace = TRUE)
#adding 5 samples from healthy biopsies
  set.idx[[i]] <- c(idx, sample(71:80, 5, replace = TRUE))
}

#load the actual draw used in the dissertation
set.idx  <- readRDS("F:/Data/CV_Indexes.RDS")

cores <- expand.grid(LETTERS[1:8],
                     formatC(1:10,
                             width=2,
                             format="d",flag="0"),
                     stringsAsFactors = FALSE
                     )
  cores <- cores[order(cores$Var1),]

  core <- c()
  for (i in 1:80) {
  core[i] <- paste0(cores$Var1[i], cores$Var2[i])
  }

SETS <- matrix("empty",
               nrow = 7,
               ncol = 10,
               dimnames = list(c("Set 1", "Set 2", "Set 3", "Set 4",
                                 "Set 5", "Set 6", "Set 7"),
                               c("Tumour 1", "Tumour 2", "Tumour 3",
                                 "Tumour 4", "Tumour 5", "Healthy 1",
                                 "Healthy 2", "Healthy 3", "Healthy 4",
                                 "Healthy 5")
                               )
               )

for (i in 1:7) {
  for (k in 1:10) {
```

```
    SETS[i,k] <- core[set.idx[[i]][k]]

  }

}

kable(SETS,
      caption = "Validation Training Sets",
      align = "c")
```

Table 1: *Validation Training Sets*

	Tumour 1	Tumour 2	Tumour 3	Tumour 4	Tumour 5	Healthy 1	Healthy 2	Healthy 3	Healthy 4	Healthy 5
Set 1	A02	B06	C10	E03	F08	H02	H08	H04	H08	H10
Set 2	A04	B08	D01	E05	F09	H08	H05	H06	H09	H05
Set 3	A06	B09	D04	E08	G01	H05	H06	H01	H09	H01
Set 4	A08	C02	D05	E09	G03	H02	H07	H01	H09	H08
Set 5	A09	C03	D07	F01	G05	H08	H06	H05	H07	H06
Set 6	B01	C05	D10	F03	G07	H03	H07	H07	H09	H08
Set 7	B03	C08	E01	F06	G09	H10	H09	H03	H05	H08

5.2 Classification Model Training

PLS-LDA was chosen as classification algorithm as it seems to have delivered the most reliable results in the past. Random forest models were also tested and resulted in similar classification accuracies. The author decided not to compare those results here as the differences are very small and the key problems are seen elsewhere.

The code chunk below is the actual training of the classification models. Execution took 3h 2min 2sec on a high spec desktop PC.

```
datasets = c("F:/Data/Agilent_QCL/dewaxed/",
             "F:/Data/Agilent_QCL/EMSC/",
             "F:/Data/Agilent_QCL/truncated/",
             "F:/Data/Bhargava_QCL/dewaxed/",
             "F:/Data/Bhargava_QCL/EMSC/",
             "F:/Data/Bhargava_QCL/truncated/",
             "F:/Data/FTIR/dewaxed/",
             "F:/Data/FTIR/EMSC/",
             "F:/Data/FTIR/truncated/")

for (i.dataset in 1:9) {

  files <- list.files(datasets[i.dataset],
```

```
                      pattern = ".RDS",
                      full.names = TRUE)

  for (i.cv in seq_along(set.idx)){
    idx = set.idx[[i.cv]]
    set.files = files[idx]

    spc = list()

    for (i.file in seq_along(set.files)) {

      file = set.files[i.file]

      spc [[i.file]] = readRDS(file)
    }
    tmp  <-  hyperSpec::collapse(spc)
    rm(spc)

    ##### Full image
    spc <-  tmp
    spc <- spc[spc$annotation != "Not Annotated"]
    spc$annotation = as.factor(spc$annotation)

localSave = paste0(datasets[i.dataset],"Full_Image_Model_", i.cv)
dir.create(localSave)

n.coef = 10
plslda.model <-  plslda(X = spc$spc,
                        grouping = spc$annotation,
                        comps = 1:n.coef,
                        ncomp = n.coef,
                        stripped = TRUE)

saveRDS(plslda.model, paste0(localSave,"/PLS_LDA_model.RDS"))

#### subseted annotation
localSave = paste0(datasets[i.dataset],"subset_Image_Model_", i.cv)
dir.create(localSave)

spc <-  tmp
spc <- spc[spc$annotation2 != "Not Annotated"]
spc$annotation2 = as.factor(spc$annotation2)
```

```
n.coef = 10
plslda.model <-  plslda(X = spc$spc,
                        grouping = spc$annotation2,
                        comps = 1:n.coef,
                        ncomp = n.coef,
                        stripped = TRUE)

saveRDS (plslda.model, paste0(localSave,"/PLS_LDA_model.RDS"))
  }



}

saveRDS(set.idx, paste0("F:/Data/CV_Indexes.RDS"))
```

5.3 Classification Model Predictions

The 126 models trained were then used to predict the pathology for all the samples not used in the training.

```
datasets = c("F:/Data/Agilent_QCL/dewaxed",
             "F:/Data/Agilent_QCL/EMSC",
             "F:/Data/Agilent_QCL/truncated",
             "F:/Data/Bhargava_QCL/dewaxed",
             "F:/Data/Bhargava_QCL/EMSC",
             "F:/Data/Bhargava_QCL/truncated",
             "F:/Data/FTIR/dewaxed",
             "F:/Data/FTIR/EMSC",
             "F:/Data/FTIR/truncated")

for (i.dataset in 1:9) {
   model.files <- list.files(datasets[i.dataset],
                       pattern = "PLS_LDA_model.RDS",
                       full.names = TRUE,
                       recursive = TRUE)

  models <- lapply(model.files, readRDS)

  core.files <- list.files(datasets[i.dataset],
                       pattern = ".RDS",
                       full.names = TRUE,
```

```
                    recursive = FALSE)


  for (i.core in seq_along(core.files)){

    file = core.files[i.core]
    test <- readRDS(file)

    for (i.cv in 1:14) {
    idx = set.idx[[rep(1:7,times = 2)[i.cv]]]
    if (i.core %in% idx) next

    savename <- sub(pattern = "PLS_LDA_model.RDS",
                    replacement= sub(".RDS", "", basename(file)),
                    model.files[i.cv])

    plslda.model <-  models[[i.cv]]
    PLSscores <- predict (plslda.model$pls,
                      newdata= test$spc,
                      type = "scores",
                      comps = plslda.model$comps)

    plslda.prediction <- predict (plslda.model$lda, newdata = PLSscores)

    if(i.cv > 8){mask = "annotation"} else{mask = "annotation2"}

    reference <-  test[[,mask,]][test[[,mask,]] != "Not Annotated"]
    predicition <-  droplevels(plslda.prediction$class[test[[,mask,]] != "Not Annotated"])

    saveRDS(list(reference, predicition),
            paste0(savename, "_predictions.RDS"))
       }
  }
}
```

5.4 Interpretation of Overall Performance

Plotted below is the accuracy of predictions for both training masks individually.

```
data = readRDS("F:/Data/2018_09_24_Prediction_AK.RDS")

p1 = ggplot(data[data$CV.mode == "full",], aes(x= Core, y= Accuracy)) +
```

```
  geom_point(aes(color = CV.set)) +
  theme(axis.text.x=element_text(angle=90,size=6, vjust=0.5))+
  facet_wrap(System ~ Treatment, ncol=1) +
  ggtitle("Accuracy for Full Annotation")

p1
```

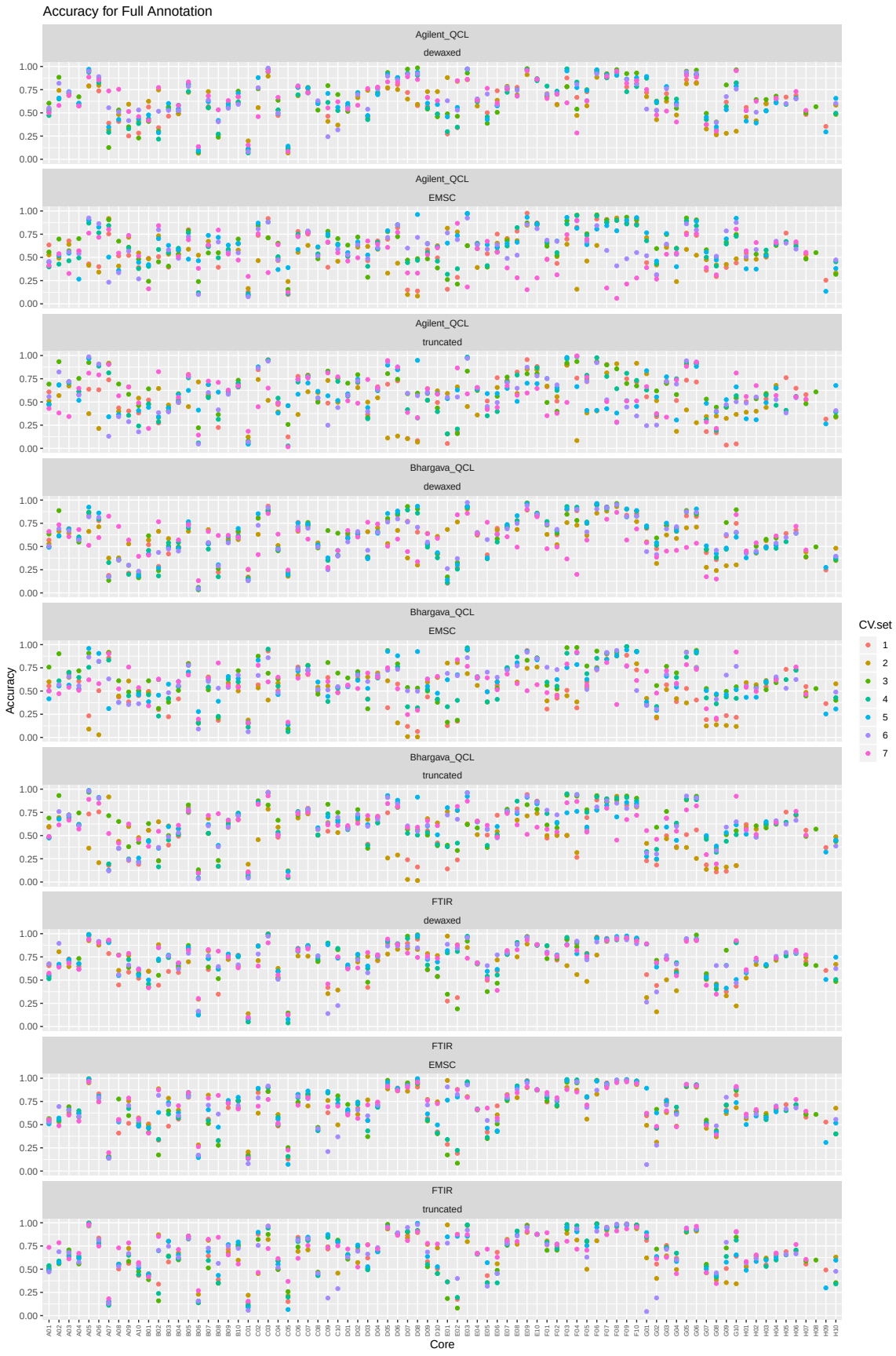
Accuracy for Full Annotation
Agilent_QCL
dewaxed
Agilent_QCL
EMSC
Agilent_QCL
truncated
Bhargava_QCL
dewaxed
Bhargava_QCL
EMSC
Bhargava_QCL
truncated
FTIR
dewaxed
FTIR
EMSC
FTIR
truncated
Accuracy
1.00
0.75
0.50
0.25
0.00
Core
CV.set
1
2
3
4
5
6
7

```
p2 =  ggplot(data[data$CV.mode == "subset",], aes(x= Core, y= Accuracy)) +
  geom_point(aes(color = CV.set)) +
     theme(axis.text.x=element_text(angle=90,size=6, vjust=0.5))+
  facet_wrap(System ~ Treatment, ncol=1) +
  ggtitle("Accuracy for Subset Annotation")

p2
```


Accuracy for Subset Annotation
Agilent_QCL
dewaxed
Agilent_QCL
EMSC
Agilent_QCL
truncated
Bhargava_QCL
dewaxed
Bhargava_QCL
EMSC
Bhargava_QCL
truncated
FTIR
dewaxed
FTIR
EMSC
FTIR
truncated
Accuracy
1.00
0.75
0.50
0.25
0.00
Core
CV.set
1
2
3
4
5
6
7

The overall performance has quite a high variability between samples as well as between models. The mean accuracies for the systems, treatments annotation masks are plotted below.

```
data_summary <- aggregate(data,
                          by= list(data$System,
                                   data$Treatment,
                                   data$CV.mode),
                          FUN = mean)

data_summary$System <-data_summary$Group.1
data_summary$Treatment <-data_summary$Group.2
data_summary$CV.mode <-data_summary$Group.3

p1 <- ggplot(data_summary, aes(x = System,
                               y = Accuracy,
                               colour= Treatment,
                               shape =CV.mode)
             ) +
        geom_point()
p1
```

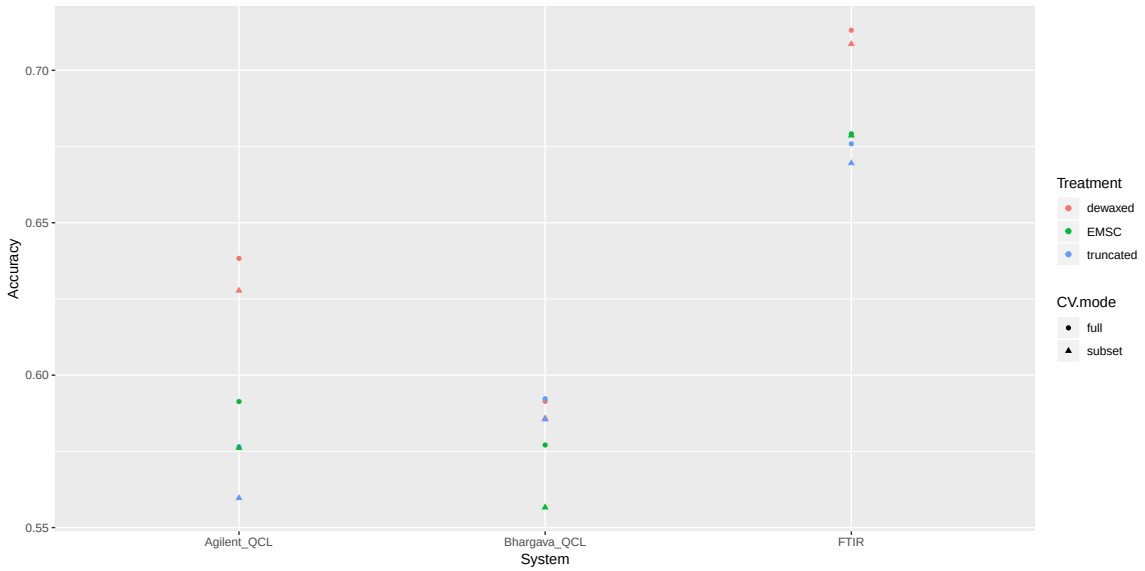

The FTIR clearly outperforms the other two systems and the full annotation set outperforms the subset. Accuracies of 60 to 70% however are not good enough for clinical diagnostics. For clinical diagnosis, this high level of annotation is not required and therefore it can be traded to ignore misclassification within the groups of benign and malignant and achieve higher accuracy.

```
files <- list.files("F:/Data",
                    pattern = "_predictions.RDS",
                    full.names = TRUE,
                    recursive = TRUE)

BreakAnnotation <- function (x){
  x <- revalue(x, c(
                   "Muscle" ="benign",
                    "Tumour" = "malignant",
                    "Stroma" = "benign",
                    "Necrosis" = "malignant",
                    "Old Squamous" = "benign",
                    "Young Squamous" = "benign"
                   )
               )
  x
}


for (i in seq_along(files))
{
  tmp = readRDS(files[i])

  tmp[[1]] <- factor(tmp[[1]], levels = levels(tmp[[2]]))
  tmp[[1]] <- BreakAnnotation(tmp[[1]])
  tmp[[2]] <- BreakAnnotation(tmp[[2]])


  tmp <- confusionMatrix(tmp[[1]], tmp[[2]])

  data[i,"Ensemble.Accuracy"]  <- tmp$overall[[1]]
  data[i,"Ensemble.Kappa"]  <- tmp$overall[[2]]

}
```

```
p1 = ggplot(data[data$CV.mode == "full",],
            aes(x= Core, y= Ensemble.Accuracy)) +
  geom_point(aes(color = CV.set)) +
  theme(axis.text.x=element_text(angle=90,
                                 size=6,
                                 vjust=0.5))+
  facet_wrap(System ~ Treatment, ncol =1) +
  ggtitle("Accuracy for full annotation")
```

```
p1
```


Accuracy for full annotation
Agilent_QCL
dewaxed
Agilent_QCL
EMSC
Agilent_QCL
truncated
Bhargava_QCL
dewaxed
Bhargava_QCL
EMSC
Bhargava_QCL
truncated
FTIR
dewaxed
FTIR
EMSC
FTIR
truncated
Ensemble.Accuracy
1.00
0.75
0.50
0.25
0.00
Core
CV.set
1
2
3
4
5
6
7

```
p2 =  ggplot(data[data$CV.mode == "subset",],
             aes(x= Core, y= Ensemble.Accuracy)) +
  geom_point(aes(color = CV.set)) +
  theme(axis.text.x=element_text(angle=90,
                                 size=6,
                                 vjust=0.5))+
  facet_wrap(System ~ Treatment, ncol = 1) +
  ggtitle("Accuracy for subset annotation")

p2
```


Accuracy for subset annotation
Agilent_QCL
dewaxed
Agilent_QCL
EMSC
Agilent_QCL
truncated
Bhargava_QCL
dewaxed
Bhargava_QCL
EMSC
Bhargava_QCL
truncated
FTIR
dewaxed
FTIR
EMSC
FTIR
truncated
Ensemble.Accuracy
1.00
0.75
0.50
0.25
0.00
Core
CV.set
1
2
3
4
5
6
7

```
data_summary <- aggregate(data,
                          by= list(data$System,
                                   data$Treatment,
                                   data$CV.mode),
                          FUN = mean)

data_summary$System <- data_summary$Group.1
data_summary$Treatment <- data_summary$Group.2
data_summary$CV.mode <- data_summary$Group.3

p1 <- ggplot(data_summary,
             aes(x = System,
                 y = Ensemble.Accuracy,
                 colour= Treatment,
                 shape =CV.mode)) +
  geom_point() +
  ylab("Accuracy")
p1
```

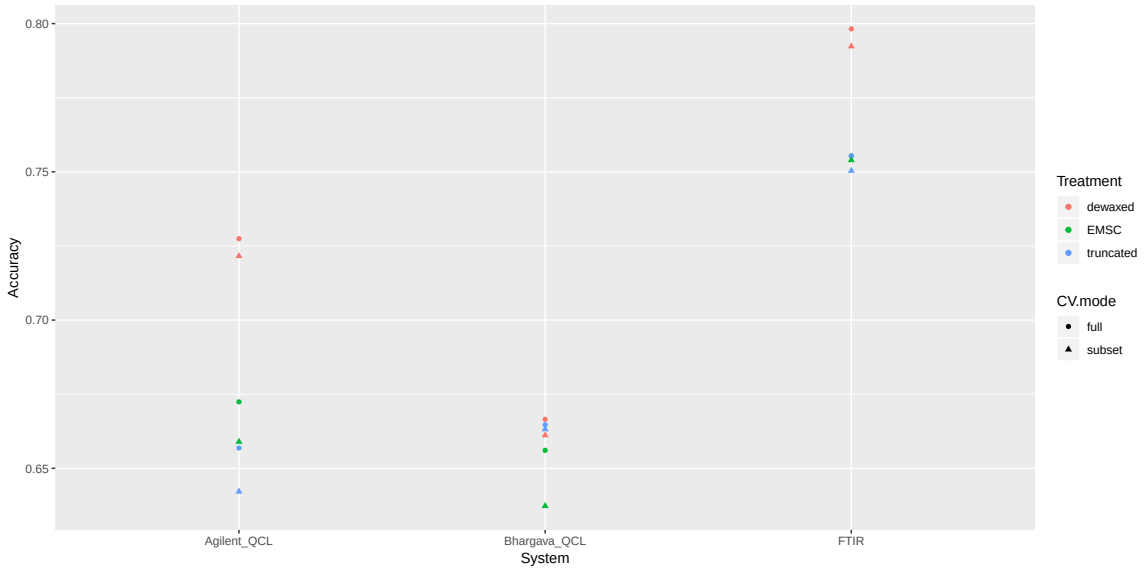

5.5 Accuracy for Aggregated Classes

```
files <- list.files("F:/Data",
                    pattern = "_predictions.RDS",
                    full.names = TRUE,
                    recursive = TRUE)
```

```
BreakAnnotation <- function (x){
  x <- revalue(x, c(
                    "Muscle" ="benign",
                     "Tumour" = "malignant",
                     "Stroma" = "benign",
                     "Necrosis" = "malignant",
                     "Old Squamous" = "benign",
                     "Young Squamous" = "benign"
                    )
                )
  x
}

for (i in seq_along(files))
{
  tmp = readRDS(files[i])

  tmp[[1]] <- factor(tmp[[1]], levels = levels(tmp[[2]]))
  tmp[[1]] <- BreakAnnotation(tmp[[1]])
  tmp[[2]] <- BreakAnnotation(tmp[[2]])

  tmp <- confusionMatrix(tmp[[1]], tmp[[2]])

  data[i,"Ensemble.Accuracy"]  <- tmp$overall[[1]]
  data[i,"Ensemble.Kappa"]  <- tmp$overall[[2]]
}
```

6 Whole Sample Classification: 'Threshold Voting'

```
cancercount = list()

for (i in seq_along(files))
{
  tmp = readRDS(files[i])

  tmp[[1]] <- factor(tmp[[1]], levels = levels(tmp[[2]]))
  tmp[[1]] <- BreakAnnotation(tmp[[1]])
  tmp[[2]] <- BreakAnnotation(tmp[[2]])

  cancercount[[i]] <- confusionMatrix(tmp[[1]], tmp[[2]])
  cancercount[[i]]$n.ref <- table(factor(tmp[[1]],
```

```
                                          levels = levels(tmp[[2]])))
  cancercount[[i]]$n.pred <- table(factor(tmp[[2]],
                                          levels = levels(tmp[[2]])))
}

for (i in seq_along(cancercount)) {
tmp <- cancercount[[i]]

data[i,"predicted.benign"]  <- tmp$n.pred[1] / sum(tmp$n.pred)
data[i,"reference.benign"]  <- tmp$n.ref[1] / sum(tmp$n.ref)
}
```

```
p2 =  ggplot(data[data$CV.mode == "full",],
              aes(x= Core,
                  y= predicted.benign)) +
  geom_point(aes(color = CV.set)) +
  facet_wrap(System ~ Treatment, ncol =1) +
  ggtitle("Percentage of pixels predicted as benign")

p2
```


Percentage of pixels predicted as benign
Agilent_QCL
dewaxed
Agilent_QCL
EMSC
Agilent_QCL
truncated
Bhargava_QCL
dewaxed
Bhargava_QCL
EMSC
Bhargava_QCL
truncated
FTIR
dewaxed
FTIR
EMSC
FTIR
truncated
predicted.benign
1.00
0.75
0.50
0.25
0.00
Core
CV.set
1
2
3
4
5
6
7

```
healthy <- c("H01", "H02", "H03", "H04", "H05",
             "H06", "H07", "H08", "H09", "H10")

data[data$Core %in% healthy,"pathology"] <- "Healthy"
data[!data$Core %in% healthy, "pathology"] <- "Cancer"
data$pathology <-  as.factor(data$pathology)

data$voted.prediction <- "Cancer"
data[data$predicted.benign > 0.7,"voted.prediction"] <- "Healthy"
data$voted.prediction <- as.factor(data$voted.prediction)

fullAnno <- data[data$CV.mode == "full",]
confusionMatrix(fullAnno$voted.prediction,
                fullAnno$pathology)
```

```
## Confusion Matrix and Statistics
##
##           Reference
## Prediction Cancer Healthy
##    Cancer    3838      59
##    Healthy    257     301
##
##                Accuracy : 0.9291
##                  95% CI : (0.9211, 0.9364)
##     No Information Rate : 0.9192
##     P-Value [Acc > NIR] : 0.007554
##
##                   Kappa : 0.6183
##  Mcnemar's Test P-Value : < 2.2e-16
##
##             Sensitivity : 0.9372
##             Specificity : 0.8361
##          Pos Pred Value : 0.9849
##          Neg Pred Value : 0.5394
##              Prevalence : 0.9192
##          Detection Rate : 0.8615
##    Detection Prevalence : 0.8747
##       Balanced Accuracy : 0.8867
##
```

```
##        'Positive' Class : Cancer
##
```

7 R Configuration Used

```
sessionInfo()
```

```
## R version 3.4.3 (2017-11-30)
## Platform: x86_64-w64-mingw32/x64 (64-bit)
## Running under: Windows 10 x64 (build 17134)
##
## Matrix products: default
##
## locale:
## [1] LC_COLLATE=English_United Kingdom.1252
## [2] LC_CTYPE=English_United Kingdom.1252
## [3] LC_MONETARY=English_United Kingdom.1252
## [4] LC_NUMERIC=C
## [5] LC_TIME=English_United Kingdom.1252
##
## attached base packages:
## [1] grid      stats     graphics  grDevices utils     datasets  methods
## [8] base
##
## other attached packages:
##  [1] corpcor_1.6.9           pls_2.6-0
##  [3] MASS_7.3-47             knitr_1.20
##  [5] caret_6.0-78            matrixStats_0.54.0
##  [7] gridExtra_2.3           dplyr_0.7.4
##  [9] plyr_1.8.4              gtools_3.5.0
## [11] FTIR_1.05               NMF_0.20.6
## [13] cluster_2.0.6           rngtools_1.2.4
## [15] pkgmaker_0.27           registry_0.3
## [17] hyperSpec_0.99-20171005 ggplot2_3.0.0
## [19] lattice_0.20-35
```

```
##
## loaded via a namespace (and not attached):
##  [1] nlme_3.1-131        lubridate_1.7.2     dimRed_0.1.0
##  [4] doParallel_1.0.10   RColorBrewer_1.1-2  rprojroot_1.2
##  [7] tools_3.4.3         backports_1.1.2     R6_2.2.1
## [10] rpart_4.1-11        lazyeval_0.2.0      colorspace_1.3-2
## [13] nnet_7.3-12         withr_2.1.1         tidyselect_0.2.4
## [16] mnormt_1.5-5        compiler_3.4.3      labeling_0.3
## [19] scales_0.5.0        sfsmisc_1.1-2       DEoptimR_1.0-8
## [22] psych_1.7.8         robustbase_0.92-8   stringr_1.2.0
## [25] digest_0.6.12       foreign_0.8-69      rmarkdown_1.7
## [28] pkgconfig_2.0.1     htmltools_0.3.6     bibtex_0.4.2
## [31] highr_0.6           rlang_0.2.0         ddalpha_1.3.1.1
## [34] bindr_0.1           ModelMetrics_1.1.0  magrittr_1.5
## [37] Matrix_1.2-12       Rcpp_0.12.19        munsell_0.5.0
## [40] stringi_1.1.5       yaml_2.2.0          recipes_0.1.2
## [43] parallel_3.4.3      crayon_1.3.2        splines_3.4.3
## [46] reshape2_1.4.2      codetools_0.2-15    stats4_3.4.3
## [49] CVST_0.2-1          glue_1.2.0          evaluate_0.10
## [52] latticeExtra_0.6-28 foreach_1.4.4       testthat_1.0.2
## [55] gtable_0.2.0        purrr_0.2.4         tidyr_0.8.0
## [58] kernlab_0.9-25      assertthat_0.2.0    DRR_0.0.3
## [61] gridBase_0.4-7      gower_0.1.2         prodlim_1.6.1
## [64] xtable_1.8-2        broom_0.4.3         e1071_1.6-8
## [67] class_7.3-14        survival_2.41-3     timeDate_3043.102
## [70] RcppRoll_0.2.2      tibble_1.3.3        iterators_1.0.8
## [73] bindrcpp_0.2        lava_1.6            ipred_0.9-6
```

Bibliography

[1] M. Hermes, R. B. Morrish, L. Huot, L. Meng, S. Junaid, J. Tomko, G. R. Lloyd, W. T. Masselink, P. Tidemand-Lichtenberg, C. Pedersen, F. Palombo, N. Stone, "Mid-IR hyperspectral imaging for label-free histopathology and cytology", in *Journal of Optics* **02/2018**, *20*, 023002, DOI 10.1088/2040-8986/aaa36b, (cit. on pp. 2, 26, 67).

[2] O. Stevens, I. E. Iping Petterson, J. C. C. Day, N. Stone, J. Helfmann, H.-J. Cappius, J. W. Fluhr, M. C. Meinke, J. Kirkham, T. Upile, M. Schmitt, L. Marcu, J. Popp, "Developing fibre optic Raman probes for applications in clinical spectroscopy", in *Chem. Soc. Rev.* **2016**, *45*, 1919–1934, DOI 10.1039/C5CS00850F, (cit. on p. 2).

[3] P. Matousek, N. Stone, "Development of deep subsurface Raman spectroscopy for medical diagnosis and disease monitoring", in *Chem. Soc. Rev.* **2016**, *45*, 1794–1802, DOI 10.1039/C5CS00466G, (cit. on p. 2).

[4] M. J. Baker, S. R. Hussain, L. Lovergne, V. Untereiner, C. Hughes, R. A. Lukaszewski, G. Thiéfin, G. D. Sockalingum, "Developing and understanding biofluid vibrational spectroscopy: a critical review", in *Chem. Soc. Rev.* **2016**, *45*, 1803–1818, DOI 10.1039/C5CS00585J, (cit. on pp. 2, 38).

[5] J. D. Horsnell, J. A. Smith, M. Sattlecker, A. Sammon, J. Christie-Brown, C. Kendall, N. Stone, "Raman spectroscopy – A potential new method for the intra–operative assessment of axillary lymph nodes", in *The Surgeon* **06/2012**, *10*, 123–127, DOI 10.1016/j.surge.2011.02.004, (cit. on p. 2).

[6] H. J. Butler, L. Ashton, B. Bird, G. Cinque, K. Curtis, J. Dorney, K. Esmonde-White, N. J. Fullwood, B. Gardner, P. L. Martin-Hirsch, M. J. Walsh, M. R. McAinsh, N. Stone, F. L. Martin, "Using Raman spectroscopy to characterize biological materials", in *Nature Protocols* **03/2016**, *11*, 664–687, DOI 10.1038/nprot.2016.036, (cit. on p. 2).

[7] K. Kong, C. Kendall, N. Stone, I. Notingher, "Raman spectroscopy for medical diagnostics – From in-vitro biofluid assays to in-vivo cancer detection", in *Advanced Drug Delivery Reviews* **07/2015**, *89*, 121–134, DOI 10.1016/j.addr.2015.03.009, (cit. on p. 2).

[8] C. Krafft, B. Dietzek, J. Popp, "Raman and CARS microspectroscopy of cells and tissues", in *The Analyst* **06/2009**, *134*, 1046, DOI 10.1039/b822354h, (cit. on pp. 2, 39, 67).

[9] M. Skacel, R. E. Petras, T. L. Gramlich, J. E. Sigel, J. E. Richter, J. R. Goldblum, "The diagnosis of low-grade dysplasia in Barrett's esophagus and its implications for disease progression", in *The American Journal of Gastroenterology* **12/2000**, *95*, 3383–3387, DOI 10.1111/j.1572-0241.2000.03348.x, (cit. on p. 2).

[10] C. Kendall, N. Stone, N. Shepherd, K. Geboes, B. Warren, R. Bennett, H. Barr, "Raman spectroscopy, a potential tool for the objective identification and classification of neoplasia in Barrett's oesophagus", in *The Journal of Pathology* **08/2003**, *200*, 602–609, DOI 10.1002/path.1376, (cit. on pp. 2, 48, 50, 51, 67).

[11] R. Bhargava, "Infrared Spectroscopic Imaging: The Next Generation", in *Applied Spectroscopy* **10/2012**, *66*, 1091–1120, DOI 10.1366/12-06801, (cit. on pp. 3, 80).

[12] M. J. Pilling, A. Henderson, B. Bird, M. D. Brown, N. W. Clarke, P. Gardner, "High-throughput quantum cascade laser (QCL) spectral histopathology: a practical approach towards clinical translation", in *Faraday Discuss.* **2016**, *187*, 135–154, DOI 10.1039/C5FD00176E, (cit. on pp. 3, 37, 39, 78).

[13] C. H. Camp Jr, M. T. Cicerone, "Chemically sensitive bioimaging with coherent Raman scattering", in *Nature Photonics* **04/2015**, *9*, 295–305, DOI 10.1038/nphoton.2015.60, (cit. on p. 3).

[14] E. R. Amstalden Van Hove, D. F. Smith, R. M. A. Heeren, "A concise review of mass spectrometry imaging", in *Journal of Chromatography A* **2010**, *1217*, 3946–3954, DOI 10.1016/j.chroma.2010.01.033, (cit. on p. 3).

[15] R. M. A. Heeren, D. F. Smith, J. Stauber, B. Kükrer-Kaletas, L. MacAleese, "Imaging mass spectrometry: Hype or hope?", in *Journal of the American Society for Mass Spectrometry* **06/2009**, *20*, 1006–1014, DOI 10.1016/j.jasms.2009.01.011, (cit. on p. 3).

[16] P. Bazylewski, S. Ezugwu, G. Fanchini, "A Review of Three-Dimensional Scanning Near-Field Optical Microscopy (3D-SNOM) and Its Applications in Nanoscale Light Management", in *Applied Sciences* **09/2017**, *7*, 973, DOI 10.3390/app7100973, (cit. on pp. 4, 101).

[17] I. Amenabar, S. Poly, W. Nuansing, E. H. Hubrich, A. A. Govyadinov, F. Huth, R. Krutokhvostov, L. Zhang, M. Knez, J. Heberle, A. M. Bittner, R. Hillenbrand, "Structural analysis and mapping of individual protein complexes by infrared nanospectroscopy", in *Nature Communications* **12/2013**, *4*, 2890, DOI 10.1038/ncomms3890, (cit. on p. 4).

[18] A. Dazzi, C. B. Prater, "AFM-IR: Technology and Applications in Nanoscale Infrared Spectroscopy and Chemical Imaging", in *Chemical Reviews* **04/2017**, *117*, 5146–5173, DOI 10.1021/acs.chemrev.6b00448, (cit. on p. 4).

[19] A. Dazzi, C. B. Prater, Q. Hu, D. B. Chase, J. F. Rabolt, C. Marcott, "AFM-IR: Combining atomic force microscopy and infrared spectroscopy for nanoscale chemical characterization", in *Applied Spectroscopy* **12/2012**, *66*, 1365–1384, DOI 10.1366/12-06804, (cit. on p. 4).

[20] F. Huth, M. Schnell, J. Wittborn, N. Ocelic, R. Hillenbrand, "Infrared-spectroscopic nanoimaging with a thermal source", in *Nature Materials* **05/2011**, *10*, 352–356, DOI 10.1038/nmat3006, (cit. on p. 4).

[21] A. C. Jones, M. B. Raschke, "Thermal Infrared Near-Field Spectroscopy", in *Nano Letters* **03/2012**, *12*, 1475–1481, DOI 10.1021/nl204201g, (cit. on p. 4).

[22] M. Unger, C. Marcott in *Encyclopedia of Analytical Chemistry*, John Wiley & Sons, Ltd, Chichester, UK, **06/2017**, pp. 1–26 (cit. on p. 4).

[23] C. Westermeier, A. Cernescu, S. Amarie, C. Liewald, F. Keilmann, B. Nickel, "Sub-micron phase coexistence in small-molecule organic thin films revealed by infrared nano-imaging", in *Nature Communications* **06/2014**, *5*, 4101, DOI 10.1038/ncomms5101, (cit. on p. 4).

[24] M. Abo-Bakr, J. Feikes, K. Holldack, P. Kuske, W. B. Peatman, U. Schade, G. Wüstefeld, H.-W. Hübers, "Brilliant, Coherent Far-Infrared (THz) Synchrotron Radiation", in *Physical Review Letters* **03/2003**, *90*, 094801, DOI 10.1103/PhysRevLett.90.094801, (cit. on p. 5).

[25] Z. Huang in Proceedings of IPAC 2013, Shanghai, China (MOYCB101), **2013**, pp. 16–20 (cit. on p. 5).

[26] B. W. J. McNeil, N. R. Thompson, "X-ray free-electron lasers", in *Nature Photonics* **12/2010**, *4*, 814–821, DOI 10.1038/nphoton.2010.239, (cit. on p. 5).

[27] T. Kawasaki, T. Imai, K. Tsukiyama, "Use of a Mid-Infrared Free-Electron Laser (MIR-FEL) for Dissociation of the Amyloid Fibril Aggregates of a Peptide", in *Journal of Analytical Sciences Methods and Instrumentation* **2014**, *04*, 9–18, DOI 10.4236/jasmi.2014.41002, (cit. on p. 5).

[28] A. Godard, Infrared (2-12 μm) solid-state laser sources: a review, **12/2007** (cit. on p. 5).

[29] J. Faist, F. Capasso, D. L. Sivco, C. Sirtori, A. L. Hutchinson, A. Y. Cho, "Quantum Cascade Laser", in *Science* **1994**, *264*, 553–556, DOI 10.1126/science.264.5158.553, (cit. on p. 6).

[30] D. Heydari, Y. Bai, N. Bandyopadhyay, S. Slivken, M. Razeghi, "High brightness angled cavity quantum cascade lasers", in *Applied Physics Letters* **03/2015**, *106*, 091105, DOI 10.1063/1.4914477, (cit. on p. 6).

[31] Y. Bai, S. Darvish, N. Bandyopadhyay, S. Slivken, M. Razeghi, "Optimizing facet coating of quantum cascade lasers for low power consumption", in *J Appl Phys* **2011**, *109*, DOI 10.1063/1.3553863, (cit. on p. 6).

[32] A. Lyakh, R. Maulini, A. Tsekoun, R. Go, C. K. N. Patel, "Tapered 47 μm quantum cascade lasers with highly strained active region composition delivering over 45 watts of continuous wave optical power", in *Optics Express* **02/2012**, *20*, 4382, DOI 10.1364/OE.20.004382, (cit. on p. 6).

[33] N. Bandyopadhyay, Y. Bai, S. Tsao, S. Nida, S. Slivken, M. Razeghi, "Room temperature continuous wave operation of 3-3.2micrometer quantum cascade lasers", in *Applied Physics Letters* **12/2012**, *101*, 241110, DOI 10.1063/1.4769038, (cit. on p. 6).

[34] O. Cathabard, R. Teissier, J. Devenson, J. C. Moreno, A. N. Baranov, "Quantum cascade lasers emitting near 2.6 μm", in *Applied Physics Letters* **04/2010**, *96*, 141110, DOI 10.1063/1.3385778, (cit. on p. 6).

[35] M. P. Semtsiv, M. Wienold, S. Dressler, W. T. Masselink, "Short-wavelength (?????3.05 ??m) InP-based strain-compensated quantum-cascade laser", in *Applied Physics Letters* **01/2007**, *90*, 051111, DOI 10.1063/1.2437108, (cit. on p. 6).

[36] I. Vurgaftman, R. Weih, M. Kamp, J. R. Meyer, C. L. Canedy, C. S. Kim, M. Kim, W. W. Bewley, C. D. Merritt, J. Abell, S. Höfling, Interband cascade lasers, **04/2015** (cit. on p. 6).

[37] K. Ohtani, M. Beck, J. Faist, "Double metal waveguide InGaAs/AlInAs quantum cascade lasers emitting at 24 ?? m", in *Applied Physics Letters* **09/2014**, *105*, 121115, DOI 10.1063/1.4896542, (cit. on p. 6).

[38] O. Fedosenko, M. Chashnikova, S. MacHulik, J. Kischkat, M. Klinkmüller, A. Aleksandrova, G. Monastyrskyi, M. P. Semtsiv, W. T. Masselink, "Scaling the output power of quantum-cascade lasers with a number of cascades", in *Journal of Crystal Growth* **05/2011**, *323*, 484–487, DOI 10.1016/j.jcrysgro.2010.11.131, (cit. on pp. 6, 8).

[39] W. T. Masselink, M. P. Semtsiv, Y. V. Flores, A. Aleksandrova, J. Kischkat in Proc. SPIE 9989, (Eds.: D. H. Titterton, R. J. Grasso, M. A. Richardson), International Society for Optics and Photonics, **10/2016**, 99890B–1–9 (cit. on p. 6).

[40] N. Bandyopadhyay, M. Chen, S. Sengupta, S. Slivken, M. Razeghi, Ultra-broadband quantum cascade laser, tunable over 760 cm-1, with balanced gain, **08/2015** (cit. on pp. 6, 8).

[41] R. Centeno, D. Marchenko, J. Mandon, S. M. Cristescu, G. Wulterkens, F. J. Harren, "High power, widely tunable, mode-hop free, continuous wave external cavity quantum cascade laser for multi-species trace gas detection", in *Applied Physics Letters* **12/2014**, *105*, 261907, DOI 10.1063/1.4905281, (cit. on pp. 6, 9).

[42] A. Hugi, R. Terazzi, Y. Bonetti, A. Wittmann, M. Fischer, M. Beck, J. Faist, E. Gini, "External cavity quantum cascade laser tunable from 7.6 to 11.4 μm", in *Applied Physics Letters* **08/2009**, *95*, 061103, DOI 10.1063/1.3193539, (cit. on pp. 6, 9).

[43] W. Zhou, N. Bandyopadhyay, D. Wu, R. McClintock, M. Razeghi, "Monolithically, widely tunable quantum cascade lasers based on a heterogeneous active region design", in **06/2016**, *6*, 25213, DOI 10.1038/srep25213http://10.0.4.14/srep25213, (cit. on pp. 6, 8).

[44] Z.-W. Jia, L.-J. Wang, J.-C. Zhang, F.-Q. Liu, Y.-H. Zhou, D.-B. Wang, X.-F. Jia, N. Zhuo, J.-Q. Liu, S.-Q. Zhai, Z.-G. Wang, "High Efficiency, Low Power-Consumption DFB Quantum Cascade Lasers Without Lateral Regrowth", in *Nanoscale Research Letters* **2017**, *12*, 281, DOI 10.1186/s11671-017-2064-2, (cit. on p. 8).

[45] S. Slivken, S. Sengupta, M. Razeghi, "High power continuous operation of a widely tunable quantum cascade laser with an integrated amplifier", in *Applied Physics Letters* **12/2015**, *107*, 251101, DOI 10.1063/1.4938005, (cit. on p. 8).

[46] A. Hugi, R. Maulini, J. Faist, External cavity quantum cascade laser, **08/2010** (cit. on p. 8).

[47] V. S. Starovoitov, J. F. Kischkat, M. P. Semtsiv, W. Ted Masselink, "Intracavity photoacoustic sensing of water vapor with a continuously tunable external-cavity quantum-cascade laser operating near 55 μm", in *Optics Letters* **11/2016**, *41*, 4955, DOI 10.1364/OL.41.004955, (cit. on p. 9).

[48] G. Wysocki, R. Lewicki, R. F. Curl, F. K. Tittel, L. Diehl, F. Capasso, M. Troccoli, G. Hofler, D. Bour, S. Corzine, R. Maulini, M. Giovannini, J. Faist, "Widely tunable mode-hop free external cavity quantum cascade lasers for high resolution spectroscopy and chemical sensing", in *Applied Physics B: Lasers and Optics* **09/2008**, *92*, 305–311, DOI 10.1007/s00340-008-3047-x, (cit. on p. 9).

[49] J. Kischkat, M. P. Semtsiv, M. Elagin, G. Monastyrskyi, Y. Flores, S. Kurlov, S. Peters, W. T. Masselink, "Alignment-stabilized interference filter-tuned external-cavity quantum cascade laser.", in *Optics letters* **12/2014**, *39*, 6561–4, DOI 10.1364/OL.39.006561, (cit. on p. 9).

[50] A. Lyakh, R. Barron-Jimenez, I. Dunayevskiy, R. Go, C. K. N. Patel, "External cavity quantum cascade lasers with ultra rapid acousto-optic tuning", in *Applied Physics Letters* **04/2015**, *106*, 141101, DOI 10.1063/1.4917241, (cit. on p. 9).

[51] C. K. N. Patel, R. Barron-Jimenez, I. Dunayevskiy, G. Tsvid, A. Lyakh, "Two wavelength operation of an acousto-optically tuned quantum cascade laser and direct measurements of quantum cascade laser level lifetimes", in *Applied Physics Letters* **01/2017**, *110*, 031104, DOI 10.1063/1.4974214, (cit. on p. 9).

[52] R. R. Alfano, S. L. Shapiro, "Emission in the region 4000 to 7000 via four-photon coupling in glass", in *Physical Review Letters* **03/1970**, *24*, 584–587, DOI 10.1103/PhysRevLett.24.584, (cit. on p. 9).

[53] V. V. Alexander, O. P. Kulkarni, M. Kumar, C. Xia, M. N. Islam, F. L. Terry, M. J. Welsh, K. Ke, M. J. Freeman, M. Neelakandan, A. Chan, "Modulation instability initiated high power all-fiber supercontinuum lasers and their applications", in *Optical Fiber Technology* **09/2012**, *18*, 349–374, DOI 10.1016/j.yofte.2012.07.014, (cit. on p. 9).

[54] J. Dudley, *Supercontinuum generation in optical fibers*, Cambridge University Press, Berlin, **2010**, p. 501 (cit. on p. 9).

[55] P. M. Moselund, L. Huot, C. D. Brooks, "All-fiber mid-IR supercontinuum: a powerful new tool for IR-spectroscopy", (Eds.: R. R. Alfano, S. G. Demos), in *Proc. of SPIE* **03/2016**, *9703*, 97030B–1–6, DOI 10.1117/12.2213129, (cit. on p. 9).

[56] C. R. Petersen, U. Møller, I. Kubat, B. Zhou, S. Dupont, J. Ramsay, T. Benson, S. Sujecki, N. Abdel-Moneim, Z. Tang, D. Furniss, A. Seddon, O. Bang, "Mid-infrared supercontinuum covering the 1.4-13.3 μm molecular fingerprint region using ultra-high NA chalcogenide step-index fibre", in *Nature Photonics* **09/2014**, *8*, 830–834, DOI 10.1038/nphoton.2014.213, (cit. on p. 9).

[57] U. Møller, Y. Yu, I. Kubat, C. R. Petersen, X. Gai, L. Brilland, D. Méchin, C. Caillaud, J. Troles, B. Luther-Davies, O. Bang, "Multi-milliwatt mid-infrared supercontinuum generation in a suspended core chalcogenide fiber", in *Optics Express* **02/2015**, *23*, 3282, DOI 10.1364/OE.23.003282, (cit. on p. 10).

[58] I. Kubat et al., "Mid-infrared supercontinuum generation to 12.5μm in large NA chalcogenide step-index fibres pumped at 4.5μm.", in *Optics express* **08/2014**, *22*, 19169–82, DOI 10.1364/OE.22.019169, (cit. on p. 10).

[59] I. D. Lindsay et al., "Towards supercontinuum-driven hyperspectral microscopy in the mid-infrared", (Eds.: R. R. Alfano, S. G. Demos), in *Proc. SPIE* **03/2016**, *9703*, 970304–1–9, DOI 10.1117/12.2210836, (cit. on p. 10).

[60] M. Farries, J. Ward, S. Valle, G. Stephens, P. Moselund, K. Van Der Zanden, B. Napier in Journal of Physics: Conference Series, *Vol. 619*, IOP Publishing, **06/2015**, p. 012032 (cit. on p. 10).

[61] L. Huot, P. M. Moselund, L. Leick, P. Tidemand-Lichtenberg, C. Pedersen, "Broadband upconversion imaging around 4 μm using an all-fiber supercontinuum source", (Eds.: K. L. Vodopyanov, K. L. Schepler), in *Proc. SPIE* **02/2017**, *10088*, 100880J–1–7, DOI 10.1117/12.2251805, (cit. on p. 10).

[62] M. Vainio, L. Halonen, "Mid-infrared optical parametric oscillators and frequency combs for molecular spectroscopy", in *Physical Chemistry Chemical Physics* **2016**, *18*, 4266–4294, DOI 10.1039/C5CP07052J, (cit. on p. 10).

[63] L. E. Myers, R. C. Eckardt, M. M. Fejer, R. L. Byer, W. R. Bosenberg, J. W. Pierce, "Quasi-phase-matched optical parametric oscillators in bulk periodically poled LiNbO_3", in *Journal of the Optical Society of America B* **1995**, *12*, 2102, DOI 10.1364/JOSAB.12.002102, (cit. on p. 11).

[64] K. Petrov, A. Ryan, T. Patterson, L. Huang, S. Field, D. Bamford, "Mid-infrared spectroscopic detection of trace gases using guided-wave difference-frequency generation", in *Applied Physics B* **09/1998**, *67*, 357–361, DOI 10.1007/s003400050516, (cit. on p. 11).

[65] D. Hofmann, G. Schreiber, C. Haase, H. Herrmann, W. Grundkötter, R. Ricken, W. Sohler, "Quasi-phase-matched difference-frequency generation in periodically poled Ti:LiNbO3 channel waveguides", in *Opt. Lett.* **07/1999**, *24*, 896–898, DOI 10.1364/OL.24.000896, (cit. on p. 11).

[66] M. Asobe, O. Tadanaga, T. Yanagawa, T. Umeki, Y. Nishida, H. Suzuki, "High-power mid-infrared wavelength generation using difference frequency generation in damage-resistant Zn:LiNbO¡sub¿3¡/sub¿ waveguide", in *Electronics Letters* **02/2008**, *44*, 288–2902, DOI 10.1049/el_20083287, (cit. on p. 11).

[67] P. Zeil, N. Thilmann, V. Pasiskevicius, F. Laurell, "High-power, single-frequency, continuous-wave optical parametric oscillator employing a variable reflectivity volume Bragg grating", in *Opt. Express* **12/2014**, *22*, 29907–29913, DOI 10.1364/OE.22.029907, (cit. on p. 11).

[68] L. E. Garn, "Fundamental noise limits of thermal detectors", in *Journal of Applied Physics* **03/1984**, *55*, 1243–1253, DOI 10.1063/1.333212, (cit. on pp. 13, 14).

[69] A. Rogalski, *Infrared detectors*, CRC Press, **2011**, p. 876 (cit. on pp. 13, 14).

[70] C. Draijer, Microbolometers Move Thermal Imaging into Next-Gen Commercial Uses — Features — Nov 2014 — Photonics Spectra, **2014** (cit. on p. 14).

[71] Pearsall, T.P.; Pollack, M.A.; Tsang, W. T in, Elsevier textbooks, **1985**, p. 363 (cit. on p. 14).

[72] B. E. A. Saleh, M. C. Teich in *Fundamentals of Photonics*, John Wiley & Sons, Inc., New York, USA, pp. 238–271 (cit. on p. 14).

[73] L. Ma, O. Slattery, A. Mink, X. Tang in Proceedings of SPIE, *Vol. 7465*, **2009**, 74650W (cit. on pp. 17, 18).

[74] J. S. Dam, C. Pedersen, P. Tidemand-Lichtenberg, "Theory for upconversion of incoherent images", in *Optics Express* **01/2012**, *20*, 1475, DOI 10.1364/OE.20.001475, (cit. on pp. 17, 18, 81, 82).

[75] S. Junaid, P. Tidemand-Lichtenberg, C. Pedersen, "Upconversion based spectral imaging in 6 to 8 μm spectral regime", (Eds.: K. L. Vodopyanov, K. L. Schepler), in *Proc. SPIE* **02/2017**, *10088*, DOI 10.1117/12.2250538, (cit. on pp. 17, 18).

[76] J. S. Dam, P. Tidemand-Lichtenberg, C. Pedersen, "Room-temperature mid-infrared single-photon spectral imaging", in *Nature Photonics* **09/2012**, *6*, 788–793, DOI 10.1038/nphoton.2012.231, (cit. on pp. 17, 85).

[77] A. McCarthy, N. J. Krichel, N. R. Gemmell, X. Ren, M. G. Tanner, S. N. Dorenbos, V. Zwiller, R. H. Hadfield, G. S. Buller, "Kilometer-range, high resolution depth imaging via 1560 nm wavelength single-photon detection", in *Optics Express* **04/2013**, *21*, 8904, DOI 10.1364/OE.21.008904, (cit. on p. 17).

[78] P. Tidemand-Lichtenberg, J. S. Dam, H. V. Andersen, L. Hogstedt, C. Pedersen, "Mid-infrared upconversion spectroscopy", in *Journal of the Optical Society of America B* **11/2016**, *33*, D28, DOI 10.1364/JOSAB.33.000D28, (cit. on pp. 18, 96).

[79] H. Xia, G. Shentu, M. Shangguan, X. Xia, X. Jia, C. Wang, J. Zhang, J. S. Pelc, M. M. Fejer, Q. Zhang, X. Dou, J.-W. Pan, "Long-range micro-pulse aerosol lidar at 1 . 5 μ m with an upconversion single-photon detector", in *Optics Letters* **04/2015**, *40*, 1579–1582, DOI 10.1364/OL.40.001579, (cit. on p. 18).

[80] E. P. W. Hawkes, E. Board, A. L. S. A. E. Siegman, M. E. H. K. V. Lotsch, *Springer Series in Optical Sciences Volume 45 Springer-Verlag Berlin Heidelberg GmbH Springer Series in Optical Sciences*, Springer Berlin Heidelberg, Berlin, Heidelberg, **1998**, p. 515 (cit. on p. 18).

[81] G. B. Lemos, V. Borish, G. D. Cole, S. Ramelow, R. Lapkiewicz, A. Zeilinger, "Quantum imaging with undetected photons", in *Nature* **08/2014**, *512*, 409–412, DOI 10.1038/nature13586, (cit. on p. 19).

[82] I. Pupeza et al., "High-power sub-two-cycle mid-infrared pulses at 100 MHz repetition rate", in *Nature Photonics* **09/2015**, *9*, 721–724, DOI 10.1038/nphoton.2015.179, (cit. on p. 19).

[83] H. W. Schweinberger, L. Vamos, M. Huber, J. Zhang, M. Trubetskov, N. Lilienfein, A. Apolonski, V. Pervak, N. Karpowicz, O. Pronin, I. Pupeza in High-Brightness Sources and Light-Driven Interactions, OSA, Washington, **2016**, MT1C.5 (cit. on p. 19).

[84] K. Schwarzschild, *Untersuchungen zur geometrischen Optik. I. Einleitung in die Fehlertheorie optischer Instrumente auf Grund des Eikonalbegriffs. Vol. 4*, Druck der Dieterich'schen Univ.-Buchdruckerei (W. Fr. Kaestner), **1905**, pp. 1–54 (cit. on p. 19).

[85] M. J. Riedl, *Optical design - Fundamentals for infrared systems. Second edition*, SPIE Press, **2001**, pp. 1–182 (cit. on p. 19).

[86] K. L. A. Chan, S. G. Kazarian, "New Opportunities in Micro- and Macro-Attenuated Total Reflection Infrared Spectroscopic Imaging: Spatial Resolution and Sampling Versatility", in *Applied Spectroscopy* **04/2003**, *57*, 381–389, DOI 10.1366/00037020360625907, (cit. on p. 19).

[87] K. Yeh, S. Kenkel, J.-N. Liu, R. Bhargava, "Fast Infrared Chemical Imaging with a Quantum Cascade Laser", in *Analytical Chemistry* **01/2015**, *87*, 485–493, DOI 10.1021/ac5027513, (cit. on p. 19).

[88] K. L. Andrew Chan, S. G. Kazarian, "Attenuated total reflection Fourier-transform infrared (ATR-FTIR) imaging of tissues and live cells", in *Chem. Soc. Rev.* **2016**, *45*, 1850–1864, DOI 10.1039/C5CS00515A, (cit. on p. 21).

[89] S. Kazarian, K. Chan, "Applications of ATR-FTIR spectroscopic imaging to biomedical samples", in *Biochimica et Biophysica Acta (BBA) - Biomembranes* **07/2006**, *1758*, 858–867, DOI 10.1016/j.bbamem.2006.02.011, (cit. on p. 21).

[90] J. A. Kimber, S. G. Kazarian, "Spectroscopic imaging of biomaterials and biological systems with FTIR microscopy or with quantum cascade lasers", in *Analytical and Bioanalytical Chemistry* **10/2017**, *409*, 5813–5820, DOI 10.1007/s00216-017-0574-5, (cit. on p. 21).

[91] F. Palombo, H. Shen, L. E. S. Benguigui, S. G. Kazarian, R. K. Upmacis, "Micro ATR-FTIR spectroscopic imaging of atherosclerosis: an investigation of the contribution of inducible nitric oxide synthase to lesion composition in ApoE-null mice", in *The Analyst* **06/2009**, *134*, 1107, DOI 10.1039/b821425e, (cit. on p. 21).

[92] F. Palombo, S. G. Cremers, P. D. Weinberg, S. G. Kazarian, "Application of Fourier transform infrared spectroscopic imaging to the study of effects of age and dietary L-arginine on aortic lesion composition in cholesterol-fed rabbits.", in *Journal of the Royal Society Interface* **08/2009**, *6*, 669–80, DOI 10.1098/rsif.2008.0325, (cit. on p. 21).

[93] F. Palombo, C. B. Danoux, P. D. Weinberg, S. G. Kazarian, "Measurement of drug and macromolecule diffusion across atherosclerotic rabbit aorta ex vivo by attenuated total reflection–Fourier transform infrared imaging", in *Journal of Biomedical Optics* **2009**, *14*, 044008, DOI 10.1117/1.3174395, (cit. on p. 21).

[94] G. Mie, “Beitr??ge zur Optik tr??ber Medien, speziell kolloidaler Metall??sungen”, in *Annalen der Physik* **1908**, *330*, 377–445, DOI 10.1002/andp.19083300302, (cit. on p. 22).

[95] P. Bassan, H. J. Byrne, J. Lee, F. Bonnier, C. Clarke, P. Dumas, E. Gazi, M. D. Brown, N. W. Clarke, P. Gardner, “Reflection contributions to the dispersion artefact in FTIR spectra of single biological cells”, in *The Analyst* **2009**, *134*, 1171, DOI 10.1039/b821349f, (cit. on pp. 22, 29).

[96] T. Konevskikh, R. Lukacs, R. Blümel, A. Ponossov, A. Kohler, “Mie scatter corrections in single cell infrared microspectroscopy”, in *Faraday Discuss.* **2016**, *187*, 235–257, DOI 10.1039/C5FD00171D, (cit. on p. 22).

[97] T. Konevskikh, R. Lukacs, A. Kohler, “An improved algorithm for fast resonant Mie scatter correction of infrared spectra of cells and tissues”, in *Journal of Biophotonics* **10/2017**, e201600307, DOI 10.1002/jbio.201600307, (cit. on p. 22).

[98] P. Bassan, J. Lee, A. Sachdeva, J. Pissardini, K. M. Dorling, J. S. Fletcher, A. Henderson, P. Gardner, “The inherent problem of transflection-mode infrared spectroscopic microscopy and the ramifications for biomedical single point and imaging applications.”, in *Analyst* **01/2013**, *138*, 144–157, DOI 10.1039/c2an36090j, (cit. on p. 22).

[99] J. Filik, M. D. Frogley, J. K. Pijanka, K. Wehbe, G. Cinque, “Electric field standing wave artefacts in FTIR micro-spectroscopy of biological materials”, in *The Analyst* **2012**, *137*, 853, DOI 10.1039/c2an15995c, (cit. on p. 22).

[100] B. M. DeVetter, S. Kenkel, S. Mittal, R. Bhargava, T. P. Wrobel, “Characterization of the structure of low-e substrates and consequences for IR transflection measurements”, in *Vibrational Spectroscopy* **2017**, *91*, 119–127, DOI 10.1016/j.vibspec.2016.09.001, (cit. on pp. 22, 79).

[101] T. P. Wrobel, B. Wajnchold, H. J. Byrne, M. Baranska, “Electric field standing wave effects in FT-IR transflection spectra of biological tissue sections: Simulated models of experimental variability”, in *Vibrational Spectroscopy* **2013**, *69*, 84–92, DOI 10.1016/j.vibspec.2013.09.008, (cit. on p. 22).

[102] J. Lee, “On the non-existence of the so-called electric field standing wave effect in transflection FTIR spectra”, in *Vibrational Spectroscopy* **2017**, *90*, 104–111, DOI 10.1016/j.vibspec.2017.03.007, (cit. on pp. 22, 79).

[103] M. J. Pilling, A. Henderson, P. Gardner, “Quantum Cascade Laser Spectral Histopathology: Breast Cancer Diagnostics Using High Throughput Chemical Imaging”, in *Analytical Chemistry* **07/2017**, *89*, 7348–7355, DOI 10.1021/acs.analchem.7b00426, (cit. on pp. 22, 67).

[104] S. Tiwari, J. Raman, V. Reddy, A. Ghetler, R. P. Tella, Y. Han, C. R. Moon, C. D. Hoke, R. Bhargava, "Towards Translation of Discrete Frequency Infrared Spectroscopic Imaging for Digital Histopathology of Clinical Biopsy Samples", in *Analytical Chemistry* **10/2016**, *88*, 10183–10190, DOI 10.1021/acs.analchem.6b02754, (cit. on pp. 22, 39, 67).

[105] P. R. Griffiths, J. A. De Haseth, *Fourier transform infrared spectrometry*, Wiley-Interscience, **2007**, p. 529 (cit. on p. 23).

[106] H. Grahn, P. Geladi, *Techniques and Applications of Hyperspectral Image Analysis*, John Wiley and Sons, Chichester, **2007**, p. 368 (cit. on pp. 23, 80).

[107] R. Brereton, *Chemometrics for Pattern Recognition (Google eBook)*, John Wiley and Sons, Chichester, **2009**, p. 522 (cit. on pp. 26, 33).

[108] P. Geladi, D. MacDougall, H. Martens, "LINEARIZATION AND SCATTER-CORRECTION FOR NEAR-INFRARED REFLECTANCE SPECTRA OF MEAT.", in *Applied Spectroscopy* **05/1985**, *39*, 491–500, DOI 10.1366/0003702854248656, (cit. on p. 27).

[109] N. K. Afseth, A. Kohler, "Extended multiplicative signal correction in vibrational spectroscopy, a tutorial", in *Chemometrics and Intelligent Laboratory Systems* **08/2012**, *117*, 92–99, DOI 10.1016/j.chemolab.2012.03.004, (cit. on p. 27).

[110] H. Martens, E. Stark, "Extended multiplicative signal correction and spectral interference subtraction: New preprocessing methods for near infrared spectroscopy", in *Journal of Pharmaceutical and Biomedical Analysis* **01/1991**, *9*, 625–635, DOI 10.1016/0731-7085(91)80188-F, (cit. on p. 27).

[111] P. Bassan, A. Kohler, H. Martens, J. Lee, H. J. Byrne, P. Dumas, E. Gazi, M. Brown, N. Clarke, P. Gardner, "Resonant Mie Scattering (RMieS) correction of infrared spectra from highly scattering biological samples", in *The Analyst* **02/2010**, *135*, 268–277, DOI 10.1039/B921056C, (cit. on pp. 27, 29).

[112] E. Ly, O. Piot, R. Wolthuis, A. Durlach, P. Bernard, M. Manfait, "Combination of FTIRspectral imaging and chemometrics for tumour detection from paraffin-embedded biopsies", in *The Analyst* **02/2008**, *133*, 197–205, DOI 10.1039/B715924B, (cit. on pp. 27, 29).

[113] J. Nallala, G. R. Lloyd, N. Stone, "Evaluation of different tissue de-paraffinization procedures for infrared spectral imaging", in *The Analyst* **03/2015**, *140*, 2369–2375, DOI 10.1039/C4AN02122C, (cit. on pp. 27, 30, 68, 71, 74, 78, 79).

[114] R. J. Barnes, M. S. Dhanoa, S. J. Lister, "Standard normal variate transformation and de-trending of near-infrared diffuse reflectance spectra", in *Applied Spectroscopy* **07/1989**, *43*, 772–777, DOI 10.1366/0003702894202201, (cit. on p. 27).

[115] M. S. Dhanoa, S. J. Lister, R. Sanderson, R. J. Barnes, "The link between multiplicative scatter correction (MSC) and standard normal variate (SNV) transformations of NIR spectra", in *Journal of Near Infrared Spectroscopy* **1994**, *2*, 43–47, DOI 10.1255/jnirs.30, (cit. on p. 27).

[116] I. S. Helland, T. Nos, T. Isaksson, "Related versions of the multiplicative scatter correction method for preprocessing spectroscopic data", in *Chemometrics and Intelligent Laboratory Systems* **10/1995**, *29*, 233–241, DOI 10.1016/0169-7439(95)80098-T, (cit. on p. 27).

[117] C. A. Lieber, A. Mahadevan-Jansen, "Automated Method for Subtraction of Fluorescence from Biological Raman Spectra", in *Applied Spectroscopy* **11/2003**, *57*, 1363–1367, DOI 10.1366/000370203322554518, (cit. on p. 27).

[118] M. A. Kneen, H. J. Annegarn, "Algorithm for fitting XRF, SEM and PIXE X-ray spectra backgrounds", in *Nuclear Instruments and Methods in Physics Research Section B: Beam Interactions with Materials and Atoms* **04/1996**, *109-110*, 209–213, DOI 10.1016/0168-583X(95)00908-6, (cit. on p. 27).

[119] P. H. Eilers, A perfect smoother, **2003** (cit. on p. 27).

[120] S. He, W. Zhang, L. Liu, Y. Huang, J. He, W. Xie, P. Wu, C. Du, "Baseline correction for Raman spectra using an improved asymmetric least squares method", in *Anal. Methods* **2014**, *6*, 4402–4407, DOI 10.1039/C4AY00068D, (cit. on p. 27).

[121] J. Peng, S. Peng, A. Jiang, J. Wei, C. Li, J. Tan, "Asymmetric least squares for multiple spectra baseline correction", in *Analytica Chimica Acta* **2010**, *683*, 63–68, DOI 10.1016/j.aca.2010.08.033, (cit. on p. 27).

[122] K. H. Liland, T. Almøy, B. H. Mevik, "Optimal baseline correction for multivariate calibration using open-source software", in *American Laboratory* **09/2011**, *43*, 13–16, DOI 10.1366/000370210792434350, (cit. on p. 27).

[123] M. R. Whitbeck, SECOND DERIVATIVE INFRARED SPECTROSCOPY. **1981** (cit. on p. 28).

[124] A. Savitzky, M. J. Golay, "Smoothing and Differentiation of Data by Simplified Least Squares Procedures", in *Analytical Chemistry* **07/1964**, *36*, 1627–1639, DOI 10.1021/ac60214a047, (cit. on p. 28).

[125] S. W. Bruun, A. Kohler, I. Adt, G. D. Sockalingum, M. Manfait, H. Martens, "Correcting attenuated total reflection-fourier transform infrared spectra for water vapor and carbon dioxide", in *Applied Spectroscopy* **09/2006**, *60*, 1029–1039, DOI 10.1366/000370206778397371, (cit. on p. 28).

[126] G. Erik, R. Jean-Marie, "Subtraction of atmospheric water contribution in Fourier transform infrared spectroscopy of biological membranes and proteins", in *Spectrochimica Acta Part A: Molecular Spectroscopy* **1994**, *50*, 2137–2144, DOI 10.1016/0584-8539(94)00167-7, (cit. on p. 28).

[127] D. Perez-Guaita, J. Kuligowski, G. Quintás, S. Garrigues, M. De La Guardia, "Atmospheric compensation in fourier transform infrared (FT-IR) spectra of clinical samples", in *Applied Spectroscopy* **11/2013**, *67*, 1339–1342, DOI 10.1366/13-07159, (cit. on p. 28).

[128] M. Miljković, B. Bird, K. Lenau, A. I. Mazur, M. Diem, "Spectral cytopathology: new aspects of data collection, manipulation and confounding effects", in *The Analyst* **07/2013**, *138*, 3975, DOI 10.1039/c3an00185g, (cit. on p. 28).

[129] PerkinElmer Inc., "Atmospheric Vapor Compensation on Spectrum Two and Frontier FT-IR Spectrometers", in *Technical Note - PerkinElmer* **2010**, 1–2, (cit. on p. 28).

[130] Robert Alan Hoult, European patent application, **2008** (cit. on p. 28).

[131] A. Köhler, J. Sulé-Suso, G. D. Sockalingum, M. Tobin, F. Bahrami, Y. Yang, J. Pijanka, P. Dumas, M. Cotte, D. G. Van Pittius, G. Parkes, H. Martens, "Estimating and correcting Mie scattering in synchrotron-based microscopic fourier transform infrared spectra by extended multiplicative signal correction", in *Applied Spectroscopy* **03/2008**, *62*, 259–266, DOI 10.1366/000370208783759669, (cit. on p. 29).

[132] M. Romeo, M. Diem in Vibrational Spectroscopy, *Vol. 38*, **07/2005**, pp. 129–132 (cit. on p. 29).

[133] D. C. Fernandez, R. Bhargava, S. M. Hewitt, I. W. Levin, "Infrared spectroscopic imaging for histopathologic recognition", in *Nature Biotechnology* **04/2005**, *23*, 469–474, DOI 10.1038/nbt1080, (cit. on pp. 29, 38, 67, 80).

[134] C. Hughes, L. Gaunt, M. Brown, N. W. Clarke, P. Gardner, "Assessment of paraffin removal from prostate FFPE sections using transmission mode FTIR-FPA imaging", in *Anal. Methods* **2014**, *6*, 1028–1035, DOI 10.1039/C3AY41308J, (cit. on p. 29).

[135] H. Martens, J. P. Nielsen, S. B. Engelsen, "Light Scattering and Light Absorbance Separated by Extended Multiplicative Signal Correction. Application to Near-Infrared Transmission Analysis of Powder Mixtures", in *Anal Chem* **02/2003**, *75*, 394–404, DOI 10.1021/ac020194w, (cit. on p. 30).

[136] S. D. Brown, R. Tauler, B. Walczak, *Comprehensive Chemometrics: Data preprocessing, linear soft-modeling, unsupervised data mining*, *Vol. 2*, Elsevier, **2009** (cit. on p. 30).

[137] L. Ashton, K. A. Hollywood, R. Goodacre, "Making colourful sense of Raman images of single cells", in *The Analyst* **2015**, *140*, 1852–1858, DOI 10.1039/C4AN02298J, (cit. on p. 31).

[138] R. G. Brereton, *Chemometrics: Data Analysis for the Laboratory and Chemical Plant*, *Vol. 8*, John Wiley and Sons, Chichester, **2003**, pp. 1–471 (cit. on p. 31).

[139] S. Wold, "Principal component analysis", in *Chemometrics and Intelligent Laboratory Systems* **07/1987**, *2*, 37–52, (cit. on p. 31).

[140] P. Geladi, H. Isaksson, L. Lindqvist, S. Wold, K. Esbensen, "Principal component analysis of multivariate images", in *Chemometrics and Intelligent Laboratory Systems* **03/1989**, *5*, 209–220, DOI 10.1016/0169-7439(89)80049-8, (cit. on p. 31).

[141] A. A. Green, M. Berman, P. Switzer, M. D. Craig, "A Transformation for Ordering Multispectral Data in Terms of Image Quality with Implications for Noise Removal", in *IEEE Transactions on Geoscience and Remote Sensing* **1988**, *26*, 65–74, DOI 10.1109/36.3001, (cit. on p. 32).

[142] J. B. Lee, A. S. Woodyatt, M. Berman, "Enhancement of High Spectral Resolution Remote-Sensing Data by a Noise-Adjusted Principal Components Transform", in *IEEE Transactions on Geoscience and Remote Sensing* **05/1990**, *28*, 295–304, DOI 10.1109/36.54356, (cit. on p. 32).

[143] R. Larsen in Journal of Chemometrics, *Vol. 16*, **08/2002**, pp. 427–435 (cit. on p. 32).

[144] R. O. Duda, P. E. Hart, D. G. Stork, *Pattern classification*, Wiley-Interscience, **2001**, p. 654 (cit. on p. 32).

[145] C. Cortes, V. Vapnik, *Finding Groups in Data*, (Eds.: L. Kaufman, P. J. Rousseeuw), John Wiley & Sons, Inc., Hoboken, **03/1990**, pp. 273–297 (cit. on pp. 32, 33).

[146] J. C. Bezdek, *Pattern Recognition with Fuzzy Objective Funcion Algorithms*, Springer US, Boston, **1981** (cit. on p. 33).

[147] J. C. Dunn, "A fuzzy relative of the ISODATA process and its use in detecting compact well-separated clusters", in *Journal of Cybernetics* **01/1973**, *3*, 32–57, DOI 10.1080/01969727308546046, (cit. on p. 33).

[148] J. C. Noordam, W. H. a. M. Van den Broek, L. M. C. Buydens, "Unsupervised segmentation of predefined shapes in multivariate images", in *Journal of Chemometrics* **04/2003**, *17*, 216–224, DOI 10.1002/cem.794, (cit. on p. 33).

[149] T. Kohonen, *Self-Organizing Maps*, Springer, **2000** (cit. on p. 33).

[150] G. R. Lloyd, J. Wood, C. Kendall, T. Cook, N. Shepherd, N. Stone, "Histological imaging of a human colon polyp sample using Raman spectroscopy and self organising maps", in *Vibrational Spectroscopy* **03/2012**, *60*, 43–49, DOI 10.1016/j.vibspec.2012.02.015, (cit. on p. 33).

[151] M. Barker, W. Rayens, "Partial least squares for discrimination", in *Journal of Chemometrics* **03/2003**, *17*, 166–173, DOI 10.1002/cem.785, (cit. on p. 33).

[152] R. G. Brereton, G. R. Lloyd, "Partial least squares discriminant analysis: Taking the magic away", in *Journal of Chemometrics* **2014**, *28*, 213–225, DOI 10.1002/cem.2609, (cit. on p. 33).

[153] R. G. Brereton, G. R. Lloyd, "Support Vector Machines for classification and regression", in *The Analyst* **02/2010**, *135*, 230–267, DOI 10.1039/B918972F, (cit. on p. 33).

[154] L. Breiman, "Random Forests", in *Machine Learning* **2001**, *45*, 5–32, DOI 10.1023/A:1010933404324, (cit. on p. 33).

[155] C. M. Bishop, *Neural Networks for Pattern Recognition. Vol. 92*, Oxford University Press, Inc., New York, **1997**, p. 1642 (cit. on p. 33).

[156] J. Shlens, "A Tutorial on Principal Component Analysis", in *CoRR* **2014**, *abs/1404.1100*, (cit. on p. 34).

[157] P. Geladi, K. Esbensen, "Regression on multivariate images: Principal component regression for modeling, prediction and visual diagnostic tools", in *Journal of Chemometrics* **1991**, *5*, 97–111, DOI 10.1002/cem.1180050206, (cit. on p. 35).

[158] I. S. Helland, T. Almøy, "Comparison of prediction methods when only a few components are relevant", in *Journal of the American Statistical Association* **1994**, *89*, 583–591, (cit. on p. 35).

[159] P. Geladi, B. R. Kowalski, "Partial least-squares regression: a tutorial", in *Anal Chim Acta* **1986**, *185*, 1–17, DOI 10.1016/0003-2670(86)80028-9, (cit. on p. 36).

[160] L.-Z. Yi, J. He, Y.-Z. Liang, D.-L. Yuan, F.-T. Chau, "Plasma fatty acid metabolic profiling and biomarkers of type 2 diabetes mellitus based on GC/MS and PLS-LDA", in *FEBS Letters* **2006**, *580*, 6837–6845, DOI 10.1016/j.febslet.2006.11.043, (cit. on p. 36).

[161] H. S. Tapp, M. Defernez, E. K. Kemsley, "FTIR Spectroscopy and Multivariate Analysis Can Distinguish the Geographic Origin of Extra Virgin Olive Oils", in *Journal of Agricultural and Food Chemistry* **2003**, *51*, PMID: 14518931, 6110–6115, DOI 10.1021/jf030232s, (cit. on p. 36).

[162] R. A. FISHER, "THE USE OF MULTIPLE MEASUREMENTS IN TAXONOMIC PROBLEMS", in *Annals of Eugenics*, *7*, 179–188, DOI 10.1111/j.1469-1809.1936.tb02137.x, (cit. on p. 36).

[163] S. J. Raudys, A. K. Jain, "Small sample size effects in statistical pattern recognition: recommendations for practitioners", in *IEEE Transactions on Pattern Analysis and Machine Intelligence* **03/1991**, *13*, 252–264, DOI 10.1109/34.75512, (cit. on p. 36).

[164] R. Huang, Q. Liu, H. Lu, S. Ma, "Solving the small sample size problem of LDA", in **08/2002**, *3*, 29–32 vol.3, DOI 10.1109/ICPR.2002.1047787, (cit. on p. 36).

[165] G. R. Lloyd, N. Stone, "Method for Identification of Spectral Targets in Discrete Frequency Infrared Spectroscopy for Clinical Diagnostics", in *Applied Spectroscopy* **09/2015**, *69*, 1066–1073, DOI 10.1366/14-07677, (cit. on pp. 37, 78).

[166] R. G. Zhbankov, *Infrared Spectra of Cellulose and its Derivatives*, *Vol. 42*, **1995**, pp. 79–88 (cit. on p. 38).

[167] M. Diem, M. Romeo, S. Boydston-White, M. Miljković, C. Matthäus, "A decade of vibrational micro–spectroscopy of human cells and tissue (1994–2004)", in *The Analyst* **2004**, *129*, 880–885, DOI 10.1039/B408952A, (cit. on p. 38).

[168] T. P. Wrobel, M. R. Kole, R. Bhargava, "Emerging trends and opportunities in discrete frequency infrared and Raman spectroscopic imaging", in *Spectroscopy* **2016**, *31*, 1–19, (cit. on p. 38).

[169] L. G. Luna, A. F. I. of Pathology (U.S.), *Manual of Histologic Staining Methods ; of the Armed Forces Institute of Pathology. Edited by Lee G. Luna*, Blakiston Division, McGraw-Hill, **1968** (cit. on p. 38).

[170] R. Bhargava, A. Madabhushi, "Emerging Themes in Image Informatics and Molecular Analysis for Digital Pathology", in *Annual Review of Biomedical Engineering* **07/2016**, *18*, 387–412, DOI 10.1146/annurev-bioeng-112415-114722, (cit. on pp. 38, 39, 52).

[171] O. J. Old, G. R. Lloyd, J. Nallala, M. Isabelle, L. M. Almond, N. A. Shepherd, C. A. Kendall, A. C. Shore, H. Barr, N. Stone, "Rapid infrared mapping for highly accurate automated histology in Barrett's oesophagus", in *The Analyst* **2017**, *142*, 1227–1234, DOI 10.1039/C6AN01871H, (cit. on pp. 39, 51, 67, 70, 71, 76).

[172] A. Akalin, X. Mu, M. A. Kon, A. Ergin, S. H. Remiszewski, C. M. Thompson, D. J. Raz, M. Diem, "Classification of malignant and benign tumors of the lung by infrared spectral histopathology (SHP)", in *Laboratory Investigation* **04/2015**, *95*, 406–421, DOI 10.1038/labinvest.2015.1, (cit. on pp. 39, 67).

[173] A. Banas, K. Banas, A. Furgal-Borzych, W. M. Kwiatek, B. Pawlicki, M. B. H. Breese, "The pituitary gland under infrared light – in search of a representative spectrum for homogeneous regions", in *The Analyst* **2015**, *140*, 2156–2163, DOI 10.1039/C4AN01985G, (cit. on p. 39).

[174] C. Beleites, O. Guntinas-Lichius, G. Ernst, J. Popp, C. Krafft, "FTIR microscopic imaging of carcinoma tissue section with 4× and 15× objectives: Practical considerations", in *Biomedical Spectroscopy and Imaging* **2015**, *4*, 57–66, DOI 10.3233/BSI-140101, (cit. on pp. 39, 67).

[175] B. Bird, J. Rowlette, "High definition infrared chemical imaging of colorectal tissue using a Spero QCL microscope", in *The Analyst* **04/2017**, *142*, 1381–1386, DOI 10.1039/C6AN01916A, (cit. on pp. 39, 67).

[176] B. Bird, M. J. Baker, Quantum Cascade Lasers in Biomedical Infrared Imaging, **10/2015** (cit. on p. 39).

[177] L. Foreman, J. A. Kimber, K. V. Oliver, J. M. Brown, S. M. Janes, T. Fearn, S. G. Kazarian, P. Rich in, *Vol. 9332*, (Ed.: G. L. Coté), **03/2015**, 93320S (cit. on p. 39).

[178] E. Giorgini, S. Sabbatini, C. Conti, C. Rubini, R. Rocchetti, M. Re, L. Vaccari, E. Mitri, V. Librando, "Vibrational mapping of sinonasal lesions by Fourier transform infrared imaging spectroscopy", in *Journal of Biomedical Optics* **12/2015**, *20*, 125003, DOI 10.1117/1.JBO.20.12.125003, (cit. on pp. 39, 67).

[179] F. Großerueschkamp, T. Bracht, H. C. Diehl, C. Kuepper, M. Ahrens, A. Kallenbach-Thieltges, A. Mosig, M. Eisenacher, K. Marcus, T. Behrens, T. Broening, D. Theegarten, B. Sitek, K. Gerwert, "Spatial and molecular resolution of diffuse malignant mesothelioma heterogeneity by integrating label-free FTIR imaging, laser capture microdissection and proteomics", in *Scientific Reports* **03/2017**, *7*, 44829, DOI 10.1038/srep44829, (cit. on pp. 39, 67).

[180] L. S. Leslie, T. P. Wrobel, D. Mayerich, S. Bindra, R. Emmadi, R. Bhargava, "High definition infrared spectroscopic imaging for lymph node histopathology", in *PLoS ONE* **2015**, *10*, e0127238, DOI 10.1371/journal.pone.0127238, (cit. on pp. 39, 67).

[181] S. Mittal, T. P. Wrobel, L. S. Leslie, A. Kadjacsy-Balla, R. Bhargava in SPIE Medical Imaging, *Vol. 9791*, **2016**, p. 979118 (cit. on pp. 39, 67).

[182] R. Bellman, *Dynamic programming*. Princeton University Press, **1972**, p. 342 (cit. on p. 39).

[183] F. N. Pounder et al., "Development of a practical spatial-spectral analysis protocol for breast histopathology using Fourier transform infrared spectroscopic imaging", in *Faraday Discuss.* **2016**, *187*, 43–68, DOI 10.1039/C5FD00199D, (cit. on p. 40).

[184] E. Goormaghtigh, "Infrared imaging in histopathology: Is a unified approach possible?", in *Biomedical Spectroscopy and Imaging* **01/2017**, *5*, 325–346, DOI 10.3233/BSI-160151, (cit. on pp. 40, 67).

[185] O. Remesz, Derived from: Tractus intestinalis esophagus.svg - Wikimedia Commons, licensed under CC BY 2.0 (cit. on p. 41).

[186] N. A. Shepherd in *Morson and Dawson's Gastrointestinal Pathology*, Wiley-Blackwell, Oxford, UK, **12/2012**, pp. 39–51 (cit. on pp. 42, 43).

[187] C. C. Abnet, M. Arnold, W. Q. Wei, "Epidemiology of Esophageal Squamous Cell Carcinoma", in *Gastroenterology* **2018**, *154*, 360–373, DOI 10.1053/j.gastro.2017.08.023, (cit. on p. 44).

[188] J. Dent, H. B. El-Serag, M. A. Wallander, S. Johansson, "Epidemiology of gastro-oesophageal reflux disease: A systematic review", in *Gut* **2005**, *54*, 710–717, DOI 10.1136/gut.2004.051821, (cit. on pp. 44, 48).

[189] G. Locke, N. Talley, S. Fett, A. Zinsmeister, L. Melton, "Prevalence and clinical spectrum of gastroesophageal reflux: A population-based study in Olmsted County, Minnesota", in *Gastroenterology* **05/1997**, *112*, 1448–1456, DOI 10.1016/S0016-5085(97)70025-8, (cit. on pp. 44, 48).

[190] Z. R. Edelstein, D. C. Farrow, M. P. Bronner, S. N. Rosen, T. L. Vaughan, "Central Adiposity and Risk of Barrett's Esophagus", in *Gastroenterology* **08/2007**, *133*, 403–411, DOI 10.1053/J.GASTRO.2007.05.026, (cit. on p. 44).

[191] H. B. El-Serag, N. J. Petersen, J. Carter, D. Y. Graham, P. Richardson, R. M. Genta, L. Rabeneck, "Gastroesophageal reflux among different racial groups in the United States", in *Gastroenterology* **06/2004**, *126*, 1692–1699, DOI 10.1053/J.GASTRO.2004.03.077, (cit. on p. 44).

[192] N. R. Barrett, "Chronic peptic ulcerz of the oeophagus and oesophagitis'", in *British Journal of Surgery* **10/1950**, *38*, 175–182, DOI 10.1002/bjs.18003815005, (cit. on p. 44).

[193] F. Hvid-Jensen, L. Pedersen, A. M. Drewes, H. T. Sørensen, P. Funch-Jensen, "Incidence of Adenocarcinoma among Patients with Barrett's Esophagus", in *New England Journal of Medicine* **10/2011**, *365*, 1375–1383, DOI 10.1056/NEJMoa1103042, (cit. on p. 44).

[194] S. J. Spechler, "Barrett Esophagus and Risk of Esophageal Cancer", in *Jama* **2013**, *310*, 627, DOI 10.1001/jama.2013.226450, (cit. on p. 44).

[195] J. F. Fléjou, "Barrett's oesophagus: From metaplasia to dysplasia and cancer", in *Gut* **03/2005**, *54*, i6–12, DOI 10.1136/gut.2004.041525, (cit. on p. 44).

[196] R. J. Schlemper et al., "The vienna classification of gastrointestinal epithelial neoplasia", in *Gut* **08/2000**, *47*, 251–255, DOI 10.1136/gut.47.2.251, (cit. on pp. 45–47, 98).

[197] N. J. Shaheen, J. E. Richter, "Barrett's oesophagus", in *The Lancet* **03/2009**, *373*, 850–861, DOI 10.1016/S0140-6736(09)60487-6, (cit. on p. 45).

[198] N. J. Shaheen, G. W. Falk, P. G. Iyer, L. B. Gerson, "ACG Clinical Guideline: Diagnosis and Management of Barrett's Esophagus", in *The American Journal Of Gastroenterology* **11/2016**, *111*, 30–50, (cit. on pp. 46, 48).

[199] A. L. Mescher, *Junqueira ' s Basic Histology Text & Atlas (14th ed .)* 12th ed., McGraw Hill Professional, **2009**, pp. 1–4 (cit. on p. 46).

[200] F. Chedgy, C. Fogg, K. Kandiah, H. Barr, B. Higgins, M. McCord, A. Dewey, J. De Caestecker, L. Gadeke, C. Stokes, D. Poller, G. Longcroft-Wheaton, P. Bhandari, "Acetic acid-guided biopsies in Barrett's surveillance for neoplasia detection versus non-targeted biopsies (Seattle protocol): A feasibility study for a randomized tandem endoscopy trial. The ABBA study", in *Endoscopy International Open* **2018**, *06*, E43–E50, DOI 10.1055/s-0043-120829, (cit. on p. 47).

[201] K. B. Dunbar, R. F. Souza, S. J. Spechler, "The Effect of Proton Pump Inhibitors on Barrett's Esophagus", in *Gastroenterology Clinics of North America* **2015**, *44*, 415–424, DOI 10.1016/j.gtc.2015.02.010, (cit. on p. 48).

[202] M. Farhad, P. Bhandari, K. Ragunath, H. Barr, R. Haidry, L. Lovat, H. Smart, R. Harrison, C. Stokes, K. Smith, T. Morris, J. S. De Caestecker, "Radiofrequency ablation compared with argon plasma coagulation after endoscopic resection of high-grade dysplasia or T1 adenocarcinoma in Barrett's esophagus: a randomized pilot study (BRIDE)", in *Gastrointestinal Endoscopy* **2018**, DOI 10.1016/j.gie.2018.07.031, (cit. on p. 48).

[203] K. N. Phoa et al., "Radiofrequency Ablation vs Endoscopic Surveillance for Patients With Barrett Esophagus and Low-Grade Dysplasia", in *Jama* **2014**, *311*, 1209, DOI 10.1001/jama.2014.2511, (cit. on p. 48).

[204] J. Lagergren, E. Smyth, D. Cunningham, P. Lagergren, "Oesophageal cancer", in *The Lancet* **2017**, *390*, 2383–2396, DOI 10.1016/S0140-6736(17)31462-9, (cit. on p. 48).

[205] R. C. Fitzgerald, M. F. Vaezi, "Esophageal Diseases", in *Gastroenterology* **2017**, 1–4, DOI 10.1053/j.gastro.2017.12.017, (cit. on p. 48).

[206] J. E. Richter, J. H. Rubenstein, "Presentation and Epidemiology of Gastroesophageal Reflux Disease", in *Gastroenterology* **2017**, 1–10, DOI 10.1053/j.gastro.2017.07.045, (cit. on p. 48).

[207] H. G. Coleman, S.-H. Xie, J. Lagergren, "The Epidemiology of Esophageal Adenocarcinoma", in *Gastroenterology* **2017**, 1–16, DOI 10.1053/j.gastro.2017.07.046, (cit. on p. 48).

[208] G. Edgren, H. O. Adami, E. W. Vainio, O. Nyrén, "A global assessment of the oesophageal adenocarcinoma epidemic", in *Gut* **2013**, *62*, 1406–1414, DOI 10.1136/gutjnl-2012-302412, (cit. on p. 48).

[209] R. L. Siegel, K. D. Miller, A. Jemal, "Cancer statistics, 2017", in *CA: A Cancer Journal for Clinicians* **01/2017**, *67*, 7–30, DOI 10.3322/caac.21387, (cit. on p. 48).

[210] T. L. Vaughan, R. C. Fitzgerald, "Precision prevention of oesophageal adenocarcinoma", in *Nature Reviews Gastroenterology and Hepatology* **2015**, *12*, 243–248, DOI 10.1038/nrgastro.2015.24, (cit. on p. 48).

[211] R. Singh, K. Ragunath, J. Jankowski, "Barrett's Esophagus: Diagnosis, Screening, Surveillance, and Controversies.", in *Gut and liver* **2007**, *1*, 93–100, DOI 10.5009/gnl.2007.1.2.93, (cit. on p. 49).

[212] M. Vieth, C. Ell, L. Gossner, A. May, M. Stolte, "Histological analysis of endoscopic resection specimens from 326 patients with Barrett's esophagus and early neoplasia", in *Endoscopy* **2004**, *36*, 776–781, DOI 10.1055/s-2004-825802, (cit. on p. 49).

[213] P. Sharma, A. R. Meining, E. Coron, C. J. Lightdale, H. C. Wolfsen, A. Bansal, M. Bajbouj, J. P. Galmiche, J. A. Abrams, A. Rastogi, N. Gupta, J. E. Michalek, G. Y. Lauwers, M. B. Wallace, "Real-time increased detection of neoplastic tissue in Barrett's esophagus with probe-based confocal laser endomicroscopy: Final results of an international multicenter, prospective, randomized, controlled trial", in *Gastrointestinal Endoscopy* **2011**, *74*, 465–472, DOI 10.1016/j.gie.2011.04.004, (cit. on p. 49).

[214] G. W. Falk, "Probe-based confocal endomicroscopy in Barrett's esophagus: The real deal or another tease?", in *Gastrointestinal Endoscopy* **2011**, *74*, 473–476, DOI 10.1016/j.gie.2011.05.046, (cit. on p. 49).

[215] P. Lao-Sirieix, A. Boussioutas, S. R. Kadri, M. O'Donovan, I. Debiram, M. Das, L. Harihar, R. C. Fitzgerald, "Non-endoscopic screening biomarkers for Barrett's oesophagus: From microarray analysis to the clinic", in *Gut* **2009**, *58*, 1451–1459, DOI 10.1136/gut.2009.180281, (cit. on p. 49).

[216] C. S. Ross-Innes et al., "Evaluation of a Minimally Invasive Cell Sampling Device Coupled with Assessment of Trefoil Factor 3 Expression for Diagnosing Barrett's Esophagus: A Multi-Center Case-Control Study", in *PLoS Medicine* **2015**, *12*, 1–19, DOI 10.1371/journal.pmed.1001780, (cit. on p. 49).

[217] J. Offman et al., "Barrett's oESophagus trial 3 (BEST3): Study protocol for a randomised controlled trial comparing the Cytosponge-TFF3 test with usual care to facilitate the diagnosis of oesophageal pre-cancer in primary care patients with chronic acid reflux", in *BMC Cancer* **2018**, *18*, DOI 10.1186/s12885-018-4664-3, (cit. on p. 50).

[218] K. Papamarkakis, B. Bird, J. M. Schubert, M. Miljković, R. Wein, K. Bedrossian, N. Laver, M. Diem, "Cytopathology by optical methods: Spectral cytopathology of the oral mucosa", in *Laboratory Investigation* **2010**, *90*, 589–598, DOI 10.1038/labinvest.2010.1, (cit. on p. 50).

[219] D. Townsend, M. Miljković, B. Bird, K. Lenau, O. Old, M. Almond, C. Kendall, G. Lloyd, N. Shepherd, H. Barr, N. Stone, M. Diem, "Infrared micro-spectroscopy for cyto-pathological classification of esophageal cells", in *Analyst* **2015**, *140*, 2215–2223, DOI 10.1039/c4an01884b, (cit. on p. 50).

[220] O. Old, G. Lloyd, M. Isabelle, L. M. Almond, C. Kendall, K. Baxter, N. Shepherd, A. Shore, N. Stone, H. Barr, "Automated cytological detection of Barrett's neoplasia with infrared spectroscopy", in *Journal of Gastroenterology* **2018**, *53*, 227–235, DOI 10.1007/s00535-017-1344-z, (cit. on p. 50).

[221] T. D. Wang, G. Triadafilopoulos, J. M. Crawford, L. R. Dixon, T. Bhandari, P. Sahbaie, S. Friedland, R. Soetikno, C. H. Contag, "Detection of endogenous biomolecules in Barrett's esophagus by Fourier transform infrared spectroscopy.", in *Proceedings of the National Academy of Sciences of the United States of America* **2007**, *104*, 15864–15869, DOI 10.1073/pnas.0707567104, (cit. on p. 50).

[222] L. Quaroni, A. G. Casson, "Characterization of Barrett esophagus and esophageal adenocarcinoma by Fourier-transform infrared microscopy", in *Analyst* **2009**, *134*, 1240–1246, DOI 10.1039/b823071d, (cit. on pp. 51, 67).

[223] H. Amrania, G. Antonacci, C.-H. Chan, L. Drummond, W. R. Otto, N. a. Wright, C. Phillips, "Digistain: a digital staining instrument for histopathology.", in *Optics express* **2012**, *20*, 7290–9, DOI 10.1364/OE.20.007290, (cit. on pp. 51, 80).

[224] M. J. Baker, H. J. Byrne, J. Chalmers, P. Gardner, R. Goodacre, A. Henderson, S. G. Kazarian, F. L. Martin, J. Moger, N. Stone, J. Sulé-Suso, "Clinical applications of infrared and Raman spectroscopy: State of play and future challenges", in *Analyst* **2018**, *143*, 1735–1757, DOI 10.1039/c7an01871a, (cit. on p. 51).

[225] M. Ishigaki, Y. Maeda, A. Taketani, B. B. Andriana, R. Ishihara, K. Wongravee, Y. Ozaki, H. Sato, "Diagnosis of early-stage esophageal cancer by Raman spectroscopy and chemometric techniques", in *Analyst* **2016**, *141*, 1027–1033, DOI 10.1039/c5an01323b, (cit. on p. 52).

[226] M. S. Bergholt, W. Zheng, K. Lin, K. Y. Ho, M. Teh, K. G. Yeoh, J. B. Y. So, Z. Huang, "¡i¿In Vivo¡/i¿ Diagnosis of Esophageal Cancer Using Image-Guided Raman Endoscopy and Biomolecular Modeling", in *Technology in Cancer Research & Treatment* **2011**, *10*, 103–112, DOI 10.7785/tcrt.2012.500185, (cit. on p. 52).

[227] S. Feng, J. Lin, Z. Huang, G. Chen, W. Chen, Y. Wang, R. Chen, H. Zeng, "Esophageal cancer detection based on tissue surface-enhanced Raman spectroscopy and multivariate analysis", in *Applied Physics Letters* **2013**, *102*, DOI 10.1063/1.4789996, (cit. on p. 52).

[228] I. W. Schie, C. Krafft, J. Popp, "Applications of coherent Raman scattering microscopies to clinical and biological studies", in *Analyst* **2015**, *140*, 3897–3909, DOI 10.1039/c5an00178a, (cit. on p. 52).

[229] M. Ji et al., "Rapid, Label-Free Detection of Brain Tumors with Stimulated Raman Scattering Microscopy", in *Science Translational Medicine* **2013**, *5*, 201ra119–201ra119, DOI 10.1126/scitranslmed.3005954, (cit. on p. 52).

[230] R. Critchley-Thorne, J. Prichard, J. Davison, B. Campbell, K. Repa, L. Reese, X. Nguyen, J. Li, T. Foxwell, L. Taylor, "TissueCypher: A systems biology approach to anatomic pathology", in *Journal of Pathology Informatics* **2015**, *6*, 48, DOI 10.4103/2153-3539.163987, (cit. on p. 53).

[231] International Organisation for Standardization, "Photography - Electronic still picture imaging – resolution and spatial frequency responses", in *ISO 12233:2017* **2017**, 1–50, (cit. on p. 54).

[232] Setreset, Reproduced from: USAF-1951 map, calibrated - Wikimedia Commons, licensed under CC BY-SA 3.0 (cit. on p. 54).

[233] Rayleigh, "XXXI. Investigations in optics, with special reference to the spectroscope", in *Philosophical Magazine Series 5* **10/1879**, *8*, 261–274, DOI 10.1080/14786447908639684, (cit. on p. 55).

[234] J. Nallala, G. R. Lloyd, M. Hermes, N. Shepherd, N. Stone, "Enhanced spectral histology in the colon using high-magnification benchtop FTIR imaging", in *Vibrational Spectroscopy* **07/2017**, *91*, 83–91, DOI 10.1016/J.VIBSPEC.2016.08.013, (cit. on pp. 55, 57, 67, 80).

[235] E. F. Glynn, USAF 1951 3-Bar Resolving Power Test Chart, **11/2002**, http://www.efg2.com/Lab/ImageProcessing/TestTargets/index.html (visited on 11/02/2018) (cit. on p. 58).

[236] C. Kuepper, A. Kallenb, H. Juette, A. Tannapfel, F. Großerueschkamp, K. Gerwert, "Quantum Cascade Laser-Based Infrared Microscopy for Label- Free and Automated Cancer Classification in Tissue Sections", in **2018**, 1–10, DOI 10.1038/s41598-018-26098-w, (cit. on pp. 67, 79, 80).

[237] T. Wrobel, R. Bhargava, "Infrared spectroscopic imaging advances as an analytical technology for biomedical sciences", in *Analytical Chemistry* **12/2017**, acs.analchem.7b05330, DOI 10.1021/acs.analchem.7b05330, (cit. on p. 67).

[238] S. Mittal, K. L. Yeh, L. S., S. Kenkel, A. Kajdacsy-Balla, R. Bhargava, "Simultaneous cancer and tumor microenvironment", in *subtyping using confocal infrared microscopy for all-digital molecular histopathology. {Proc}. {Natl}. {Acad}. {Sci}. {U}. {S}. {A}* **2018**, *115*, (cit. on pp. 70, 80).

[239] A. Kohler, C. Kirschner, A. Oust, H. Martens, "Extended Multiplicative Signal Correction as a Tool for Separation and Characterization of Physical and Chemical Information in Fourier Transform Infrared Microscopy Images of Cryo-Sections of Beef Loin", in *Applied Spectroscopy* **06/2005**, *59*, 707–716, DOI 10.1366/0003702054280649, (cit. on p. 74).

[240] A. de Juan, R. Tauler, "Chemometrics applied to unravel multicomponent processes and mixtures: Revisiting latest trends in multivariate resolution", in *Analytica Chimica Acta* **2003**, *500*, 195–210, DOI 10.1016/S0003-2670(03)00724-4, (cit. on p. 74).

[241] M. H. Van Benthem, M. R. Keenan, "Fast algorithm for the solution of large-scale non-negativity-constrained least squares problems", in *Journal of Chemometrics* **03/2005**, *18*, 441–450, DOI 10.1002/cem.889, (cit. on p. 74).

[242] X. Li et al., "Organoid cultures recapitulate esophageal adenocarcinoma heterogeneity providing a model for clonality studies and precision therapeutics", in *Nature Communications* **2018**, *9*, 1–13, DOI 10.1038/s41467-018-05190-9, (cit. on p. 75).

[243] A. M. Van Nistelrooij, R. Van Marion, L. B. Koppert, K. Biermann, M. C. Spaander, H. W. Tilanus, J. J. B. Van Lanschot, B. P. Wijnhoven, W. N. Dinjens, "Molecular clonality analysis of esophageal adenocarcinoma by multiregion sequencing of tumor samples", in *BMC Research Notes* **2017**, *10*, 1–7, DOI 10.1186/s13104-017-2456-5, (cit. on p. 75).

[244] P. Koziol, M. Juszczyk, J. Skibinska, S. Urbaniak, C. Paluszkiewicz, W. M. Kwiatek, T. P. Wróbel, "Comparison of spectral and spatial denoising techniques in the context of hyperspectral data: High Definition FT-IR imaging", in *Scientific Reports* **2018**, *in review*, 1–11, DOI 10.1038/s41598-018-32713-7, (cit. on p. 78).

[245] M. J. Pilling, P. Bassan, P. Gardner, "Comparison of transmission and transflectance mode FTIR imaging of biological tissue", in *The Analyst* **2015**, *140*, 2383–2392, DOI 10.1039/C4AN01975J, (cit. on p. 79).

[246] F. Großerueschkamp, A. Kallenbach-Thieltges, T. Behrens, T. Brüning, M. Altmayer, G. Stamatis, D. Theegarten, K. Gerwert, "Marker-free automated histopathological annotation of lung tumour subtypes by FTIR imaging", in *The Analyst* **2015**, *140*, 2114–2120, DOI 10.1039/C4AN01978D, (cit. on p. 79).

[247] L. M. Fullwood, D. Griffiths, K. Ashton, T. Dawson, R. W. Lea, C. Davis, F. Bonnier, H. J. Byrne, M. J. Baker, "Effect of substrate choice and tissue type on tissue preparation for spectral histopathology by Raman microspectroscopy", in *Analyst* **2014**, *139*, 446–454, DOI 10.1039/C3AN01832F, (cit. on p. 79).

[248] C. Beleites, U. Neugebauer, T. Bocklitz, C. Krafft, J. Popp, "Sample size planning for classification models", in *Analytica Chimica Acta* **2013**, *760*, 25–33, DOI 10.1016/j.aca.2012.11.007, (cit. on pp. 79, 98).

[249] S. Junaid, S. C. Kumar, M. Mathez, M. Hermes, N. Stone, M. E.-Z. N. Shepherd, P. Tidemand-Lichtenberg, C. Pedersen, "Video-rate, mid-IR hyperspectral upconversion imaging", in *In prep.* **10/2018**, -, 1–20, DOI -, (cit. on pp. 80, 84, 86–88, 91, 92).

[250] A. Travo, O. Piot, R. Wolthuis, C. Gobinet, M. Manfait, J. Bara, M.-E. Forgue-Lafitte, P. Jeannesson, "IR spectral imaging of secreted mucus: a promising new tool for the histopathological recognition of human colonic adenocarcinomas", in *Histopathology* **2010**, *56*, 921–931, DOI 10.1111/j.1365-2559.2010.03563.x, (cit. on p. 80).

[251] D. Wang, S. Liang, T. He, Q. Shi, "Estimating clear-sky all-wave net radiation from combined visible and shortwave infrared (VSWIR) and thermal infrared (TIR) remote sensing data", in *Remote Sensing of Environment* **2015**, *167*, 31–39, DOI 10.1016/j.rse.2015.03.022, (cit. on p. 80).

[252] J. Li, U. Parchatka, R. Königstedt, H. Fischer, "Real-time measurements of atmospheric CO using a continuous-wave room temperature quantum cascade laser spectrometer", in *2012 Symposium on Photonics and Optoelectronics SOPO 2012* **2012**, *20*, DOI 10.1109/SOPO.2012.6271103, (cit. on p. 80).

[253] J. Patz, "Global warming.", in *BMJ (Clinical research ed.)* **2004**, *328*, 1269–1270, DOI 10.1136/bmj.328.7451.1269, (cit. on p. 80).

[254] D. F. Meer, H. M. A. Werff, F. J. A. Ruitenbeek, C. A. Hecker, W. H. Bakker, M. F. Noomen, M. Meijde, E. J. M. Carranza, J. B. Smeth, T. Woldai, "Multi-and hyperspectral geologic remote sensing: A review", in *Elsevier* **2012**, *14*, 112–128, (cit. on p. 80).

[255] D. Sun, *Hyperspectral imaging for food quality analysis and control*, Academic press in an imprint of {Elsevier}, **2010** (cit. on p. 80).

[256] F. Peñaranda, V. Naranjo, L. Kastl, B. Kemper, G. R. Lloyd, J. Nallala, N. Stone, J. Schnekenburger, *Multivariate classification of Fourier transform infrared hyperspectral images of skin cancer cells*, *Vol. 2016-November*, Proceedings of {IEEE} European Signal Processing Conference, **2016**, pp. 1328–1332 (cit. on p. 80).

[257] L. M. Kehlet, P. Tidemand-Lichtenberg, J. S. Dam, C. Pedersen, "Infrared upconversion hyperspectral imaging", in *Optics Letters* **03/2015**, *40*, 938–941, DOI 10.1364/OL.40.000938, (cit. on p. 81).

[258] L. M. Kehlet, N. Sanders, P. Tidemand-Lichtenberg, J. S. Dam, C. Pedersen, "Infrared hyperspectral upconversion imaging using spatial object translation", in *Optics Express* **12/2015**, *23*, 34023–34028, DOI 10.1364/OE.23.034023, (cit. on pp. 81, 83).

[259] L. Huot, P. M. Moselund, P. Tidemand-Lichtenberg, L. Leick, C. Pedersen, "Upconversion imaging using an all-fiber supercontinuum source", in *Opt. Lett.* **06/2016**, *41*, 2466–2469, DOI 10.1364/OL.41.002466, (cit. on pp. 83, 84).

[260] M. Mathez, P. J. Rodrigo, P. Tidemand-Lichtenberg, C. Pedersen, "Upconversion imaging using short-wave infrared picosecond pulses", in *Opt. Lett.* **02/2017**, *42*, 579–582, DOI 10.1364/OL.42.000579, (cit. on p. 85).

[261] M. Ebrahim-Zadeh, S. Chaitanya Kumar, "Yb-fiber-laser-pumped ultrafast frequency conversion sources from the mid-infrared to the ultraviolet", in *IEEE Journal on Selected Topics in Quantum Electronics* **2014**, *20*, 7600519, DOI 10.1109/JSTQE.2014.2319590, (cit. on p. 85).

[262] R. A. Andrews, *Wide Angular Aperture Image Up-Conversion*, *Vol. QE-5*, IEEE J. Quantum Electron, **1969**, pp. 548–550 (cit. on p. 87).

[263] C. Beleites, C. Krafft, J. Popp, V. Sergo, *hyperSpec : working with spectroscopic data*, *Vol. 2*, The {R} {User} {Conference}, user! 2011, {Aug} 16, **2011** (cit. on p. 89).

[264] Y.-P. Tseng, P. Bouzy, C. Pedersen, N. Stone, P. Tidemand-Lichtenberg, "Upconversion raster scanning microscope for long-wavelength infrared imaging of breast cancer microcalcifications", in *Biomed. Opt. Express* **10/2018**, *9*, 4979–4987, DOI 10.1364/BOE.9.004979, (cit. on p. 97).

[265] G. V. Trunk, "A Problem of Dimensionality: A Simple Example", in *IEEE Transactions on Pattern Analysis and Machine Intelligence* **07/1979**, *PAMI-1*, 306–307, DOI 10.1109/TPAMI.1979.4766926, (cit. on p. 98).

[266] S. Theodoridis, K. Koutroumbas, *Pattern Recognition 4th Edition*, 4th ed., Elsevier, **2008**, pp. 1–984 (cit. on p. 98).

[267] N. S. G. R. Lloyd, J. Nallala, "Investigating the effect of pixel size of high spatial resolution FTIR imaging for detection of colorectal cancer", in *Proc.SPIE* **2016**, *9703*, 9703–9706, DOI 10.1117/12.2210844, (cit. on p. 99).

[268] M. Isabelle, J. Dorney, A. Lewis, G. R. Lloyd, O. Old, N. Shepherd, M. Rodriguez-Justo, H. Barr, K. Lau, I. Bell, S. Ohrel, G. Thomas, N. Stone, C. Kendall, "Multi-centre Raman spectral mapping of oesophageal cancer tissues: a study to assess system transferability", in *Faraday Discuss.* **2016**, *187*, 87–103, DOI 10.1039/C5FD00183H, (cit. on p. 99).

[269] C. Li, D. Zhang, M. N. Slipchenko, J.-X. Cheng, "Mid-Infrared Photothermal Imaging of Active Pharmaceutical Ingredients at Submicrometer Spatial Resolution", in *Analytical Chemistry* **2017**, *89*, PMID: 28398722, 4863–4867, DOI 10.1021/acs.analchem.6b04638, (cit. on p. 102).

[270] Y. Bai, D. Zhang, L. Lan, Y. Huang, K. Maize, A. Shakouri, J.-X. Cheng, "Ultrafast Chemical Imaging by Widefield Photothermal Sensing of Infrared Absorption", in **11/2018**, (cit. on p. 102).

Acknowledgements

Funding within the scope of Horizon 2020 by the European Union[1] is highly appreciated. This work was conducted as part of the Mid-TECH Marie Curie innovative training network [H2020-MSCA-ITN-2014-642661].

There are numerous people whom I would like to thank for directly and indirectly supporting me in writing this thesis.

First, I would like to express my deepest gratitude towards my supervisor Nick Stone, who has been an absolute rock! Thank you Nick, for giving me the supervision and freedom to carry out this project and learn so many new things. Your positive attitude in even the most stressful situations has been a constant anchor for me and very inspirational for my personal development.

Furthermore, I would like to thank Francesca Palombo, my second supervisor, as well. Francesca, you were an incredible source of motivation, always seeing the good in people.

Jayarupakar Nalalla, thank you very much for welcoming me in Exeter and giving me an incredible start. Hannah Sheridan, thank you for supporting me measuring the TMA in your summer project. I am convinced you will make a great scientist and I wish you the best of luck for your PhD. Thanks also to Mark Heath for training me in the cleanroom.

Thank you very much to the partners at DTU Fotonik and ICFO for the great collaborations.

Another group of people without whom this work would not have been possible are our medical collaborators Neil Shepherd, Hugh Barr and Gavin Lloyd at Gloucester. Thank you for everything you taught me and helped me with!

I would like to thank Rohit Bhargava and his group for hosting me for a stay at the Beckman Institute in Urbana Champaign. The few weeks I stayed there were incredible.

[1] Fuck Brexit!

Thank you to the biophysics group for making lunch a proper break and all the various social events from going to the pub to hiking through the mud of Dartmoor. Thanks to Dave, Tobi, Fay, Beth, Skye, Lou, Rikke, Ryan, Ben, Michelle, Richard, Siva, Bob, Leanne, Sarah, Claudio and Alex[2].

Wolfram Möbius, thank you, not only for the access to your equipment but much more for being a very good friend and climbing partner, making time to head down to the climbing wall even between all the travelling across the world for conferences and research visits.

Thank you to Natalie and Richard who from time to time got me out of the university into the outdoors for sailing, climbing and hiking! You made my time here in Devon unforgettable.

I would not have had the opportunity to work with all of these people if it was not for my family and friends in Germany who always supported me in my decision to take on this adventure:

Danke Tina und Markus für das Korrekturlesen und die gelegentlichen Runden HOTS nach einem langen Tag. Danke auch an Chris dafür.

Danke und “For Pony” an Neli.

Danke an meine Eltern dafür, dass ihr immer da wart, wenn es Rückschläge gab und mich motviert habt, weiter zu machen: “Jetzt geh und hole Bauholz auch wenn du leise fluchst.” Wer hätte jeh gedacht, dass der 8-Jährige, der seiner Lehrerin wütend das Diktatheft vor die Füße schmeißt 20 Jahre später eine Doktorarbeit einreichen würde?

Die letzten Worte dieser Arbeit gebühren meiner Verlobten Ulrike. Ohne dich hätte ich niemals den Mut gehabt, dieses Abenteuer zu wagen und durchzustehen. Ich hoffe wir können noch Viele mehr gemeinsam erleben!